DISSERTATION

COMPUTATIONAL FLUID DYNAMICS MODELING OF A LARGE BORE TWO-STROKE NATURAL GAS ENGINE

Submitted by

Gi-Heon Kim

Department of Mechanical Engineering

In partial fulfillment of the requirements

For the Degree of Doctor of Philosophy

Colorado State University

Fort Collins, Colorado

Fall 2004

COLORADO STATE UNIVERSITY

Nov 3, 2004

WE HEREBY RECOMMEND THAT THE DISSERTATION PREPARED UNDER OUR SUPERVISION BY GI-HEON KIM, ENTITLED "COMPUTATIONAL FLUID DYNAMICS MODELING OF A LARGE BORE TWO-STROKE NATURAL GAS ENGINE" BE ACCEPTED AS FULFILLING IN PART REQUIREMENTS FOR THE DEGREE OF DOCTOR OF PHILOSOPHY.

Committee on Graduate Work

Advisor

Co-Advisor

Department Head

ABSTRACT OF DISSERTATION

COMPUTATIONAL FLUID DYNAMICS MODELING OF A LARGE BORE TWO-STROKE NATURAL GAS ENGINE

Natural gas fueled engines have been used for many years in stationary applications such as gas compression and electric power generation. In the United States alone, there are over 8,000 large bore (bore >30 cm) slow speed (speed < 500 rpm) natural gas engines in use. The most common configuration is a two-stroke cycle with direct injection of natural gas into the cylinder. The specific engine modeled in this study, the GMV Cooper Bessemer engine, is widely used in the gas compression industry, primarily in 10 cylinder versions. As air emission regulations have been enacted, reducing exhaust emission levels from pipeline engines has become increasingly important. Insufficient in-cylinder mixing due to ineffective fuel delivery is believed to be problematic in these natural gas engines. Cyclic combustion instability is a key-contributor to NO_x and CO. Therefore, enhancement of fuel-air mixing using high pressure pipeline gas for fuel injection and use of alternative ignition systems such as pre-combustion chamber ignition and laser ignition are being considered as engine retrofit technologies.

The characteristics of natural gas fuel jets emanating from a low pressure conventional poppet valve and from a retrofitted high pressure valve are investigated and compared. The fuel-air mixing in the engine is characterized and quantified by defining the parameters such as flammable volume fractions. At low injection pressures the gas flow around a typical poppet valve collapses to axis of symmetry of

the valve downstream of the poppet. At high pressure, the gas flow from this simple poppet valve does not collapse, but rather expands outward and eventually flows along the cylinder wall, producing poor mixing in the cylinder.

A Poppet valve is not an efficient valve in delivering momentum to the cylinder. Stagnation pressure losses occurring while the fluid passes through the valve are quantified and classified. Pressure base valve injection efficiency was defined and used to show the valve injection performance. Comparison of the results indicates that it is possible to make remarkable improvements of injection performance in momentum delivery by substituting well designed valves for the conventional poppet valves.

The development of a compatible virtual valve which reproduces downstream jet characteristics of the jet issuing from actual valves is described. Instead of including the complex detail of a real valve, a simple converging-diverging type virtual valve is suggested for three dimensional engine simulation with high pressure injection. The results indicated that the suggested converging-diverging nozzle type virtual valve produces practically identical down stream fuel jet with the real valve injection jets.

The simulation results for three dimensional overall engine simulations for a two-stroke natural gas engine are presented and discussed. The interaction between the scavenging flow and the injected fuel jet causes the jet to deflect enough to impact the piston top off center, producing non-symmetric mixing in the combustion chamber. As a result, the combustion mixture is not fully mixed at the time of ignition. There is a lean region in the core, and richer regions around the edge of the

cylinder, with the richest region in the crevice around the edge of the cylinder. The flame propagation during combustion is non-uniform, with a greater flame speed in regions with a near stoichiometric equivalence ratio and of the engine flow fields favoring the direction of flame propagation.

Retrofitted operation of the engine with high pressure fuel injection, pre-combustion chamber ignition and laser spark ignition are all investigated computationally. The simulation results indicate that high pressure fuel injection enhances the cylinder mixing. The alternative ignition methods examined change the flame propagation pattern so that the duration of heat release is shortened.

Gi-Heon Kim

Department of Mechanical Engineering

Colorado State University

Fort Collins, CO 80523

Fall 2004

CONTENTS

LIST OF FIGURES

LIST OF TABLES

NOMENCLATURE

A^*	area of nozzle throat
A_e	area of nozzle exit
e_p	pressure base valve injection efficiency
M_e	Mach number at nozzle exit
R	gas constant
T_0	stagnation temperature of injection gas
f_f	flammable fuel fraction
f_m	flammable mixture fraction
k	turbulent kinetic energy
m_f	mass of fuel
$\dot{m}_f$	mass flow rate of fuel
p_i	injection pressure
$\dot{p}_x$	axial momentum flow rate
p_0	stagnation pressure of injection gas
p_e	static pressure at nozzle exit
r^*	radius of nozzle throat
r_e	radius of nozzle exit
SOI	start of injection
$\bar{v}$	fuel mass specific momentum
ϕ	equivalence ratio
γ	specific heat ratio
ρ	density of mixture

CHAPTER 1: Introduction of Dissertation

Large bore two-stroke natural gas engines have been used for many years in stationary applications such as gas compression and electric power generation. In the United States alone, there are over 8000 large bore natural gas engines in use. A common configuration of the engines is a two-stroke cycle with direct injection of natural gas into the cylinder. As more stringent air emission regulations have been enacted, reducing the emission levels from these engines and improving the engine efficiency has become an important issue.

The Cooper-GMV, a typical large bore natural gas engine, was investigated in this dissertation. Detailed information about the fluid dynamics and combustion in this engine is limited. One of the research objectives is to understand the port scavenging flow, gas compression, fuel injection, mixing, combustion and pollutant generation in conventional and retrofitted operation of the engine. Another important goal of the engine CFD research is to make suggestions for new designs and operating conditions for engine performance improvement.

Computational Fluid Dynamics (CFD) is a useful tool to achieve these research goals. Validated CFD results provide an inclusive data set to aid in developing comprehensive understanding over the domain of interest. Geometries and conditions of CFD simulations can be easily changed with less expense relative to an experiment. This is an important advantage when modifications of engine components are being considered. Planar laser induced fluorescence (PLIF) experiments using an optical engine were used to validate the CFD simulation results.

Poor in-cylinder mixing due to ineffective fuel delivery is believed to be problematic in this natural gas engine. Insufficient mixing causes unexpected flame extinguishment that leads to CO and CH_2O. In addition, cyclic combustion instability is one of the key contributors to NO_x and CO. Therefore, enhancement of fuel-air mixing using 35 bar high pressure pipeline gas for fuel injection and use of alternative stable ignition systems such as pre-combustion chamber ignition and laser spark ignition are being considered as engine retrofit technologies.

This dissertation consists of four consecutive independent CFD studies to accomplish the suggested research objectives. Each chapter was written in the format of a separate chapter with its own sub-topics.

In chapter 2, the characteristics of natural gas fuel jets emanating from a low pressure conventional poppet valve and from a retrofitted high pressure valve are investigated and compared. The fuel-air mixing in the engine is characterized and quantified by using the parameters such as the flammable volume fraction.

In chapter 3, poppet valve flow is examined. The results indicate that poppet valve is not efficient valve in delivering momentum to the cylinder. Stagnation pressure losses occurring while the fluid passes through the valve are quantified and classified. Improved designs for fuel injection valves are suggested.

The development of a compatible virtual valve which reproduces downstream jet characteristics of the jet issuing from actual valves is described in chapter 4. Instead of including the complex detail of a real valve, a simple converging-diverging type virtual valve is suggested for the engine simulation with high pressure injection.

In chapter 5, the simulation results for three dimensional overall engine simulations for a two-stroke natural gas engine are presented. Some possible retrofit technologies are simulated and analyzed. The retrofit technologies investigated are categorized into two areas: fuel-air mixing enhancement, and alternative ignition systems. High pressure fuel injection enhances the cylinder mixing. The alternative ignition methods change the flame propagation pattern so that the duration of heat release would be shortened. It is observed that NOx forming location in cylinder can be changed by ignition system.

CHAPTER 2: Computational Modeling of Natural Gas Injection

Chapter Abstract

The topic of this chapter is the computational modeling and experimental visualization of gas injection through different poppet valve geometries in a large bore engine. The injection process considered here is accomplished through the use of a poppet valve. The objective of the chapter is to contribute to a better understanding of the significance of the poppet valve and the piston top in controlling the mixing of the injected fuel with the air in the cylinder. In this chapter, the flow past the poppet valve into the engine cylinder is computed using CFD for both a low (4 bar) and a high pressure (35 bar) injection process using unshrouded and shrouded valves. Experiments using PLIF (Planar Laser Induced Fluorescence) are used to visualize the actual fluid flow for the valve geometries considered.

The results indicate that for low injection pressures the gas flow around a typical poppet valve collapses to the axis of symmetry of the valve downstream of the poppet. At high pressure, the gas flow from this simple poppet valve does not collapse, but rather expands outward and eventually flows along the cylinder wall, producing poor mixing in the cylinder. Thus, to obtain satisfactory fuel jet flow at high pressure, the results indicate that a shroud should be employed around the poppet valve to direct the gas into the center of the cylinder. Additional computations show that at top dead center, the flammable mixture fraction for high pressure injection with a shroud in place is significantly greater than for low pressure injection.

2.1 Introduction

The topic of this chapter is the computational modeling of gas injection and in-cylinder mixing in a large bore natural gas fueled engine. The effect of the poppet valve on the mixing of the gas is not fully understood. In contrast to a simple orifice, the poppet valve acts as a bluff body, over which the injected gas flows, producing an annular type flow pattern into the cylinder.

The rudimentary gas injection system is suspected to make these engines exhibit poor mixing. Many of these gas admission systems typically consist of a low-pressure mechanically actuated poppet valve that admits gas directly into cylinder. One technology that has promise for improved engine performance and low emissions is the use of electronically controlled gas injectors operating at high injection pressures. Gas injection at high pressure is believed to increase the momentum transferred into the cylinder, to increase the turbulence levels, and to improve mixing.

In this chapter we examine the injection of natural gas from two types of poppet valves, an unshrouded valve for low pressure injection (Type A) and a shrouded valve for high pressure injection (Type B). Both types of valves are currently used in practice in large bore natural gas fueled engines. In addition, the effect of the injection pressure on the subsequent mixing in the cylinder has not been extensively studied. Natural gas is typically injected at low pressures, 1-3 bar above manifold pressure. Since natural gas pipelines operate at pressures of the order of 35 bar, it is of interest to consider the use of this high pressure gas for direct injection into the engine cylinder.

The CFD model includes the geometry of the gas injection system and some parts of the internal cylinder configuration such as piston top and domed cylinder head with a centrally located, full-lift opened gas admission valve. Off-engine PLIF tests were carried out in the same geometries as those used in the numerical computations for comparison.

There have been many studies of the injection and mixing of sonic gas flow from a simple orifice. As the gas injection pressure/cylinder pressure ratio increases, above a critical pressure ratio of about 1.9, compressible flow phenomena such as rarefaction waves and shock formation need to be taken into consideration. Birch et al. [2.1] used gas chromatography, and Ewan and Moody [2.2] used shadowgraphy to study the behavior of underexpanded jets with injection/cylinder pressure ratios varying from 2 to over 50. Li et al [2.3] used the method of characteristics and CFD modeling to compute the dependence of the gas jet width and the size and location of the resulting Mach disk on the injection pressure ratio.

Many researchers in overall engine performance have used a virtual nozzle as an alternative to modeling the exact geometry of the gas injector. Downstream of the Mach disk, the jet flow field is subsonic, so a virtual nozzle can be sized proportional to the diameter of the Mach disk Recent examples of this approach are given in Ouellette and Hill [2.4] and Mather and Reitz [2.5]. This assumption has an advantage of decreasing the grid density requirements in the near field of the injection nozzle for an engine performance simulation. Numerical models of engine performance incorporating subsonic natural gas injection from a simple orifice into an

engine cylinder are presented by Gaillard [2.6], Han et al. [2.7], and Gundappa et al. [2.8].

The studies of sonic and supersonic gas injection with a poppet valve are much more limited. Boyer et al. [2.9] used schlieren photography to study the injection and scavenging processes in a Cooper GMV engine. The results indicated that the injected gas did not fully mix with the cylinder gases before impinging onto the piston and impinged unmixed as a jet onto the piston top. Two related areas are those of annular propulsive nozzles, which have been studied extensively for aerospace propulsion applications, Conley et al. [2.10], and underexpanded coanda jets, in which a supersonic jet attaches to a adjacent surface, Sawada and Asami [2.11].

There are a number of methods used to quantify the mixing performance of a given injector. In this chapter, two parameters, mixture mass fraction and fuel mass fraction are used. The mass fractions are divided into lean, flammable and rich categories. Papageorgakis and Assanis [2.12] used the mixture mass fraction as a basis of comparison, while Abraham and Magi [2.13] used the fuel mass fraction.

The flammable mixture fraction is defined as the ratio of the burnable mass of mixture to the total mass in the cylinder at any instant. Similarly, the flammable fuel fraction is defined as the ratio of the mass of burnable fuel to the total fuel mass in the cylinder. The mixture and fuel fractions are computed by integrating over all of the computational cells in the cylinder volume with Eq. (2.1) and Eq. (2.2).

$$f_m = \frac{burnable\,mass\,of\,mixture}{total\,mass\,of\,mixture} \qquad (2.1)$$

$$f_f = \frac{mass\ of\ fuel\ included\ in\ burnable\ mixture}{total\ mass\ of\ fuel\ injected} \qquad (2.2)$$

The non-flammable (rich or lean) mixture mass fraction is related to the emissions performance, as it indicates the relative volume of the combustion chamber that may be susceptible to pollutant formation resulting from incomplete combustion. The flammable fuel mass fraction is related to the combustion efficiency, as it indicates the relative mass of fuel that is combustible.

2.2 Computational Experiments

The specific cylinder modeled in this chapter is a Cooper GMV engine cylinder with a 35.5cm cylinder bore and stroke, compression ratio of 9, and rated speed of 300 rpm. The intake ports for this two stroke engine close at 134° before TDC(top dead center), and the exhaust ports close at 103° before TDC. The low pressure poppet valve (Type A) is 23.9mm diameter, with a 6.35mm maximum lift, and the shrouded high pressure valve (Type B) is 18.3mm dia., with a 0.635mm lift. A smaller diameter and lift is required at higher pressures in order to keep an appropriate fuel mass flow rate due to increase in the density of the injected fuel gas. Both types of valves, as they are electronically controlled, have a top hat profile, in which the opening and closing times are much less than the fully open duration. Since the focus of the research was on the fuel injection and mixing, the initial cylinder gases were assumed to be stationary, so that the effect of the scavenging flow is not included in this chapter.

There were three different numerical models developed in sequence. The geometry of the CFD models included the complex details of the fuel poppet valve,

piston crown, and cylinder head. The first model included the valve configuration Type A, the domed head and the cylinder wall but not the piston crown. This allowed investigation of the effect of the injection pressure on the fuel jet behavior in the cylinder in the absence of effects due to jet impingement on the piston. The poppet valve was fixed open at its maximum lift, and a constant injection pressure (4 bar and 35 bar) boundary condition was applied during the methane injection period. The second model represented an off-cylinder configuration with no cylinder head or sidewalls. This was developed in order to study the detailed flow structures in and immediately downstream of the valve. In addition, an experimental rig for this geometry was available for PLIF flow visualization and for subsequent comparison with and validation of the CFD predictions. . The third model included a moving piston and simulated the compression stroke. This allowed investigation of the interaction of the fuel jet with both the moving piston top and the side walls.

The computational domain was discretized by using a variable size grid axisymmetric mesh in the computations. Grid adaptation was used to refine the mesh and locate the rapidly varying expansion and compression structures (including shock waves).

Two CFD solvers were used, Fluent, and Star CD. The turbulence model used was the standard k-ε model. The computations were carried out on a SUN Ultra Sparc workstation.

2.2.1 Injection Pressure Effects on Low Pressure (Type A) Valve Flow

Simulations were performed under two different pressure inlet conditions: a low pressure supply (4 bar, pressure ratio 4:1) and a high pressure supply (35 bar,

pressure ratio 35:1). Computations for both supply pressures were performed for the typical low pressure poppet design we have called Type A. Fig. 2.1 shows the mesh of the axis-symmetric domain used in these calculations, and represents the geometric configuration of the Cooper GMV large bore engine without a piston. Pure methane at inlet pressure is injected through the valve into the cylinder, which is initially filled with quiescent air at 1bar.

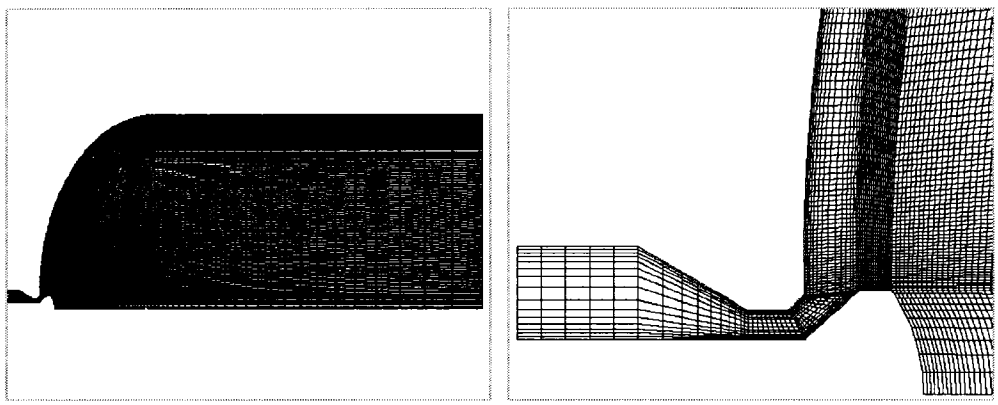

Fig. 2.1 Axis-symmetric cylinder mesh without piston

Flow patterns through the unshrouded valve operating at the low supply pressure and at the high supply pressure show clearly different tendencies. In the case of 4 bar methane injection, shown in Fig. 2.2 (a), (b), (c), fuel jets collapse to the axis with time. On the other hand, the high pressure fuel jets resulting from the 35 bar methane supply spread outward and attach to the wall of cylinder head, as is shown in Fig. 2.2 (d), (e), (f). The left halves of each figure in Fig. 2.2 are the methane mole fraction contours showing the extent of mixing and the right halves are the velocity magnitude contours. The high velocity jet that forms in the high pressure case is of such strength that it never collapses back to the axis and instead impinges on and remains attached to the cylinder wall. Because of this, the high pressure jet would not

impinge on the moving piston if it were present. Since this impingement and interaction with the piston is believed to be critical in enhancing mixing, the unshrouded design at high pressure would have poor mixing performance.

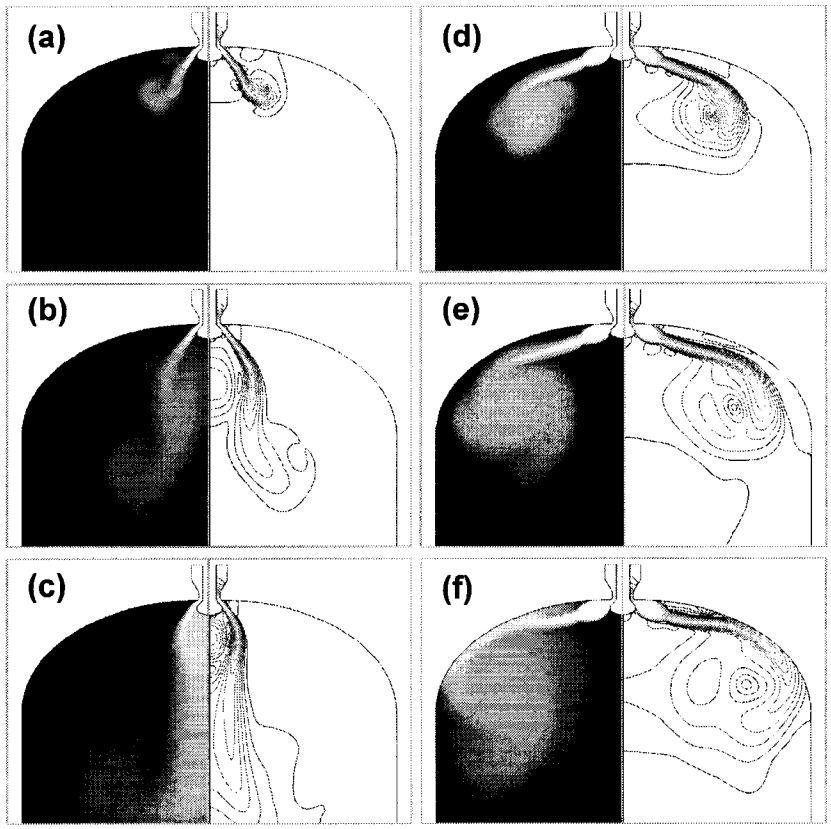

Fig. 2.2 Contours of methane mole fraction and velocity magnitude. (Fig. 2.2 (a)) 4 bar injection case at 1 ms after start of injection. (Fig. 2.2(b)) 4 bar, 4 ms. (Fig. 2.2(c)) 4 bar, 7 ms. (Fig. 2.2(d)) 35 bar, 1 ms. (Fig. 2.2(e)) 35 bar, 2 ms. (Fig. 2.2(f)) 35 bar, 3 ms.

The velocity magnitude contours (on the left hand side) and the pressure contours (on the right hand side) at the early stage of 4 bar methane injection in the near valve region are shown in Fig. 2.3 (a). For the pressure contours, there exist two local maxima, B, D, and two local minima, A, C. The minima, A and C, correspond to the centers of vortices those are induced by the jet on both sides of the jet

boundaries. Point D represents stagnated local pressure occurring at the jet tip. At point B, which is between the wall and the jet, mass accumulation occurs due to the pushing operation of the counter-clockwise rotating vortex at A. Since the jet boundary blocks mass exchange through the jet, a pressure difference between the outer local maximum B and the inner local minimum C results and this pressure gradient across the jet forces the jet to move toward the axis in the low pressure injection case. At a later stage of injection shown in Fig. 2.3 (b), a stationary vortex ring E, which is mainly due to the separation at the valve tip, establishes a position under the valve and pulls down the jet so that it collapses to the axis.

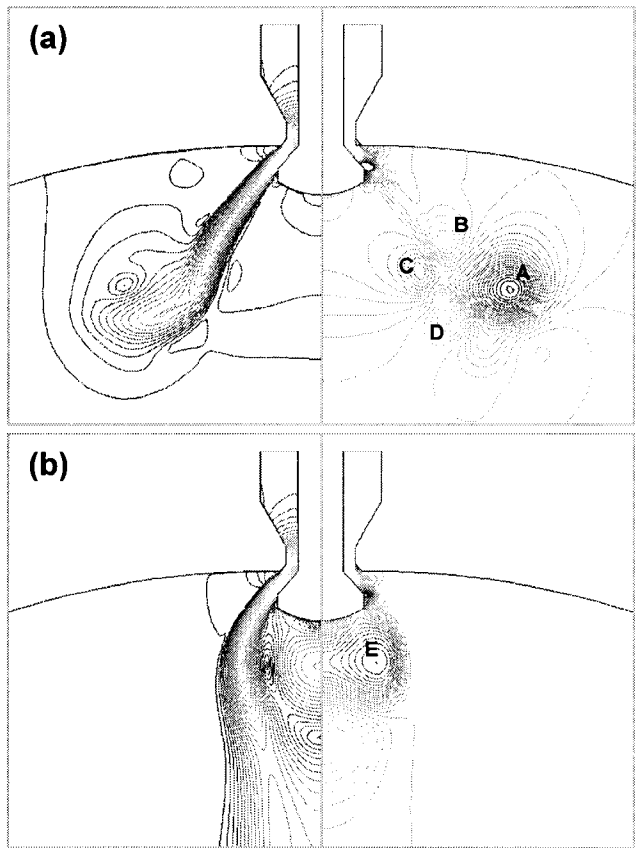

Fig. 2.3 Flow structures just downstream of the valve at 2 ms after start of 4 bar fuel injection (Fig. 2.3(a)) and at 2 sec after start of injection(Fig. 2.3(b)).

Sequential time histories of velocity and pressure contours for the high pressure methane injection case are presented in Fig. 2.4. The flow structures shown downstream of the valve can be used to explain the spreading behavior of the jet. On the left hand sides of the figures are velocity magnitude contours representing the jet structures and on the right hand sides are pressure contours that show forces acting on the jet. Fig. 2.4 (a) shows the jet at 0.6ms after injection starts. Injected fuel is being

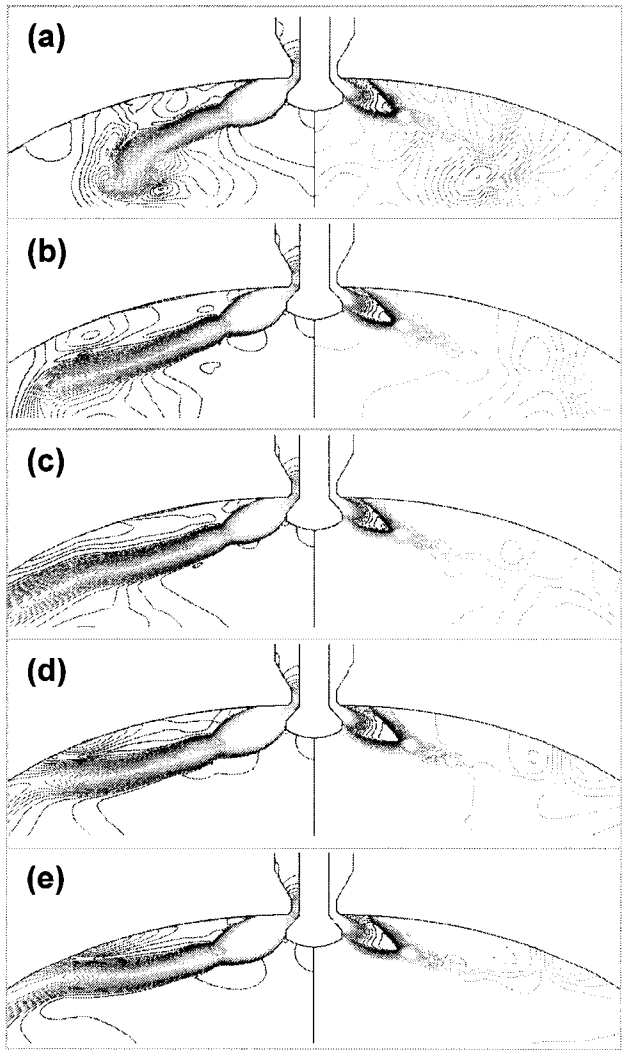

Fig. 2.4 Flow structures downstream of the valve at 0.6 ms after start of 35 bar fuel injection (Fig. 2.4(a)), at 1.2 ms after start of injection (Fig. 2.4(b)), at 1.8 ms after start of injection(Fig. 2.4(c)) , at 2.4 ms after start of injection(Fig. 2.4(d)) and at 3.0 ms after start of injection(Fig. 2.4(e)).

expanded through the valve opening and a shock structure has already formed downstream and to the right of the valve exit. At 1.2ms (Fig. 2.4 (b)) the fuel jet has not yet hit the cylinder wall. There is no pressure gradient across the jet. As the jet approaches the wall (1.8ms, Fig. 2.4 (c)), an isolated circulation region is formed between jet and the wall of cylinder head. When the jet isolates the circulation region completely (2.4ms, Fig. 2.4 (d)), the pressure difference across the jet increases and stagnation occurs at the point of impingement on the wall. In Fig. 2.4 (e) (3.0ms), circulation in the isolated region causes a further decrease in pressure and a significant pressure gradient across the jet is induced. As a result, the fuel jet is pushed to the wall. As time increases the attachment point of jet moves upward, but the upstream structure of the jet is not affected by this behavior downstream. Thus, the main result of the pressure gradient is to cause the jet to be bent upward.

In general, the downstream behavior of the jet is probably of greatest interest as far as mixing is concerned. Still, the flow structures in and near the valve must be examined carefully since they impact directly the nature of the downstream jet. Fig. 2.5(a) and Fig. 2.5(e) show the adapted grid for steady state simulations of low and high pressure injection, respectively. Corresponding Mach number contours are presented in Fig. 2.5(b) and Fig. 2.5(f). Since the minimum Mach number contour scale value is fixed as unity, the area filled with contour lines represents the supersonic region. The fuel flow changes its direction and experiences compression when the bluff body of the valve head is encountered at point A. This causes the complex transonic flow that is seen in this part of the valve for both low and high pressure injection. During the supersonic flow along the slope AB, expansion occurs

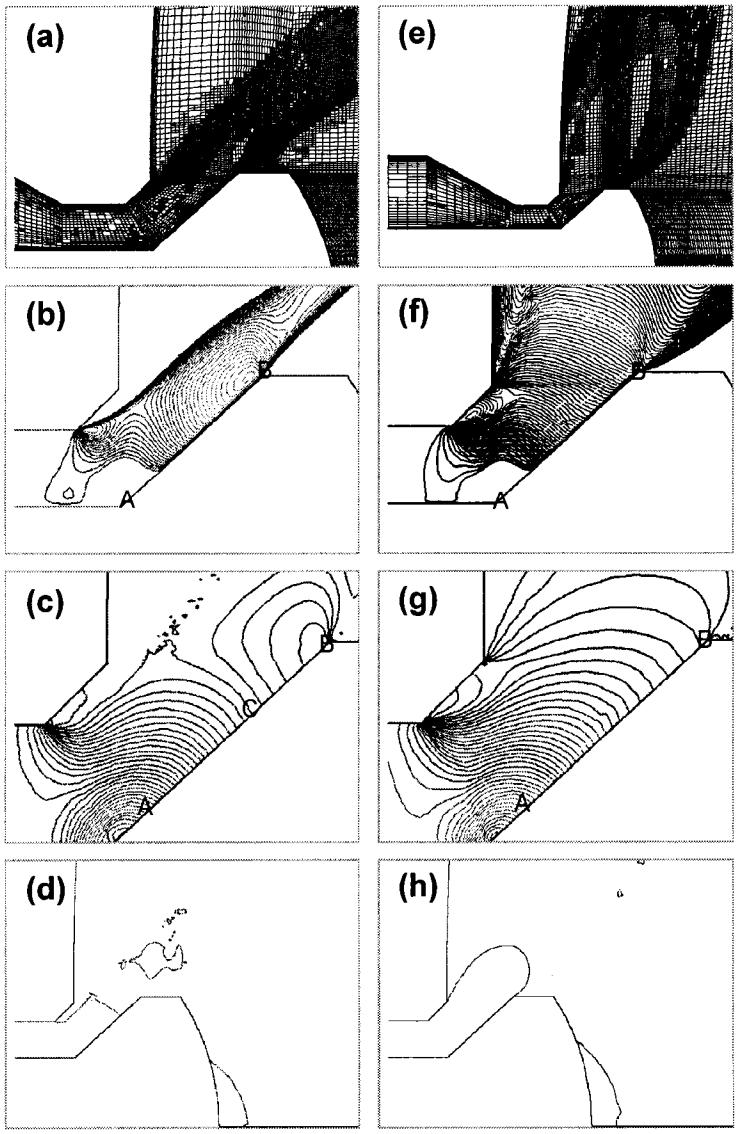

Fig. 2.5 Adapted grids for steady state solution in 4 bar injection case (Fig. 2.5(a)) and in 35 bar injection case (Fig. 2.5(e)). Mach number contours of 4 bar injection (Fig. 2.5(b)) and of 35 bar injection (Fig. 2.5(f)). Static pressure contours of 4 bar injection (Fig. 2.5(c)) and of 35 bar injection (Fig. 2.5(g)). Back pressure line where flow pressure equals cylinder pressure in 4 bar injection case (Fig. 2.5(d)) and in 35 bar injection case (Fig. 2.5(h)).

continuously in both low and high pressure injection cases because the flow area increases in direct proportion to the distance from the cylinder axis. However, the flow patterns are quite different at point B depending on the injection pressure. In the low injection pressure case, the supersonic flow is compressed at point B while for the high pressure injection case the flow continues to expand. Static pressure contours

(Fig. 2.5(c) and Fig. 2.5(g)) show that the low pressure injection flow is over-expanded after passing the point C, in the sense that the pressure falls below that of the cylinder. For this case the flow along the valve center-body is compressed and slowed suddenly by a shock structure at point B, since the pressure at the free jet boundary emanating from point B must match the cylinder pressure. For the high pressure injection case, the flow continues to expand at and downstream of point B through a centered expansion wave structure in order to meet the same free jet boundary pressure condition. Pressure contour lines with a pressure equal to the back pressure, which are shown in Fig. 2.5(d) and Fig. 2.5(h), indicate where the flows are expanded to cylinder pressure.

2.2.2 Simulation of Off-engine PLIF Test Cases

The meshes for unshrouded Type A and shrouded Type B valves used to simulate off-engine PLIF tests are presented in Fig. 2.6. The calculation domain shown includes the gas injector assembly and the piston top in order to match the experimental set-up, though the piston top was not included in the discussion of this section. Since acetone seeded nitrogen was injected into ambient air in the experimental tests, nitrogen was chosen as the injection gas in these computations instead of natural gas. In each simulation, gas was injected into quiescent air at atmospheric pressure. As can be seen in Fig. 2.6, the high pressure injection design included a shroud to direct the valve outflow in the axial direction and reduce the radial expansion seen earlier in Fig. 2.4.

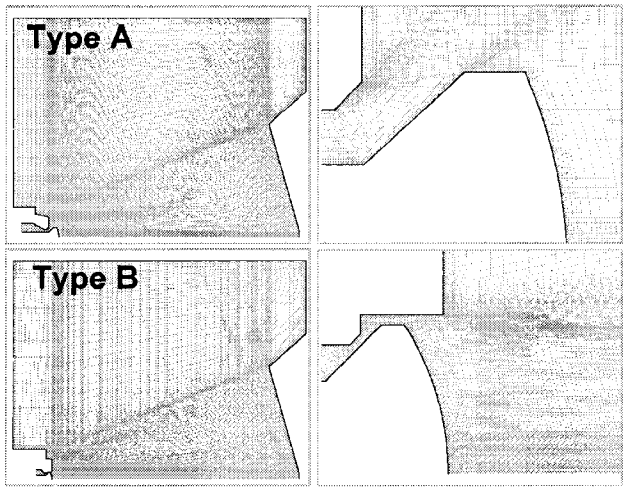

Fig. 2.6 Meshes for simulation of the off-engine PLIF tests.

The CFD computations were validated through comparison with the PLIF experimental results as shown in Fig. 2.7 and Fig. 2.8. The details of the PLIF imaging experiment are described further in Olsen et al. [2.14]. In this set of computations, the jet is injected into an open cavity with no side walls. The cylinder pressure is atmospheric, so that the injection/cylinder pressure ratio is 4 for the low pressure case, and 35 for the high pressure case. For the PLIF images the bright areas indicate regions of high intensity fluorescence from the acetone seed and thus also represent high concentrations of injected gas. For the CFD images the bright areas are direct representations of high injected gas concentrations as taken from the computational results.

Fig. 2.7 shows the comparison of the results for transient behavior from the computational simulation and from the experiments for the low pressure injection case. The left side of each frame is the PLIF image, while the nitrogen concentration contours from the computations appear on the right side. The image sequences are approximately 0.5 ms apart. The flow features contained in the CFD and the PLIF

images are very similar. As the gas is injected into the cylinder, it flows over the poppet valve initially forming an S-shaped conical profile with a leading vortex, as shown in the first three images. The conical profile collapses to the axis downstream of the poppet valve, and the body of the jet behind the leading vortex has a relatively constant diameter. The vortex increases in size as it penetrates into the cylinder, and mixes with the cylinder gas.

Fig. 2.8 presents the PLIF images and the nitrogen concentration contours of the simulation for the high pressure injection case. The impact of adding a shroud for the high pressure design is shown in this figure. The contrast between the high pressure jet with and without a shroud in place (see Fig. 2.4 for high pressure unshrouded poppet injection) is striking. With the shroud, the jet has a general similarity to an axially directed jet emanating from a hole of circular or annular cross section. Here again a general qualitative agreement between experiment and prediction is apparent. A repeating pattern of low concentration zones followed by high concentration zones along the jet axis is evident in both sets of images. The location and extent of these zones correspond quite well at least for the first few occurrences. The flow downstream of the valve exit is supersonic and the high and low concentration zones result from the alternate reflection of compression and expansion waves from the axis and from the free boundary of the jet. The strength of successive compressions and rarefactions decreases due to viscous and turbulent mixing losses. This kind of reflection pattern has long been observed in axially symmetric supersonic free jets. The jet diameter and spread rate with distance along the axis are at least approximately the same for both PLIF and computational-images.

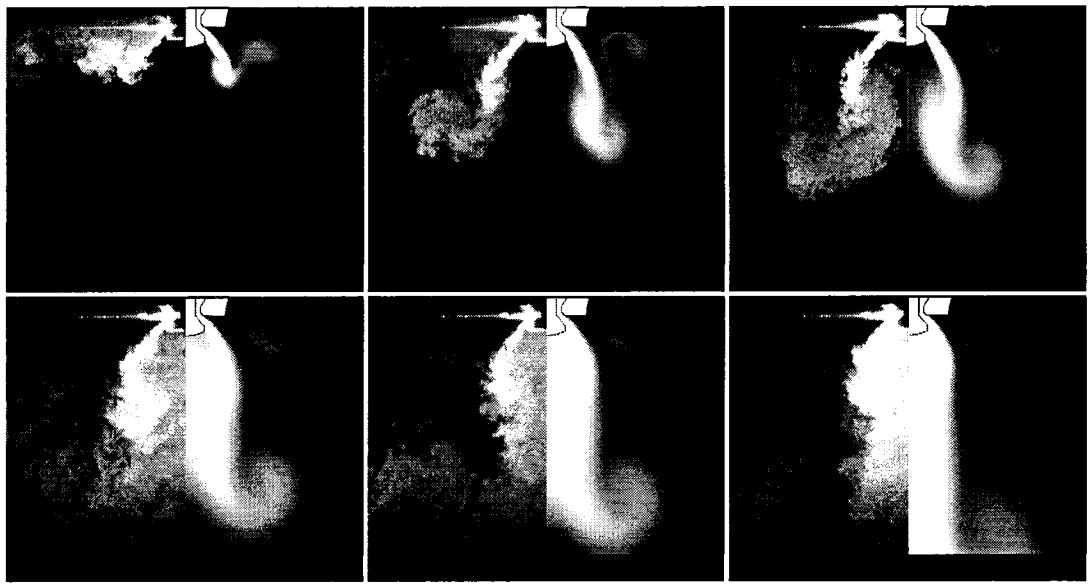

Fig. 2.7 Comparison of the results from PLIF experiments and from CFD computations for 4 bar nitrogen injection.

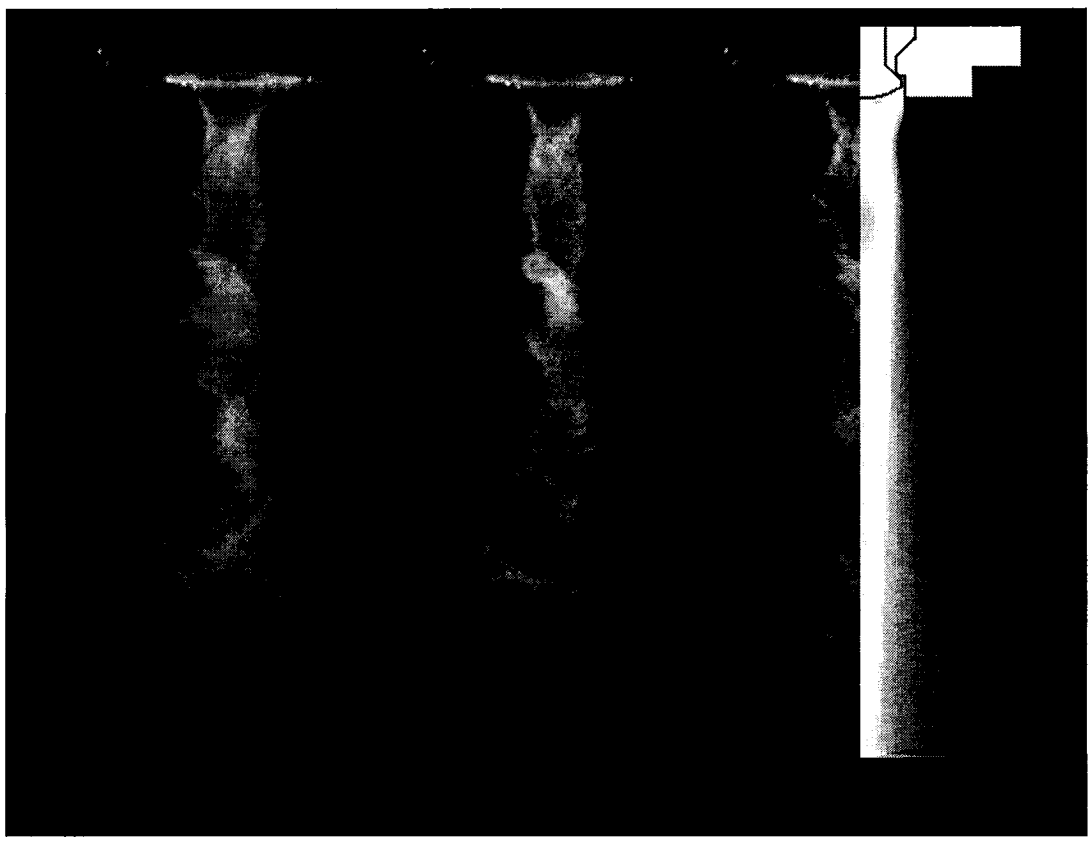

Fig. 2.8 Comparison of the results from PLIF experiments and from CFD computations for 35 bar nitrogen injection.

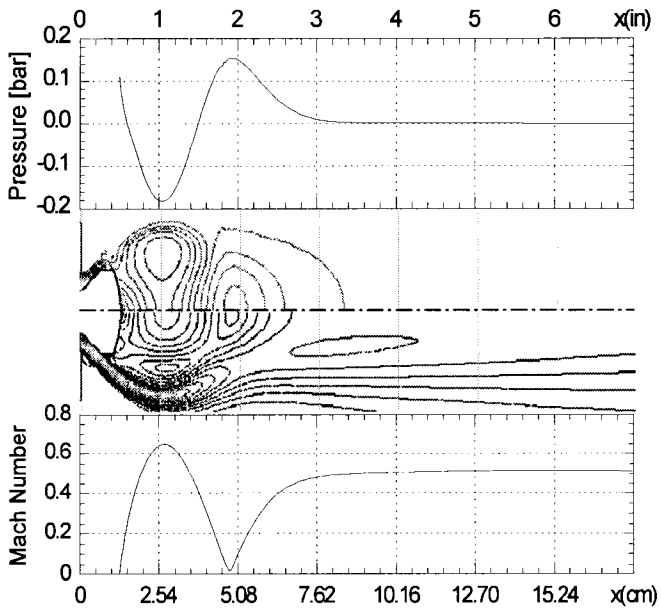

Fig. 2.9 Contours of static pressure and Mach number and their axial profiles for 4 bar injection case, steady flow computation

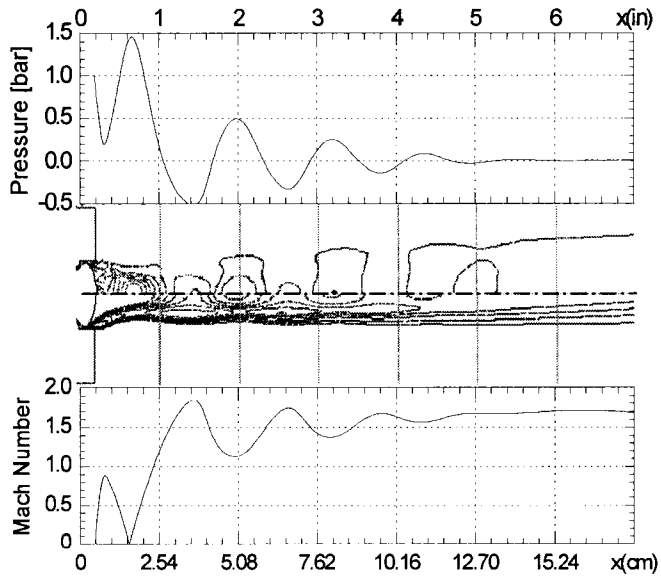

Fig. 2.10 Contours of static pressure and Mach number and their axial profiles for 35 bar injection case, a steady flow computation

Contours of static pressure and Mach number for the low pressure injection case are presented in Fig. 2.9 for a steady flow computation. In the same figure the corresponding axial profiles of static pressure (gage) and Mach number are also shown. Fig. 2.10 shows similar contours and profiles for the high pressure injection case. One of the important differences between the downstream structures shown in these figures is that the downstream jet is subsonic for the low pressure injection case while the high pressure injection case results a supersonic jet with a Mach number of 1.7. As mentioned in previous section, the annular jet which occurs for low pressure injection collapses and begins to merge at about 5cm (2in) downstream from inlet. Static pressure along the axis reaches a local maximum at this stagnation point and decreases monotonically to the cylinder pressure. In contrast, the supersonic jet occurring for the high pressure injection case has a shroud to direct the jet to the center and is repeatedly accelerated and decelerated due to the complex rarefaction and compression waves which result.

Axial velocity profiles in the radial direction are plotted at seven equally spaced downstream locations for low pressure injection and for high pressure injection, respectively, in Fig. 2.11(a) and Fig. 2.11(b). Axial momentum flux distributions at the same locations are also presented in Fig. 2.11(c) and in Fig. 2.11(d). These figures illustrate the spatial development of the jets. The initially annular jets are eventually transformed into typical bell shape profiles due to turbulent and molecular mixing in both cases. In the case of high pressure injection, the higher momentum inside the high pressure jet retards this transformation and, as a result of this, the bell shaped profile occurs much further downstream. The high

pressure jet has a much larger velocity gradient than the low pressure jet because the jet radius is smaller and the core velocity is larger. This fact is important in that a large velocity gradient implies a good source for turbulence. Since high level turbulence is believed to enhance fuel-air mixing and flame propagation, high pressure injection may have an advantage over low pressure injection in engine performance even in the absence of piston impingement effects. The axial momentum transfer rate is about 45 kg m s^{-2} for the low pressure injection case and about 100 kg m s^{-2} for the high pressure injection case respectively.

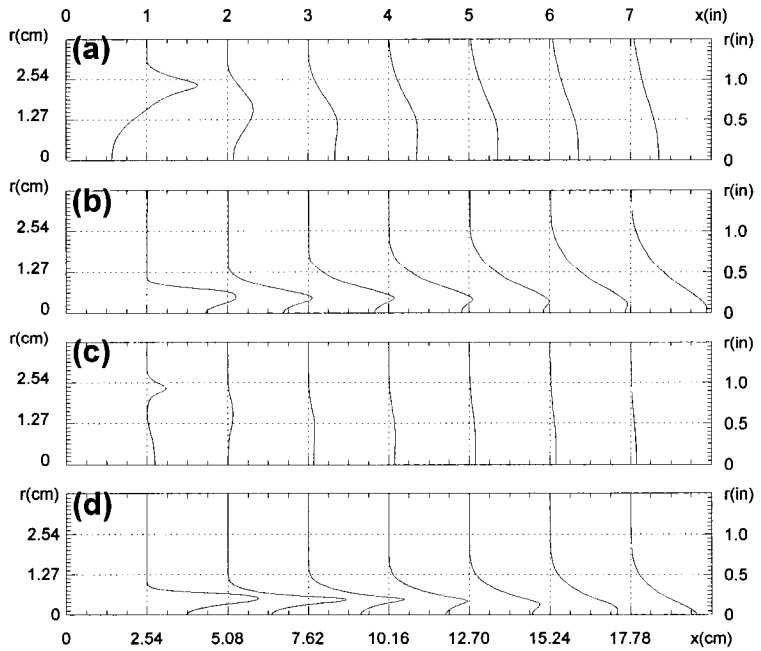

Fig. 2.11 Axial velocity profiles in radial direction at seven equally spaced downstream locations for 4 bar injection in valve Type A (Fig. 2.11(a)) and for 35 bar injection in valve Type B (Fig. 2.11(b)). Corresponding axial momentum flux profiles for 4 bar injection in valve Type A (Fig. 2.11(c)) and for 35 bar injection in valve Type B (Fig. 2.11(d)).

Mass flow rates and energy flow rates passing through the same seven axial locations, which are given by integrating the momentum and energy fluxes across the radial profiles, are plotted in Fig. 2.12. In spite of dissimilarity in the valve geometries and the operating pressure, injected fuel mass rates are almost the same in both gas admission systems. This is reflected by the total mass flow rates shown near the injection valves. The mass entrainment rate of the high pressure jet is higher, which implies that more air is being mixed into the fuel stream. Changes in the kinetic energy flow rate and enthalpy flow rate show opposite phase in both valve flows. This is to be expected and reflects the reversible and irreversible exchange between kinetic and thermal energy by waves and dissipation. In connection with this, the stagnation enthalpy flow rate, the sum of flow rates of kinetic energy and enthalpy, shows a small, monotonic increase in the downstream direction due to enthalpy inflow by entrainment. At the location where the high pressure valve flow

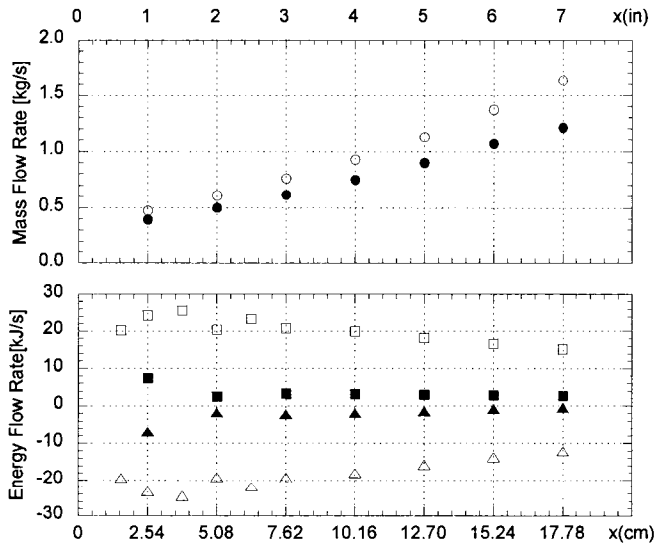

Fig. 2.12 Mass flow rates and energy flow rates integrated at seven different axial locations. Mass flow rate in 4 bar injection in valve Type A (●) and in 35 bar injection in valve Type B (○). Kinetic energy flow rate in 4 bar injection in valve Type A (■) and in 35 bar injection in valve Type B (□). Enthalpy flow rate in 4 bar injection in valve Type A (▲) and in 35 bar injection in valve Type B (△).

begins to assume a bell shaped profile there is approximately six or seven times as much kinetic energy in the jet as there is in the low pressure jet at the same axial location.

2.2.3 In-cylinder Mixing Simulation with Moving Piston

Fig. 2.13 shows the grid systems designed to simulate gas injection in a cylinder with a moving piston. In this final set of computations the piston moves from bottom dead center (BDC) to top dead center (TDC). The unshrouded valve, Type A, was used for low pressure injection and the shrouded Type B for high pressure injection with a 35.5cm cylinder bore and stroke. These axis-symmetric simulations were designed to investigate the interaction between the poppet valve jets and the moving piston top in the cylinder. The effectiveness of fuel-air mixing for each injection system was examined by calculating flammable fuel fractions and flammable mixture fractions during and after the injection process for both cases. Scavenging flow was not considered and initial conditions for quiescent air-filled cylinder at 1bar were assumed.

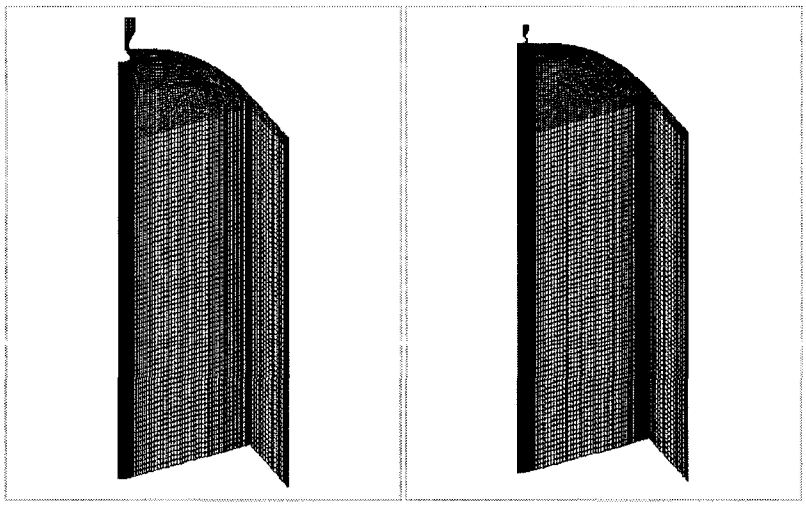

Fig. 2.13 Grid systems of axis-symmetric domain for in-cylinder mixing simulations with moving piston.

At an engine speed of 300 rpm, the compression stroke takes 100 ms. Two different injection cases were computed, a "short" duration of 20 degrees crank angle (22 degrees for the low pressure Type A case), which corresponds to 11 ms, and a 32 degree "long" duration of 18 ms, with the start of injection at about 120 degrees before TDC. The specific start of injection (SOI) and injection duration are given in Table 1.1. The resulting injected fuel mass and overall equivalence ratios, which correspond to lean engine conditions, are given in Table 2.1.

Table 2.1 In-cylinder mixing at top dead center

	P_i (bar)	SOI ($^\circ$ btdc)	Duration ($^\circ$)	m_f (g)	ϕ	f_m	f_f
Short	35	115	20	1.81	0.66	0.84	0.95
	4	120	22	1.42	0.52	0.62	0.87
Long	35	122	32	2.89	1.06	0.98	0.99
	4	122	32	2.06	0.76	0.80	0.95

A lean mixture in a cell is defined as one with an equivalence ratio less than 0.5, a flammable mixture has an equivalence ratio between 0.5 and 2.0, and a rich mixture has an equivalence ratio greater than 2.0. Thus, lean, rich and flammable mixture and fuel fractions can be computed at all times during the injection and mixing processes. Our definitions of lean, rich and flammable mixtures were based on laminar flame propagation limits at atmospheric pressure and nominal atmospheric temperature. At top dead center, both pressure and temperature are substantially higher. It is generally observed that the lean limit is not strongly affected by

increasing pressure and temperature. Since our basic mixing problems exist on the lean limit our conclusions should still be valid in the main.

The change in the flammable mixture fraction and the flammable fuel fraction during the compression stroke for the short duration low and high-pressure cases is shown in Fig. 2.14 and Fig. 2.15. Even though the amount of the flammable mixture increases faster in the high pressure injection through valve Type B than in the low pressure injection with the valve Type A, the mixing rate decreases with time in both cases. High flammable mixture fraction increasing rates appear about 5 degrees crank angle after start of injection and it is kept for about 20 degrees. These linear sections of the curves correspond to the jet impinging periods. It indicates that jet impingement on the piston top enhances mixing and that the higher momentum jet results in the steeper linear section which means the higher mixing rate. In interpreting this result, it can be pointed out that the high pressure jet has about 2 times more momentum flow rate and 6 times more kinetic energy flow rate than the low pressure jet as it impinges on the piston top. Examination of the computational results indicates that one consequence of this additional momentum and energy is to produce more vigorous vortex structures in the cylinder as well as more substantial gas flow along the piston surface and cylinder wall. Values of the flammable mixture fraction (f_m) and the flammable fuel fraction (f_f) at TDC for both low and high pressure injection and for short and long injection durations are listed in the last two columns of Table 2.1.

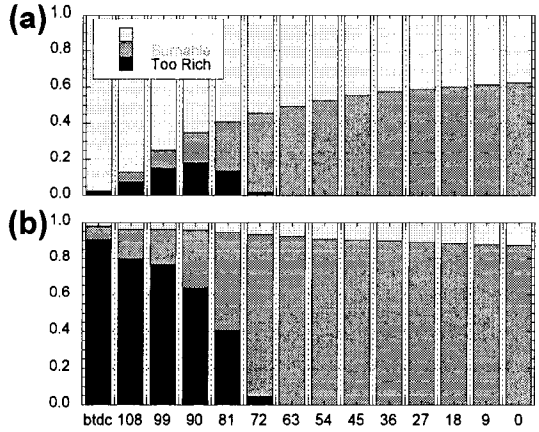

Fig. 2.14 Flammable mixture fraction (Fig. 2.14(a)) and flammable fuel fraction (Fig. 2.14(b)) as a function of piston location in 4 bar injection case.

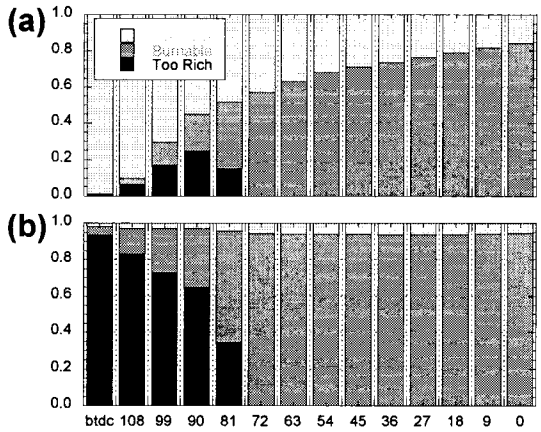

Fig. 2.15 Flammable mixture fraction (Fig. 2.15(a)) and flammable fuel fraction (Fig. 2.15(b)) as a function of piston location in 35 bar injection case.

As can be seen by examination of the column labeled "m_f (g)" in Table 2.1, the total mass of fuel injected is substantially less for the low pressure injection cases when the valve open times are approximately the same. Of course, this will affect the flammable fuel and mixture fractions and prejudice the results in favor of the high pressure design. In order to compare mixing results for equal total fuel mass amounts

for both high and low pressure injection, several additional computations were run with additional injection durations. Results of these calculations are presented in Fig. 2.16. In the Figure, flammable mixture fractions at top dead center (TDC) in low pressure injection cases and high pressure injection cases with different injection durations are plotted versus the amount of injected fuel. Start of injection (SOI) was fixed as 120 degrees before TDC. The computational results predict that for all values of total fuel mass injected, high pressure operation is superior to low pressure operation in increasing flammable mixture fraction.

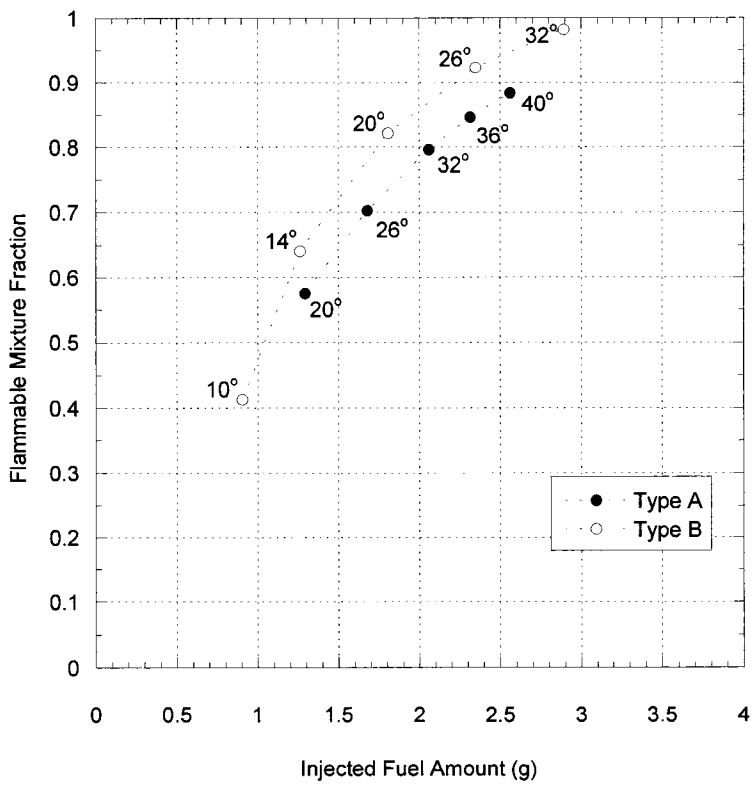

Fig. 2.16 Flammable mixture fractions at top dead center (TDC) with different injection durations. Numbers beside the makers are corresponding durations in crank angle degrees.

The spatial distribution of the local fuel mole fraction at top dead center for the long duration (32 crank angle degrees) injection is shown in Fig. 2.17. The lean areas for both pressure conditions occur in the interior of the cylinder. This is due to the redirection of the injected fuel from the top of the piston toward the sides of the cylinder. The relatively greater velocity of the high-pressure fuel jet allows for larger recirculation of the jet into the center of the cylinder and a corresponding larger fuel fraction in the cylinder center.

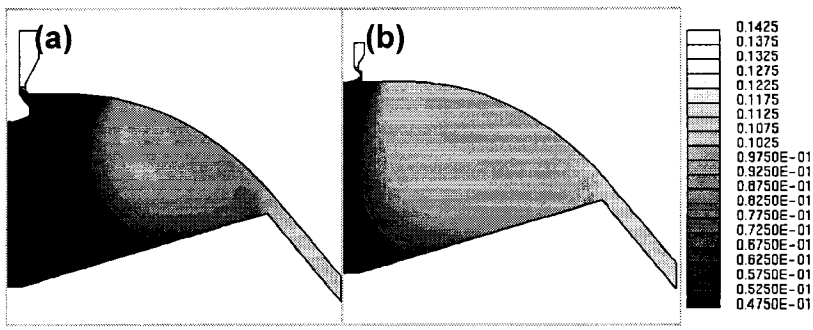

Fig. 2.17 Contours of methane mole fraction [mole/mole] at top dead center in 4 bar injection case (Fig. 2.17(a)) and in 35 bar injection case (Fig. 2.17(b)).

The spatial distribution of the turbulent kinetic energy (m^2/s^2) at top dead center for the long duration injection computations is shown in Fig. 2.18. The turbulent kinetic energy is of interest as minimization of the combustion duration in an engine requires a high turbulent intensity. The high pressure jet creates increased turbulent kinetic energy relative to the low pressure jet, with the average value being of 7.8 m^2/s^2 as compared to the average low-pressure value of 3.8 m^2/s^2. Clearly, at least some of the additional directed kinetic energy present in the high pressure injection jet shows up as additional turbulent kinetic energy at TDC.

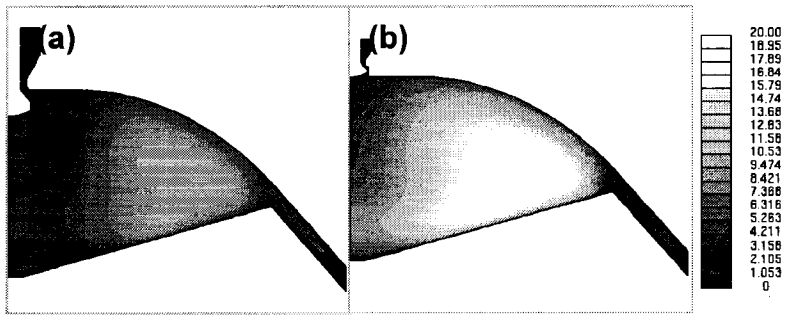

Fig. 2.18 Contours of turbulent kinetic energy [m^2/s^2] at top dead center in 4 bar injection case (Fig. 2.18(a)) and in 35 bar injection case (Fig. 2.18(b)).

CHAPTER 3: Improvement of Poppet Valve Injection Performance

Chapter Abstract

Poppet valves have been used as fuel delivery mechanisms in internal combustion engines due to their excellent sealing characteristics. For example, in large-bore stationary natural gas engines, gas is directly injected by a poppet valve into the engine cylinder.

The objectives of this paper are to show that a significant amount of stagnation pressure is lost during the gas flow through a conventional poppet valve and to suggest design improvements to obtain more efficient poppet valves with reduced stagnation pressure loss. In this paper, simple converging-diverging nozzles are incorporated into the poppet valve configuration to reduce the stagnation pressure loss originating from compressible flow structures.

Numerical simulations of the gas flow through various poppet valve geometries were performed. Both push and pull poppet valve geometries with nozzle were studied. The stagnation pressure losses, momentum delivery downstream and downstream flow characteristics of the jets from conventional poppet valves and the modified valves were compared. A pressure-based valve injection efficiency was defined and used to compare the valve injection performance. A mixing fraction parameter was also defined to compare valve performance in a moving piston simulation.

The results indicate that a conventional poppet valve is an inefficient mechanism to deliver momentum to the fuel-air mixture. Comparison of the results

indicates that it is possible to make significant improvements of injection performance in momentum delivery by incorporating well-designed nozzles into the poppet valve geometry.

3.1 Introduction

One of mixing enhancement technologies currently used is high pressure fuel injection. Natural gas is typically injected at low pressures, 1-3 bar above manifold pressure. Since natural gas pipelines operate at pressures of the order of 35 bar, it is of interest to explore the use of pipeline gas at high pressure as the source for injection fuel.

The objective of this chapter is to show that conventional poppet valves have inherent design flaws that severely limit their performance at both low and high injector pressures and to suggest guiding principals for designing more efficient fuel injection valves. Kim et al. [3.1] examined the injections of natural gas from these two typical types of poppet valve, an unshrouded low pressure injection valve (4bar, Fig. 3.1(a)) and a shrouded high pressure injection valve (35bar, Fig. 3.1(b)). This study was also performed for these two types of typical valves which are in use. These were taken as the baseline for comparison with improved designs. Fig. 3.1(c) and Fig. 3.1(d) show the simple converging-diverging nozzles designed to be operated at the same injection pressures as those of the conventional poppets. In addition two modified poppets were designed for each injection pressure. One of these was just a straightforward modification achieved by simply attaching the converging-diverging nozzle downstream of the conventional poppet valve as showed in Fig. 3.1(e) and Fig. 3.1(f). The other one had the same nozzle, but employed a

major change in poppet actuation. This involved simplification of the fuel flow path in the subsonic region before the throat, and substitution of a pull-open poppet for the conventional push-open configuration (Fig. 3.1(g) and Fig. 3.1(h)).

The computational domain was discretized by using a variable size grid axisymmetric mesh in the computations. Grid sensitivity computations indicated that at least ten grid points across the nozzle orifice were required in order to reduce the sensitivity of computational predictions to grid size in the nozzle region to an acceptable level. Two CFD solvers were used, Fluent, and Star CD. The turbulence model used was the RNG k-ε model for static simulations and the standard k-ε model for moving piston simulations. The computations were carried out on a SUN Ultra Sparc workstation.

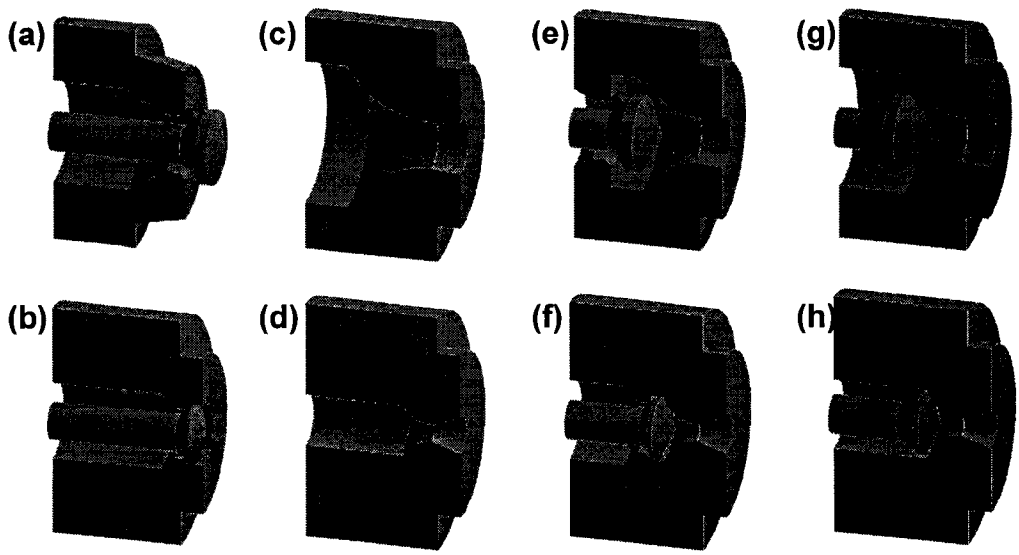

Fig. 3.1 Schematics of the conventional poppet valves currently in use on a large-bore engine (Fig. 3.1(a) for low pressure injection and Fig. 3.1(b) for high pressure injection) and schematics of their modifications (Fig. 3.1 (c), (d), (e), (f), (g), (h)) for low and high pressure natural gas injection.

3.2 Nozzle Design

A significant amount of stagnation pressure loss occurs during the gas flow through a conventional poppet valve. As reported by Kim et al. [3.1], the speed of the fuel jet issuing from conventional poppet valves was much less than theoretically expected from the nominal injection pressure ratios of 4.06:1 for the low pressure case and 35.0:1 for the high pressure case. In the low pressure injection case, the downstream fuel jet was completely subsonic, even though a simple one dimensional isentropic flow relation predicted that the downstream flow could be supersonic with a Mach number as high as 1.60. This implies that there is a considerable amount of stagnation pressure loss as the fuel jet passes through the poppet valve. Stagnation pressure losses occur both internally and externally relative to the valve by a number of mechanisms such as mixing, dissipation and shocks.

Supersonic stagnation pressure losses originating from shocks can be reduced by introducing a properly designed nozzle. For this study, a converging-diverging nozzle having a conical diverging section was chosen. For simplicity, quasi-one-dimensional isentropic flow relations and ideal gas relations were used to calculate the dimensions of these nozzles operated at a given supply pressure p_0. Fig. 3.2 presents a schematic showing the nozzle design parameters such as throat radius r^*, nozzle exit radius r_e and the given flow conditions. The cone angle for the conical diverging section is fixed as 6 degrees. The nozzle throat area and its corresponding throat radius were determined by Eq. (3.1)

$$A^* = \frac{\dot{m}_f}{p_0}\sqrt{\frac{RT_0}{\gamma}}\left(\frac{\gamma+1}{2}\right)^{\frac{\gamma+1}{2(\gamma-1)}} \tag{3.1}$$

Eq. (3.1) gives throat area A^* for a given fuel mass flow rate $\dot{m}_f$. Nozzle exit area and its corresponding radius were calculated using the well-known area-Mach number relation shown in Eq. (3.2).

$$\left(\frac{A_e}{A^*}\right)^2 = \frac{1}{M_e^2}\left[\frac{2}{\gamma+1}\left(1+\frac{\gamma-1}{2}M_e^2\right)\right]^{\frac{(\gamma+1)}{(\gamma-1)}} \tag{3.2}$$

where A_e is nozzle exit area required to expand the fuel jet to the cylinder pressure at exit. Nozzle exit Mach number M_e is determined using one-dimensional flow relation shown in Eq. (3.3) for a given injection pressure ratio p_0 / p_e.

$$M_e = \sqrt{\frac{2}{\gamma-1}\left(\left(\frac{p_0}{p_e}\right)^{\frac{\gamma-1}{\gamma}} - 1\right)} \tag{3.3}$$

Table 3.1 presents the dimensions and the conditions of the nozzles which are designed for low pressure (LP) injection and high pressure (HP) injection respectively. For the low pressure case the exit Mach number predicted by isentropic relations is 1.60, and for the high pressure case, the exit Mach number is 2.91.

Table 3.1 Operation conditions and dimensions of designed nozzles

	p_o/p_e	$\dot{m}_f$ (kg/s)	r^*(mm)	r_e(mm)	M_e
LP nozzle	4.06	0.113	7.18	8.08	1.60
HP nozzle	35.0	0.132	2.64	5.71	2.91

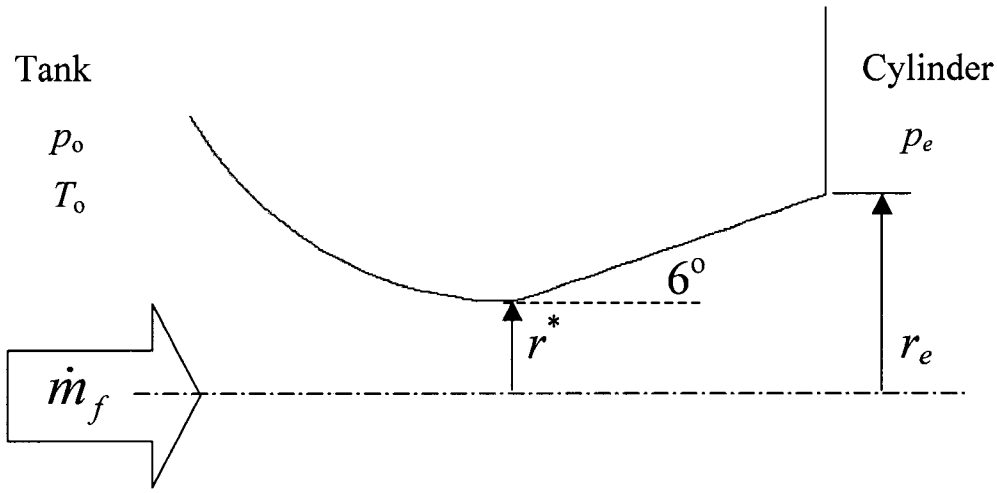

Fig. 3.2 Design parameters and conditions for the simple converging-diverging nozzles.

3.3 Comparison of Momentum Delivery

Numerical simulations for fuel injections through the eight valve/nozzle configurations were carried out to compare the injection performance of the valve/nozzle configurations with respect to momentum delivery downstream. Methane was injected through each valve into an open cylinder which was kept at a constant pressure of one bar. Since the cylinder pressure varies slowly with a mean value close to one bar, during injection in these engines, the constant cylinder pressure assumption is reasonable computational approximation. The computational domain included the valve geometries and the piston top but not the cylinder wall. Near valve regions of the grids used for these numerical simulations are shown at Fig. 3.3.

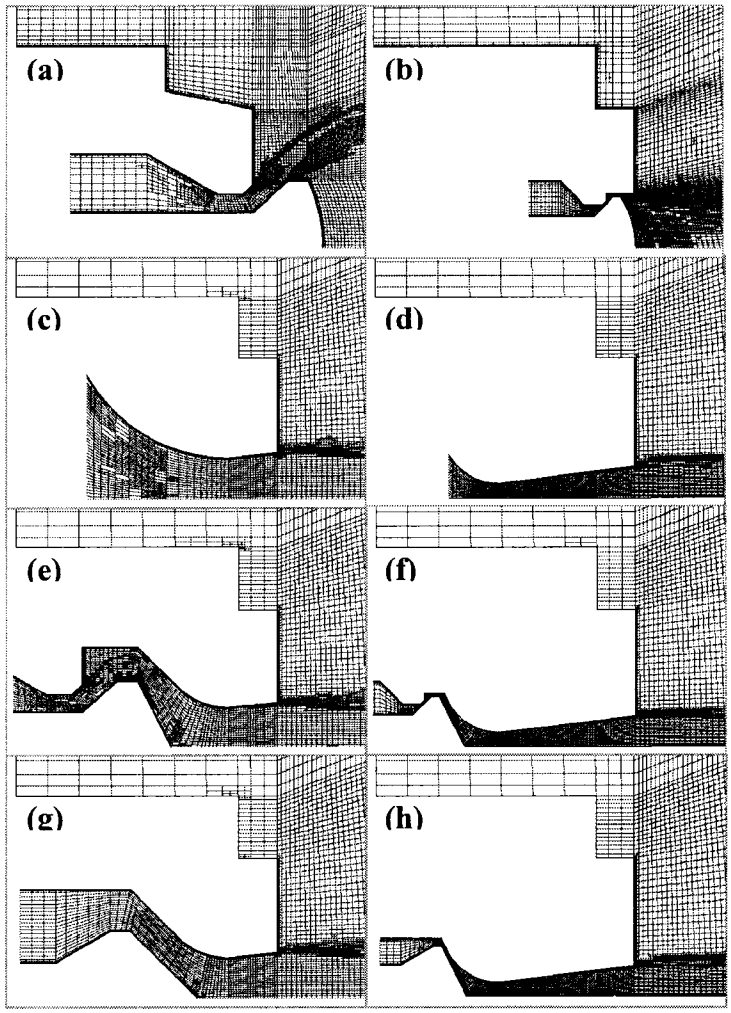

Fig. 3.3 Near valve regions of grids used in axisymmetric computations for conventional valve injection (Fig. 3.3(a) for low pressure and Fig. 3.3(b) for high pressure), for simple converging-diverging nozzle injection (Fig. 3.3(c) for low pressure and Fig. 3.3(d) for high pressure), for injection from push-open poppet with nozzle (Fig. 3.3(e) for low pressure and Fig 3.3(f) for high pressure) and for injection from pull-open poppet with nozzle (Fig. 3.3(g) for low pressure and Fig. 3.3(h) for high pressure).

Because the injection jet flow approaches a local steady state within 2~4ms for all tested valves and the fuel injection duration of these engines is about 11ms, most of the comparisons were carried out at 11ms after start of injection. At the axial location 18cm from the nozzle exit all the jets presented here had developed typical

bell-shaped profiles and were still free from the effect of piston top located at 30cm downstream.

Radial distributions of axial velocity and axial momentum flux at the axial location 18cm from the nozzle exit are compared for the low pressure valves in Fig. 3.4 respectively. The jet issuing from the low pressure conventional poppet valve shows a blunter core profile and larger jet radius than the other jets. This is due to the initial jet profile difference. As discussed in Kim et al. [3.1], the jet flowing from the conventional poppetvalve has an initial annular jet radial profile just downstream of the poppet and then collapses to the centerline axis. The maximum speed for this type of jet occurs considerably well off the centerline axis. In contrast, the converging-diverging nozzle produces a one-dimensional flow at the exit of the nozzle. In terms of core jet speed, the addition of the nozzle brought remarkable improvement in injection performance of the valve.

The velocity of the jet issuing from the push-open poppet equipped with a nozzle is much greater than that of the conventional poppet jet and it reaches and exceeds sonic velocity downstream. The pull-open poppet equipped with a nozzle injects an even more energetic supersonic fuel jet with a velocity profile almost the same as the flow from the simple reference nozzle. This implies that introducing the nozzle inboth the push-open and the pull-open valves can reduce a significant amount of the stagnation pressure loss originating from the downstream shock structures in conventional poppet valves. As discussed in the next section, there also is significant subsonic pressure loss upstream of the nozzle throat in the push-open configuration

while there is nearly no stagnation pressure loss in the subsonic section of the pull-open poppet.

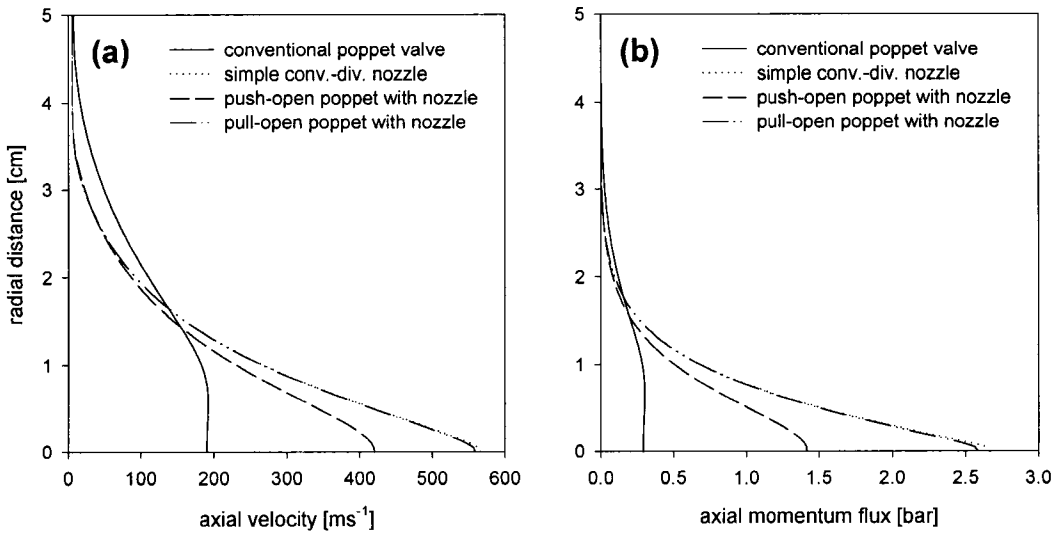

Fig. 3.4 Comparisons of axial velocity profiles (Fig. 3.4(a)) and of axial momentum flux profiles (Fig. 3.4(b)) for the tested low pressure injection valves at 18 cm downstream from nozzle exit at 11 ms after start of injection.

Similarly, Fig. 3.5 show the comparisons of axial velocity profiles and of axial momentum flux profiles for the high pressure injection valves. The high pressure injection jet profiles in Fig. 3.5 generally exhibit the same tendencies as the low pressure jets. Note that due to the shroud, the poppet jet diameter is about the same size as the nozzle flows. In conventional high pressure poppet valve injection, the fuel jet is directed to the center by the shroud without which the jet willnot collapse and hit the piston. Even though a larger jet radius implies a larger peripheral area through which the entrained air flows, the entrainment rate of the air with the fuel stream of

the conventional poppet jet is not so much different with those of the others due to its smaller speed and transverse velocity gradient.

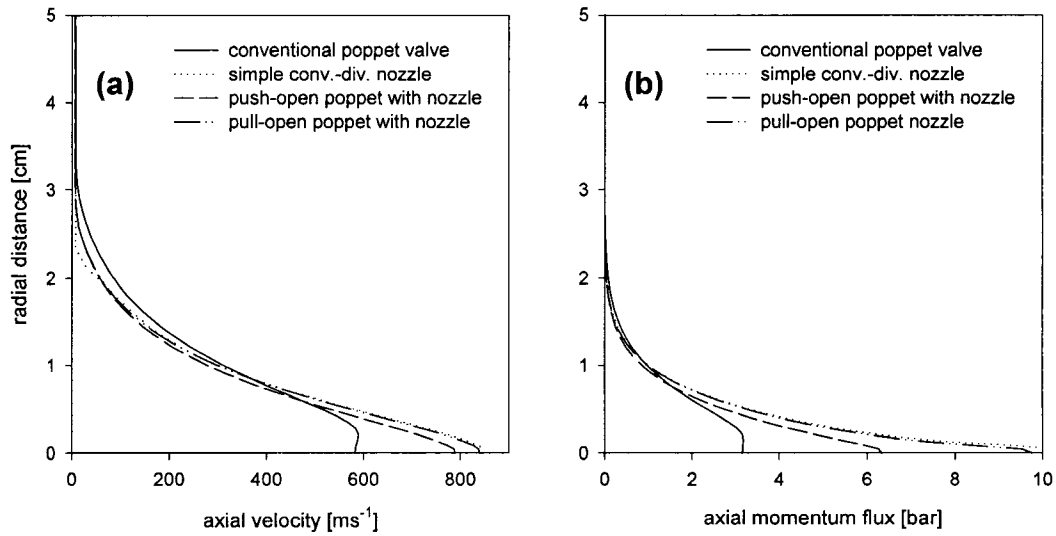

Fig. 3.5 Comparisons of axial velocity profiles (Fig. 3.5(a)) and of axial momentum flux profiles (Fig. 3.5(b)) for the tested high pressure injection valves at 18 cm downstream from nozzle exit at 11 ms after start of injection.

One of the main functions of the fuel injection system is conversion of the fuel pressure to jet momentum, as overall mixing is related to the momentum injected into the fuel-air mixture. The axial momentum flux profiles shown at Fig. 3.4(b) and at Fig. 3.5(b) were integrated using Eq. (3.4) over the jet cross sectional area to get the axial momentum flow rate, $\dot{p}_x$, which is shown in Table 3.2.

$$\dot{p}_x = \int_0^\infty \rho v_x^2 2\pi r dr \qquad (3.4)$$

The axial momentum delivery rate, $\dot{p}_x$, of push-open valves is less than the other nozzle flows, and for the high pressure push-open valve it is even smaller than the conventional poppet. This signifies that the subsonic stagnation pressure loss should be a consideration in the design of supersonic nozzles. This decrease of

injection performance in the push-open configurations is caused mainly by the reduction of the fuel mass injection rate which can be easily increased by increasing the nozzle throat area through Eq. (3.1) using a corrected stagnation pressure, p_0, at the throat.

The specific momentum is defined in Eq. (3.5) and presented in Table 3.2. The specific momentum normalizes a nozzle's momentum rate with the fuel flow rate, and has units of m/s. The specific momentum accounts for differences in the fuel mass flow rates of the various nozzles.

$$\bar{v} = \frac{\dot{p}_x}{\dot{m}_f} \tag{3.5}$$

Table 3.2 Valve performance comparison

		$\dot{m}_f$ (kg/s)	$\dot{p}_x$ (N)	$\bar{v}$ (m/s)
Low pressure injection (4bar)	Conventional poppet	0.113	42.7	378
	Simple converging-diverging nozzle	0.117	73.6	629
	Push-open poppet with nozzle	0.0928	53.6	577
	Pull-open poppet with nozzle	0.116	72.8	627
High pressure injection (35bar)	Conventional poppet	0.132	99.5	754
	Simple converging-diverging nozzle	0.129	116	899
	Push-open poppet with nozzle	0.108	93.8	869
	Pull-open poppet with nozzle	0.126	113	899

In terms of $\bar{v}$, 66% improvement for low pressure injection and 19% improvement for high pressure injection are possible by introducing a simple nozzle to the poppet valves. It is also worthy to note that a pull-open poppet operated at 4 bar low pressure injection pressure can give 83% of the specific momentum carried by

the jet issuing from the conventional 35 bar high pressure injection poppet valve. Using 35bar pipeline gas as an injection source is one of important and proved technology currently used for improving the engine performance. Result implies that introducing an efficient design to the conventional low pressure injection system can be an alternative supposed to bring comparable improvement with lower reform costs. At Fig. 3.6, In spite of the difference in fuel mass flow rate, the velocity profiles and the momentum flux profiles are compared for these two valves.

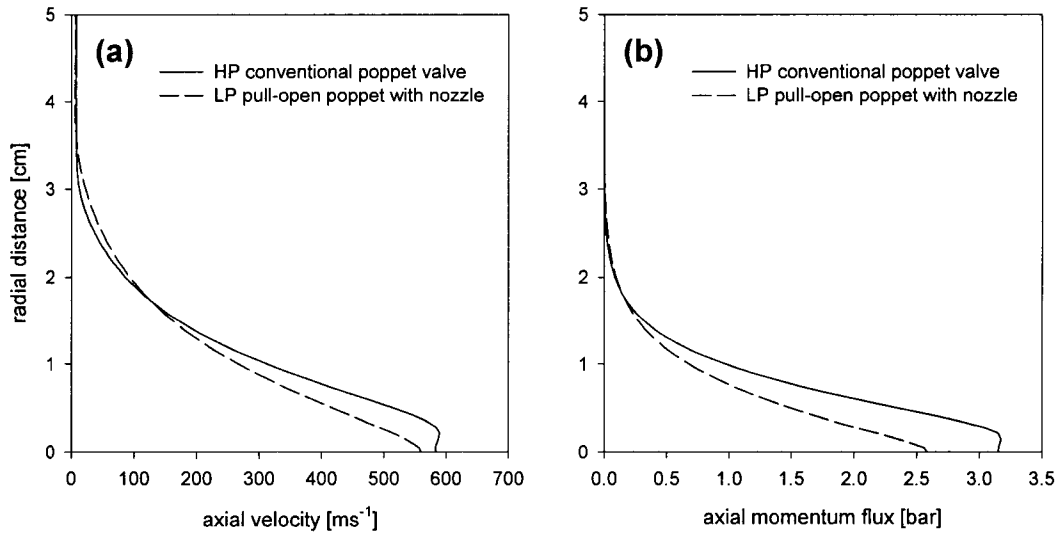

Fig. 3.6 Comparisons of axial velocity profiles (Fig. 3.6(a)) and of axial momentum flux profiles (Fig. 3.6(b)) between conventional high pressure injection poppet valve and improved low pressure injection poppet modification at 18 cm downstream from nozzle exit at 11 ms after start of injection.

3.4 Injection Efficiency of Valve

Radial distributions of stagnation pressure at nozzle throats for the nozzle equipped poppet valves are shown in Fig. 3.7. Results show that there is considerable amount of stagnation pressure loss upstream of nozzle throat in the push-open configurations for the both injection pressures, while only negligible loss occurs in

pull-open configurations of injection system. Since the flow upstream of the choking point, the nozzle throat, is subsonic, this loss that occurs inside of the poppet valve can be classified as a subsonic loss of injection pressure and called a valve loss. A representative value of the stagnation pressure at the throat can be determined from the fact that the throat stagnation pressure is proportional to the mass flow rate for the same nozzle throat area.

$$p_o \propto \dot{m}_f \qquad (3.6)$$

Histograms shown in Fig. 3.8 compare the throat stagnation pressures of the nozzle injection cases with the nominal injection pressure for both injection pressures. Fig. 3.8 indicates that about 20% of injection stagnation pressure for low pressure valve and about 16% for high pressure valve is lost during the jet passing the subsonic flow path in push-open configuration.

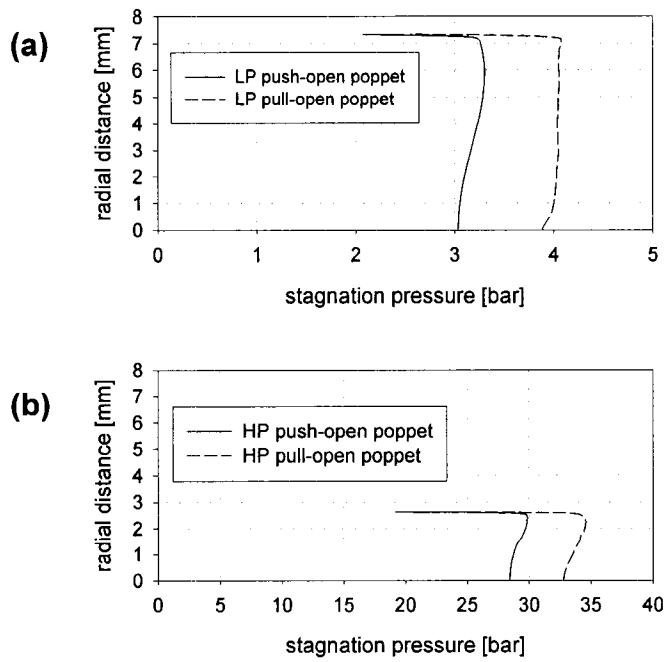

Fig. 3.7 Radial profile of stagnation pressure in modified valves at the nozzle throat for 4bar low pressure injection (Fig. 3.7(a)), and for 35 bar high pressure injection (Fig. 3.7(b)).

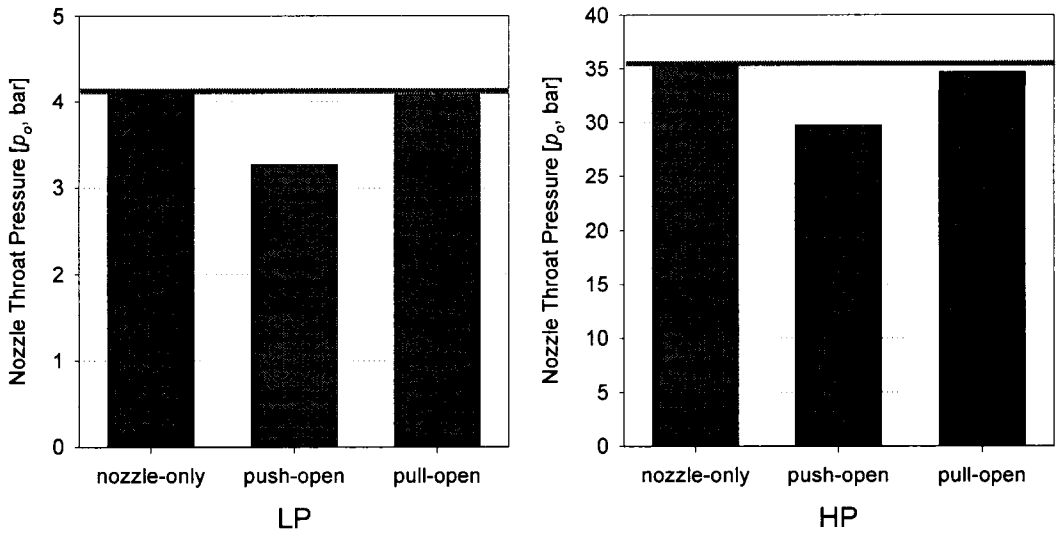

Fig. 3.8 Comparisons of throat stagnation pressures with nominal injection pressure for the low pressure nozzle injection cases (Fig. 3.8(a)) and for the high pressure nozzle injection cases (Fig. 3.8(b)).

Looking now at the flow downstream of the nozzle exit, Fig. 3.9 shows the Mach number profile along the jet axis in the low pressure injection test valve cases (Fig. 3.9(a)) and in the high pressure injection test valve cases (Fig. 3.9(b)). The axial distance was measured from the nozzle exit plane in each case. The low pressure conventional poppet jet has a completely subsonic downstream flow field due to its stagnation pressure loss in the poppet valve. The axis Mach numbers for the rest of the fuel jets are supersonic, and they oscillate immediately downstream of the nozzle.

These jet oscillations are due to the fact that none of the nozzle designs resulted in perfect expansion at the exit. The exit flow of the conically-shaped diverging nozzles used is not a parallel flow. The supersonic exit flow has a radially outward component of velocity determined by the nozzle cone angle as well as an axial component. Therefore, the jet issuing from a conical nozzle continues to expand

and to be over-expanded relative to the cylinder pressure. A larger nozzle cone angle causes a stronger expansion followed by the stronger compression waves or the shocks. Hence using a smaller cone angle for a conical nozzle reduces the stagnation pressure losses downstream despite an increase in the nozzle length.

Downstream of the oscillations, the axis Mach numbers of conventional poppet valve flow increase slightly before they start to decrease. This can be explained with the initial jet profile. As discussed in Kim et al. [3.1], the jet emanating from these types of valves is an initial jet profile with an annular radial profile. The maximum speed for this type of jet occurs well off the axis. The small and gradual increase of Mach number for the real valves can thus be traced to momentum transfer to the axis from higher velocity regions off the axis.

The centerline axis Mach numbers of the fuel jets issuing from the poppet valves with a nozzle reached a constant value around 5~11cm downstream, and remained constant until the jet core decay caused by the radially outward momentum diffusion reached jet center.

The effective injection pressure, which is defined as the supply stagnation pressure required to produce the same centerline Mach number for isentropic flow conditions can be determined using the one dimensional isentropic flow relation Eq. (3.7).

$$\frac{p_{o,eff}}{p_e} = \left(1 + \frac{\gamma - 1}{2} M_{e,eff}{}^2\right)^{\frac{\gamma}{\gamma - 1}} \qquad (3.7)$$

where $p_{o,eff}$ is effective stagnation pressure for injection and $M_{e,eff}$ is downstream core Mach number with back pressure p_e. Fig. 3.10 presents effective injection

pressures of the poppet valve with nozzle compared with the nominal injection pressure for each injection pressure. The difference between nominal injection pressure and effective injection pressure in each valve can be interpreted as the overall loss of stagnation pressure throughout the injection process. Since the subsonic losses of the valves have been determined (see Fig. 3.8), the quantification of the supersonic loss occurring downstream of the nozzle throat can be carried out by subtracting the subsonic loss from the overall stagnation loss. In this paper, this supersonic loss will be called a nozzle loss, because it mainly comes from non-isentropic supersonic flow structures such as oscillations and shocks.

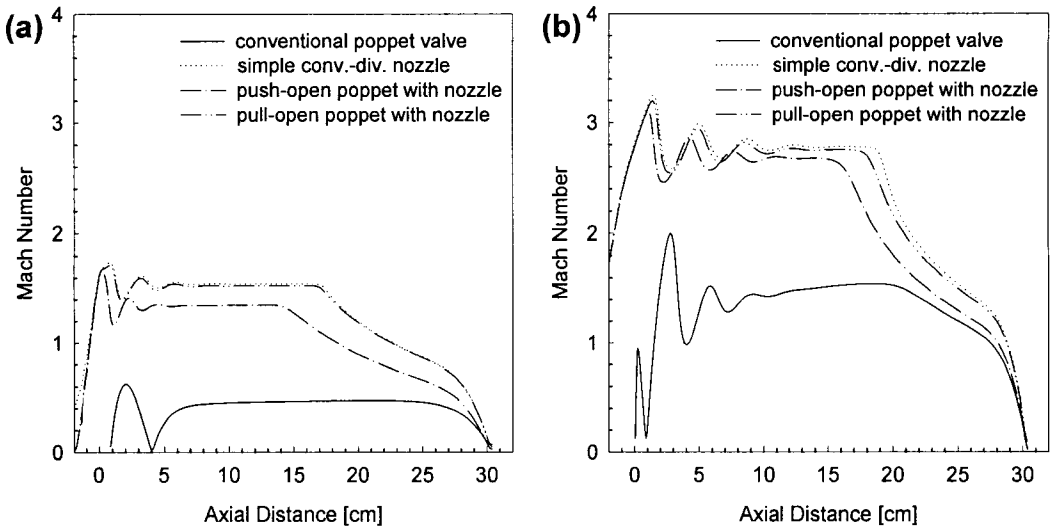

Fig. 3.9 Comparison of axis Mach number profiles for the tested valves in 4bar low injection pressure (Fig. 3.9(a)) and in 35bar high injection pressure(Fig. 3.9(b)).

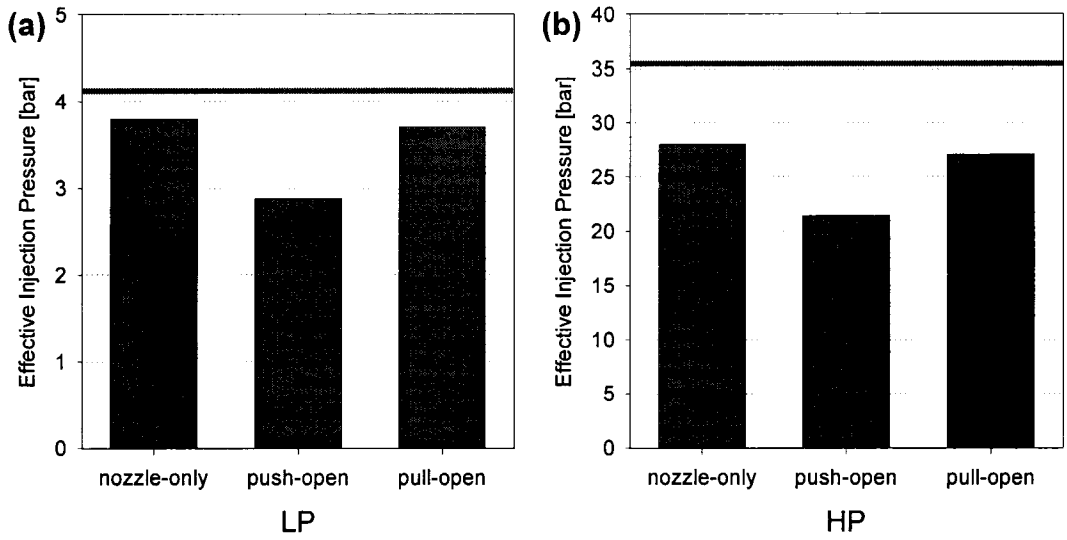

Fig. 3.10 Comparisons of the effective injection pressures with nominal injection pressure for the low pressure nozzle injection cases (Fig. 3.10(a)) and for the high pressure nozzle injection cases (Fig. 3.10(b)).

The classification of total stagnation pressure losses into a valve loss (a subsonic loss) and a nozzle loss (a supersonic loss) is useful in in devising improved injection valve design procedures. Since the throat stagnation pressure is a crucial operational parameter of the poppet valve with a nozzle, evaluation of the valve loss upstream of the throat must precede the design of the nozzle shape and its dimensions. The relative magnitude of each type of loss is also of interest to decide which one of them should be focused on for injection improvement under a given fuel supply conditions.

A pressure based injection efficiency, e_p, is defined in Eq. (3.8) as a parameter to compare the performance of poppet-nozzle fuel injection systems.

$$e_p = \frac{p_{o,eff}}{p_{o,nom}} \tag{3.8}$$

where $p_{o,nom}$ is the nominal injection pressure. Comparison of the relative losses for the poppet valves with a nozzle for both pressure conditions is presented in Fig. 3.11. The push-open valve with a nozzle for low pressure injection has an injection efficiency of 69.9%, and the pull-open design operated at a low injection pressure has a 90.0% efficiency. For the high injection pressure cases, the push-open and the pull-open configurations have 60.3% and 76.3% injection efficiency respectively. Fig. 3.11 also shows that the pull-open configurations have an advantage in reducing the subsonic valve loss relative to the push-open configurations in both injection pressure cases. The supersonic losses are almost the same for the same nozzles.

Direct evaluation of the injection efficiency for the conventional poppet valves is not straightforward, since the simple one-dimensional flow relations used for the effective pressure are not strictly applicable to the annular flow of conventional poppet jets. For the shrouded high pressure case, Kim et al. [3.2]

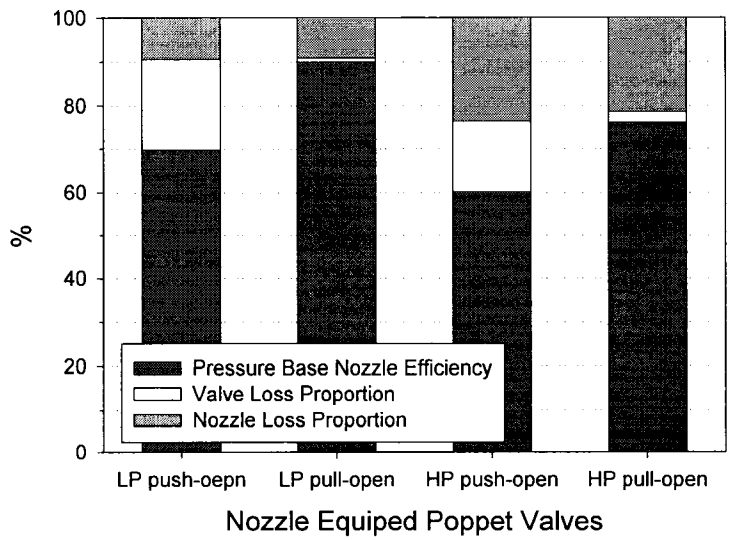

Fig. 3.11 Comparison of relative amount of the classified stagnation pressure losses and the effective injection pressure for the tested valves with nozzle.

suggested a procedure using an equivalent virtual valve concept to obtain a simple converging-diverging nozzle which would produce the same centerline Mach number as the conventional poppet operated at 35 bar high pressure. The valve injection efficiency of the high pressure conventional poppet valve calculated from this equivalent virtual valve method is 12.5%.

3.5 Comparison of Mixing

Moving piston simulations for the conventional poppet valves and for the reference simple converging-diverging nozzles were carried out to compare the mixing characteristics of the low and high pressure flows for an actual combustion chamber geometry. The flammable mixture fraction throughout the compression

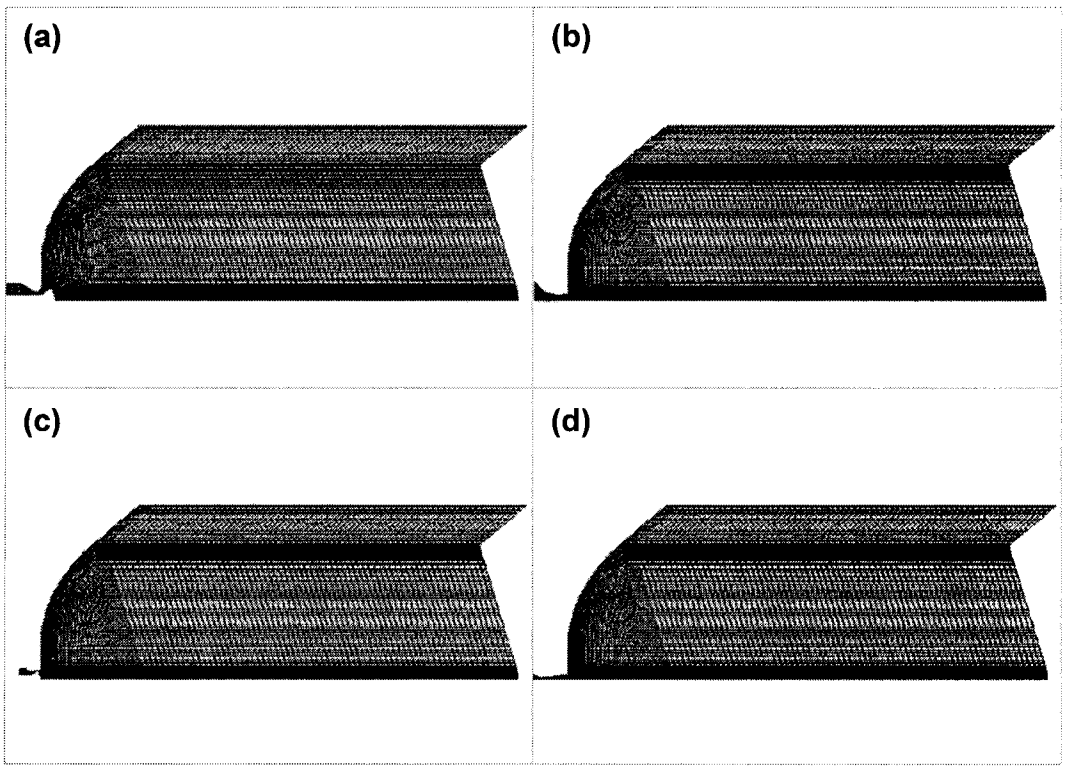

Fig. 3.12 Grid systems used for in-cylinder mixing simulations with moving piston top for conventional poppet valve low pressure injection case (Fig. 3.12 (a)), for converging-diverging nozzle low pressure injection case (Fig. 3.12(b)), for conventional poppet valve high pressure injection case (Fig. 3.12 (c)) and for converging-diverging nozzle high pressure injection case (Fig. 3.12 (d)).

stroke was computed as a measure of the effectiveness of the poppet valves and simple nozzle injectors.

Fig. 3.12 shows the grid systems designed to investigate the interaction between the fuel jets and the moving piston top in the cylinder. In this set of computations the piston moves from bottom dead center (BDC) to top dead center (TDC). Injection started at 120 degrees before top dead center in low pressure injection cases and at 115 degrees before top dead center in high pressure injection cases. The injection timings are the values used in actual engine operations. Initially the cylinders were filled with air at 1bar. The cylinder gas was assumed to be quiescent, with no scavenging air motion. The amount of fuel injected was chosen to produce an overall equivalence ratio of 0.61.

The flammable mixture fraction is defined as the ratio of the burnable mass of mixture to the total mass in the cylinder at any instant The mixture fractions are computed by integrating over all of the computational cells in the cylinder volume with Eq. (3.9).

$$f_m = \frac{burnable\,mass\,of\,mixture}{total\,mass\,of\,mixture} \qquad (3.9)$$

A lean mixture in a cell is defined here as one with an equivalence ratio less than 0.5, a flammable mixture has an equivalence ratio between 0.5 and 2.0, and a rich mixture has an equivalence ratio greater than 2.0. These definitions of lean, rich and flammable mixtures are based on laminar flame propagation limits at atmospheric pressure and nominal atmospheric temperature. Since the lean limit is generally observed not to be strongly affected by temperature and pressure, and since this is the

limit of consequence in lean burning engines, predictions based on these limits should still be useful.

Equivalence ratio contours during and after injection are shown in Fig. 3.13 The contours for each valve are presented from 81 degrees before top dead center to TDC in increments of 27 crank angle degrees. In the absence of scavenging flows, mixing is dominated by jet impingement on the piston and by fuel flow redirection along the surface of piston top and cylinder wall.

The results indicate that high pressure conventional poppet valve injection has better mixing than the low pressure poppet injections in terms of the spatial distribution of fuel. It is interesting to note that that the low pressure nozzle injection and the high pressure conventional poppet injection produced almost the same size and strength of induced vortices.

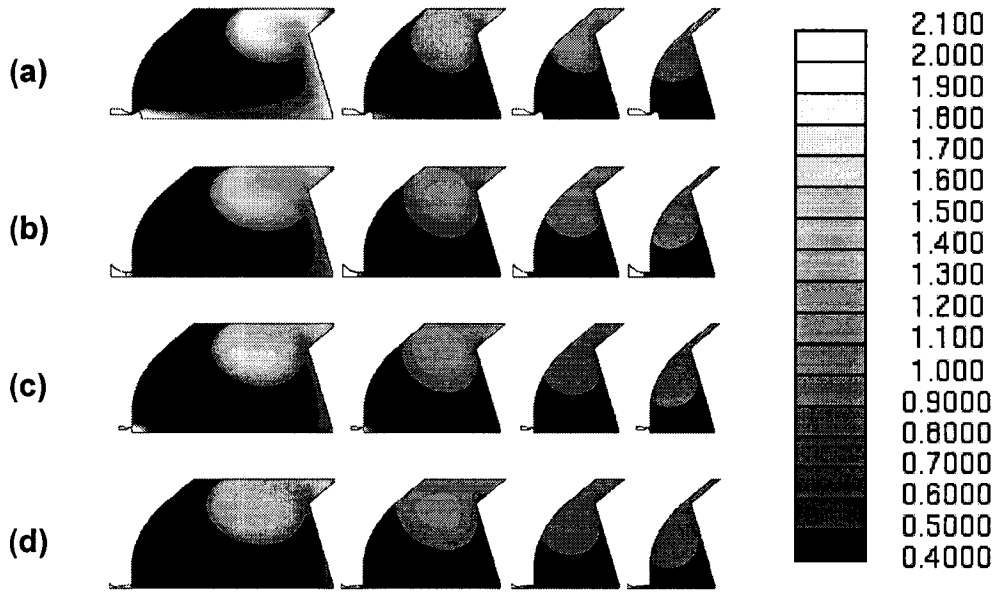

Fig. 3.13 Equivalence ratio contour sequences from 81 degrees of crank angle before top dead center to TDC in every 27 degrees of crank angle for low pressure conventional poppet valve injection (Fig. 3.13(a)), for low pressure nozzle injection (Fig. 3.13(b)), for high pressure conventional poppet valve injection (Fig. 3.13(c)) and for high pressure nozzle injection (Fig. 3.13(d)).

Fig. 3.14 shows how the flammable mixture fraction changes with crank angle during compression. These curves are a function of the start of injection, which is different for the low and high pressure cases, as well as the amount of fuel injected. The curves have an S-shaped profile. The greatest mixing is with the high pressure nozzle, and the least mixing is with the low pressure conventional poppet.

The higher slope sections of the curves correspond to the period of jet impingement on the piston, which indicates that jet impingement on the piston top enhances mixing. With the exception of the low pressure poppet, the increased slope of the high flammable mixture fraction appears about 5 degrees crank angle after start of injection and it is kept for about 20 degrees.

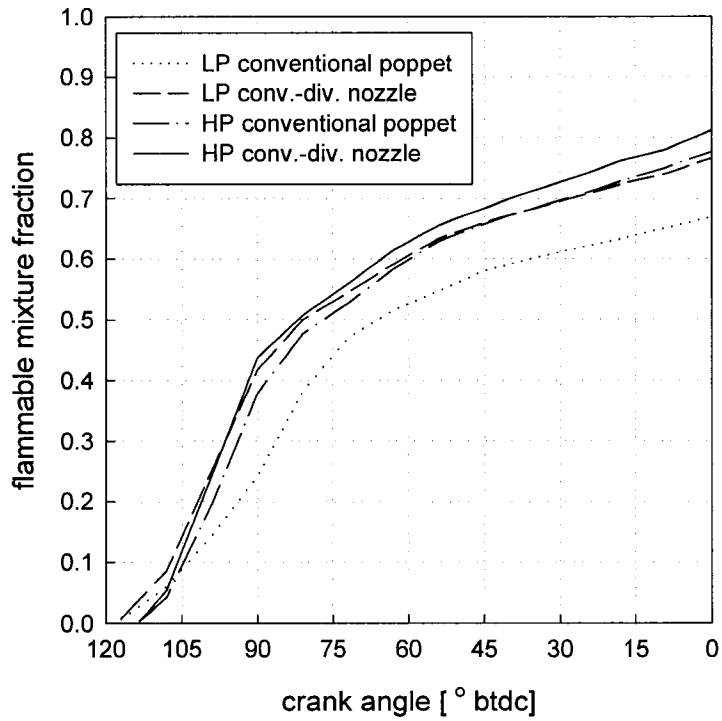

Fig. 3.14 Flammable mixture fraction changes with crank angle [degrees in btdc].

At both low and high injection pressure, the nozzle injection cases show better mixing at top dead center than the conventional poppet injection cases. This shows that introducing a nozzle to the poppet valves can effectively improve fuel-air mixing. As seen in Fig. 3.13 and in Fig. 3.14, the nozzle addition to the low pressure injection valve makes the mixing extent increase to that of the conventional high pressure injection through the poppet. Because raising injection pressure is one of most effective way in use to improve engine performance, removing the intrinsic defects of the poppet valve by adding a nozzle can be an alternative, as it giving compatible results to high pressure injection with less additional cost.

CHAPTER 4: Supersonic Injection Virtual Valve Design

Chapter Abstract

In many research areas, the role of overall three dimensional computation which can deal with the complex supersonic jet has become critical. However, in spite of its increasing necessity, it is costly to capture the details of supersonic structures in intricate three dimensional geometries. In large-bore stationary natural gas fueled engine research, one of the promising mixing enhancement technologies for natural gas engines currently used is high pressure fuel injection. Three dimensional computational simulations that can examine the entire injection and mixing process in high pressure injection engines and determine the impact of injector design on engine performance are consequently of considerable interest. However, the cost of three dimensional engine simulations including a moving piston and the kinetics of combustion and pollutants production quickly becomes considerable in terms of simulation time requirements. The limiting factor is the modeling of the small length scales of the poppet valve flow. Such length scales can be two orders of magnitude smaller than cylinder length scales.

The objective of this paper is to describe the development of a compatible simple geometry virtual valve which can be substituted in three-dimensional numerical models for the complex shrouded poppet valve injection system actually installed in the engine. Downstream flow characteristics of the jets from an actual valve and a virtual valve are compared. Various mixing parameters are evaluated in moving piston simulations that include the effect of the jet-piston interaction.

The results indicated that the suggested converging-diverging nozzle type virtual valve produces practically identical down stream fuel jet with the real valve injection jets.

4.1 Introduction

Three dimensional computational simulations that can examine the entire injection and mixing process in engines using high pressure injection and determine the impact of injector design on engine performance are consequently of considerable interest. However, the cost of three dimensional engine simulations including a moving piston and the kinetics of combustion and pollutants production quickly becomes considerable in terms of simulation time requirements. This cost is particularly high if the computational model has to capture the details of the complex supersonic flow structures in and near the intricate geometry of the injection valve. However, for an overall simulation designed to examine engine features such as the extent of fuel-air mixing, combustion, power production and pollutant generation, the details of these supersonic flow structures may not be critical. Indeed, it is probable that only the downstream jet characteristics are of crucial importance in these macroscopic engine performance studies.

The objective of this chapter is to describe the development of a compatible virtual valve which can be substituted in three dimensional numerical models for the complex shrouded poppet valve injection system actually installed in the engine to be simulated. Downstream flow characteristics of the jets passing through an actual valve and a virtual valve were compared. In addition, parameters assessing the extent

and effectiveness of mixing were evaluated in moving piston simulations that considered the effect of the jet-piston interaction.

Kim et al. [4.1] examined the injection of natural gas from the two typical types of poppet valves, an unshrouded low pressure (4bar) injection valve and a shrouded high pressure (35bar) injection valve. The results showed that large stagnation pressure losses occurred as the fuel passes through the poppet valve in both cases. In the low pressure injection case, the losses were sufficient to cause the downstream fuel jet to be completely subsonic. In contrast, the supply pressure was sufficiently high in the high pressure injection case that, in spite of large stagnation pressure losses, the jet was still supersonic downstream.

Many researchers in overall engine performance have tried to use a virtual nozzle as an alternative to modeling the exact geometry of the gas injector. Numerical models of engine performance incorporating subsonic natural gas injection from a simple orifice into an engine cylinder are presented by Gaillard [4.2], Han et al. [4.3], and Gundappa et al. [4.4]. Ouellette and Hill [4.5] and Mather and Reitz [4.6] developed the concept of a virtual nozzle sized proportional to the diameter of the Mach disk, which appears in high pressure jets from simple orifices, in order to model the subsonic flow downstream of the jet. However, experimental measurements of Olsen et al. [4.7] indicate that a significant portion of the injected fuel jet penetration distance is in the supersonic flow regime. Studies of sonic and supersonic gas injection with a poppet valve are much more limited. Of particular note is the pioneering work of Boyer et al. [4.8] who used schlieren photography to study the injection and scavenging processes in a Cooper GMV engine.

There are a number of methods used to quantify the mixing performance of a given injector. In this chapter, two parameters, mixture mass fraction and fuel mass fraction, are used. The mass fractions are divided into lean, flammable and rich categories. Papageorgakis and Assanis [4.9] used the mixture mass fraction as a basis of comparison, while Abraham and Magi [4.10] used the fuel mass fraction. The non-flammable (rich or lean) mixture mass fraction is related to the emissions performance, as it indicates the relative volume of the combustion chamber that may be susceptible to pollutant formation resulting from incomplete combustion. The flammable fuel mass fraction is related to the combustion efficiency, as it indicates the relative mass of fuel that is combustible.

The computational domain was discretized by using a variable size grid axisymmetric mesh in the computations. Grid adaptation was used to refine the mesh and locate the rapidly varying expansion and compression structures. Grid sensitivity computations indicated that at least ten grid points across the nozzle orifice were required in order to reduce the sensitivity of computational predictions to grid size in the nozzle region to an acceptable level. Two CFD solvers were used, Fluent, and Star CD. Standard k-ε model and RNG k-ε model were used for modeling turbulence. The computations were carried out on a SUN Ultra Sparc workstation.

4.2 Virtual Valve Design

A converging-diverging nozzle having a conical diverging section was adopted as the simplified virtual injection valve in this study because of its geometrical simplicity. An actual poppet valve in use for 35 bar high pressure fuel injection is presented in Fig. 4.1(a) and a converging-diverging nozzle type virtual

valve in Fig. 4.1(b). Several combinations of throat area and supply pressure for this virtual valve were tested. In each case these parameters were determined by matching the downstream jet characteristics such as Mach number, momentum flow rate and the fuel mass injection rate with the values for the actual poppet valve.

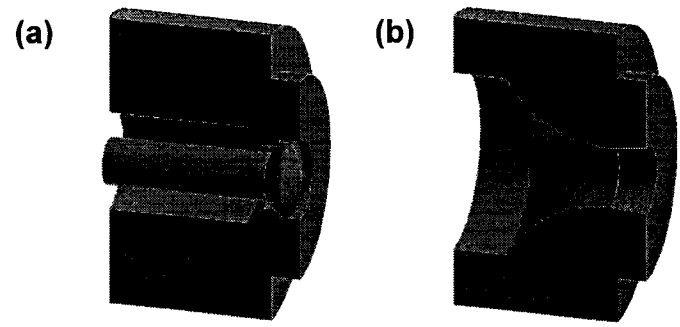

Fig. 4.1 Schematics of an actual valve currently in use for high pressure natural gas injection on a large-bore engine (Fig. 4.1(a)), and schematics of a simple converging-diverging type virtual valve designed for 3-D computations (Fig. 4.1(b)).

Quasi-one-dimensional isentropic flow relations and ideal gas relations were used to determine the required injection pressure and the dimensions of the virtual nozzle. Fig. 4.2 is a schematic showing the nozzle parameters; tank (supply) pressure p_0, throat radius r^* and nozzle exit radius r_e.

The injection stagnation pressure can be determined from given downstream condition using Eq. (4.1) which assumes isentropic flow occurs through the virtual nozzle and a constant value for γ.

$$\frac{p_0}{p_e} = \left(1 + \frac{\gamma - 1}{2} M_e^{\,2}\right)^{\frac{\gamma}{\gamma - 1}} \qquad (4.1)$$

The nozzle throat area A^* and its corresponding radius are determined by Eq. (4.2) for a given fuel mass flow rate $\dot{m}_f$.

$$A^* = \frac{\dot{m}_f}{p_0}\sqrt{\frac{RT_0}{\gamma}}\left(\frac{\gamma+1}{2}\right)^{\frac{\gamma+1}{2(\gamma-1)}} \qquad (4.2)$$

The nozzle exit area and its corresponding radius were calculated using the area-Mach number relation shown in Eq. (4.3).

$$\left(\frac{A_e}{A^*}\right)^2 = \frac{1}{M_e^{\,2}}\left[\frac{2}{\gamma+1}\left(1+\frac{\gamma-1}{2}M_e^{\,2}\right)\right]^{\frac{(\gamma+1)}{(\gamma-1)}} \qquad (4.3)$$

where A_e is nozzle exit area required to expand the fuel jet to the cylinder pressure at exit.

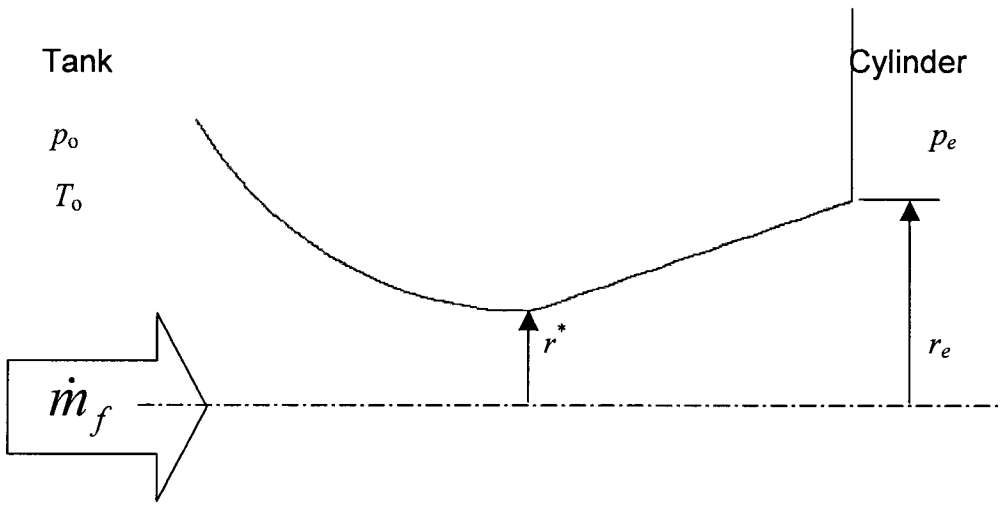

Fig. 4.2 Design parameters and conditions for virtual valves.

4.3 Comparison of Downstream Characteristics of Fuel Jet

Numerical simulations for the actual and a virtual valves were carried out to compare the injection performance of the valves. Methane was injected through each valve into an open cylinder which was kept at a constant pressure of one bar. The cylinder pressure varies slowly with a mean value close to one bar during injection in actual engines. The computational domain included the valve geometries and the piston top but not the cylinder wall. The near valve region and entire domain grids used for these numerical simulations are shown at Fig. 4.3. Since the poppet valve operates electronically with a top hat profile, the computational simulation assumed a fully open valve.

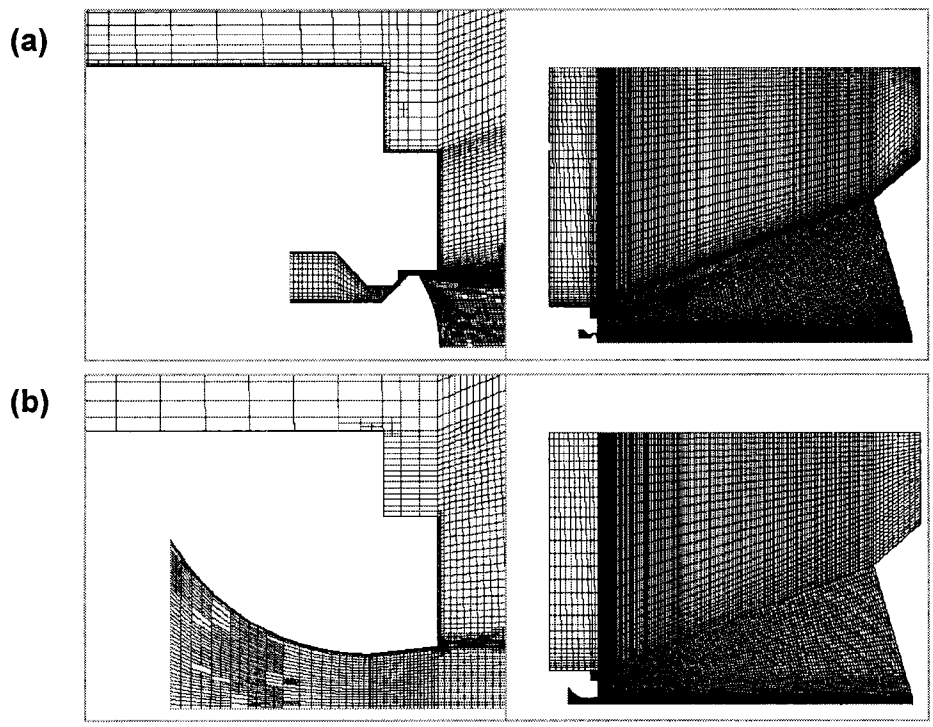

Fig. 4.3 Grids used in axisymmetric computations for actual valve injection (Fig. 4.3(a)) and for virtual valve injection (Fig. 4.3(b)).

Three different virtual valves used in the computations are presented here for comparison with the conventional actual valve. Design Mach numbers at nozzle exit, 1.53 for virtual-1 and 1.95 for virtual-2, were picked from the downstream Mach number profile of the jet issuing from actual poppet valve as shown in Fig. 4.4. Table 4.1 shows the design parameters and the resulting jet characteristics of these valves.

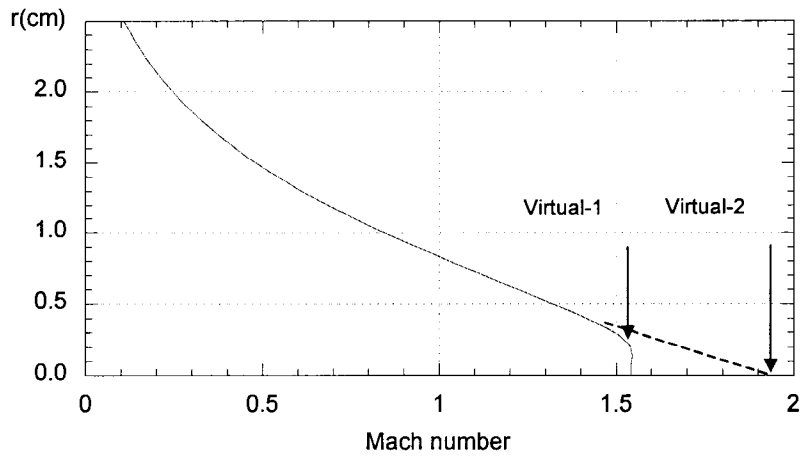

Fig. 4.4 Mach number profile of the jet issuing from conventional poppet valve at 18 cm downstream from shroud nozzle exit. Design exit Mach number of virtual-1 and virtual-2 are marked on the graph.

Table 4.1 Virtual valve design parameters and the characteristics of jets issuing from the valve/nozzle configurations

	Actual	Virtual-1	Virtual-2
$\dot{m}_f$ [kg/s]	0.131	0.130	0.129
$\dot{p}_x$ [N]	98.9	79.3	91.9
M_e		1.53	1.95
p_0 [bar]	35	3.73	7.16
r^* [mm]		8.14	5.88
r_e [mm]		8.95	7.65

Each axial momentum flow rate, $\dot{p}_x$, was calculated with Eq. (4.4) at 18cm downstream from the valve exit and at 11ms after start of injection.

$$\dot{p}_x = \int_0^\infty \rho v_x^2 2\pi r dr \qquad (4.4)$$

Because the injection jet flow approaches a local steady state within 2ms and the fuel injection duration of these engines is about 11ms, most of comparisons for validation of virtual valves were carried out at 11ms after start of injection. Fig. 4.5(a) shows the distribution of Mach number on the jet axis. The axial distance was measured from the nozzle exit plane in each case. The shrouded actual valve flow had a largely annular character. The resulting repeating structures of expansion and compression were eventually damped away downstream, with some losses in stagnation pressure accompanying this process. Downstream of the oscillations, the Mach number of the fuel jet that issued from conventional poppet valve increased slightly before it started to decrease. This can be explained with the initial jet profile. As discussed in Kim et.al. [4.1], the jet emanating from this type of poppet valve exhibits an initial jet profile with an annular radial profile. The maximum speed for this type of jet occurs well off the axis. The small and gradual increase of Mach number for the real valve can thus be traced to momentum transfer to the axis from higher velocity regions off the axis.

In spite of the peculiar initial structures of poppet flow, the main idea of the virtual valve design is to replicate the actual fuel jet after the structures have died down. In both the virtual valves, virtual-1 and virtual-2, the Mach number of the supersonic fuel jet oscillated just downstream of the nozzle exit. These oscillations were due to the fact that neither of the nozzle designs resulted in perfect expansion at

the exit plane. Both virtual nozzles were somewhat over-expanded due to the simple approximate method used in their design. The core Mach number of the fuel jets issuing from the virtual valves reached a constant value about 8cm downstream, and remained constant until the momentum of the jet's core started to diffuse outward in the radial direction; the virtual valve converging-diverging nozzles produce essentially one-dimensional flows at the exit. The jet was further slowed as it eventually entered the region influenced by the existence of the piston top located at 30cm. Comparing the axis Mach number profiles, virtual-1 showed better agreement with the actual valve in the initial jet region and virtual-2 followed the real profile more closely as the piston surface was approached.

Radial distributions of axial velocity and axial momentum flux at this location are compared in Fig. 4.5(b) and Fig. 4.5(c) respectively. At the axial location 18cm from the nozzle exit all the jets presented here had developed typical bell-shaped profiles and were still free from the effect of piston top. As can be seen from these figures, virtual -2 profiles for velocity and axial momentum flux were very similar to those of the real valve except near the axis. This dissimilarity of near axis profiles is relatively unimportant in designing a virtual nozzle, since the amount of mass flow is small near the axis. This is due to the fact that the cross-sectional flow area is proportional to the square of the radial distance from the axis.

The axial momentum flux, showed in Fig. 4.5(c), was integrated over the jet cross-section in order to get the numerical values of axial momentum flow rate presented in Table 4.1. The profiles of Fig. 4.5(b) and Fig. 4.5(c) imply that virtual nozzles can produce satisfactory approximations of the downstream fuel jet issuing

from a real poppet valve in spite of the quite different geometries and supply conditions and significant differences in upstream jet structures.

Because interaction of the fuel jet with the piston top is believed to play a significant role in fuel-air mixing, the jet penetration rate could be of importance. Penetration depth comparisons among the actual and the virtual valves are presented by showing the velocity magnitude contours at increasing times from the start of injection in Fig. 4.6. The actual valve and virtual-1 contours show good agreement while the jet issuing from the virtual-2 valve penetrates slightly faster than the others. The difference in penetration depths comes from the fact that the maximum velocity of virtual-2 is larger than those of the others, as seen at Fig. 4.5(b). It should be observed that since the penetration time to the piston top is of the order of 1ms, while the total injection period is about 11ms, small differences in penetration rate are unlikely to have any substantial impact on overall mixing behavior.

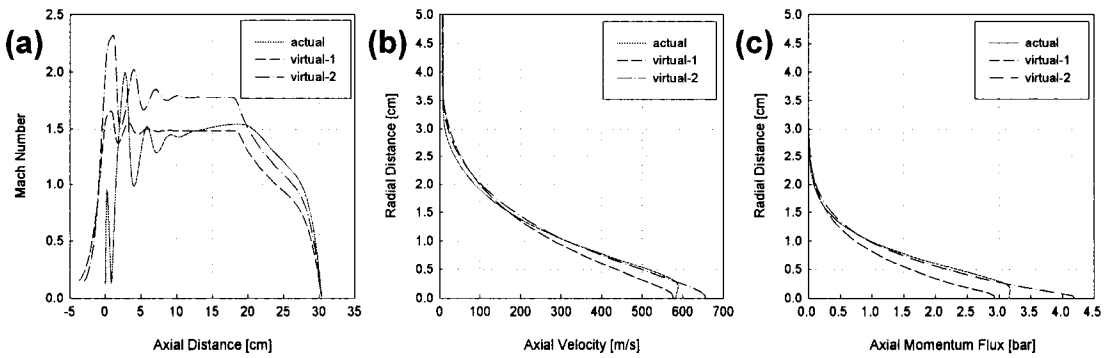

Fig. 4.5 Comparisons of centerline Mach number profiles among the tested valves (Fig. 4.5(a)), axial velocity [ms^{-1}] distribution at 18 cm downstream jets (Fig. 4.5(b)) and axial momentum flux [bar] at 18 cm downstream jets (Fig. 4.5(c)).

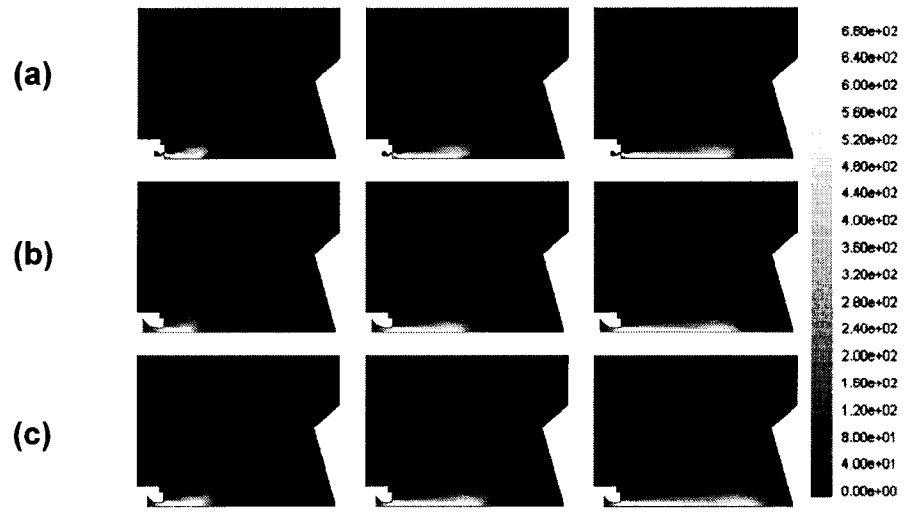

Fig. 4.6 Velocity magnitude contours [ms^{-1}] at 0.3 ms, 0.6 ms and 0.9 ms for comparison of penetration rates of actual valve (Fig. 4.6(a)), virtual-1 (Fig. 4.6(b)) and virtual-2 (Fig. 4.6(c)).

4.4 Comparison of Mixing Statistics

Moving piston simulations for the conventional shrouded poppet valve and for the virtual valves were carried out in order to compare the overall mixing characteristics. Fig. 4.7 shows the grid systems designed to investigate the interaction between the fuel jets and the moving piston top in the cylinder. The computations

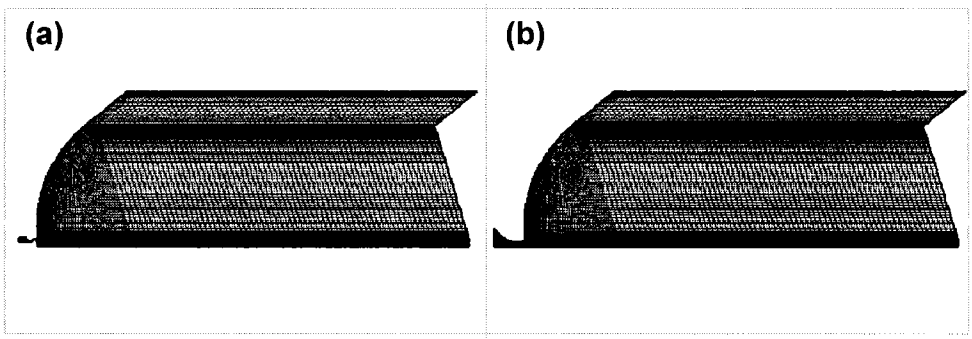

Fig. 4.7 Grid systems used for in-cylinder mixing simulations with moving piston top with actual valve(Fig. 4.7(a)) and with virtual valve(Fig. 4.7(b)).

were axisymmetric and the effects of scavenging were not included. In this set of computations the piston moves from bottom dead center (BDC) to top dead center (TDC). Injection started at 115 degrees before top dead center and the injection duration was 20 degrees of crank angle. The effectiveness of fuel-air mixing was examined by calculating flammable fuel fractions and flammable mixture fractions during the injection.

The flammable mixture fraction is defined as the ratio of the burnable mass of mixture to the total mass in the cylinder at any instant. Similarly, the flammable fuel fraction is defined as the ratio of the mass of burnable fuel to the total fuel mass in the cylinder. Note that the flammable mixture fraction considers those fractions of the mass where only air is present, while the flammable fuel fraction does not. The mixture and fuel fractions are computed by integrating over all of the computational cells in the cylinder volume with Eq. (4.5) and Eq. (4.6).

$$f_m = \frac{burnable\ mass\ of\ mixture}{total\ mass\ of\ mixture} \tag{4.5}$$

$$f_f = \frac{mass\ of\ fuel\ included\ in\ burnable\ mixture}{total\ mass\ of\ fuel} \tag{4.6}$$

A lean mixture in a cell is defined as one with an equivalence ratio less than 0.5, a flammable mixture has an equivalence ratio between 0.5 and 2.0, and a rich mixture has an equivalence ratio greater than 2.0. These definitions of lean, rich and flammable mixtures are based on laminar flame propagation limits at atmospheric pressure and nominal atmospheric temperature. Since the lean limit is generally observed not to be strongly affected by temperature and pressure, and since this is the

limit of consequence in lean burning engines, predictions based on these limits should still be useful.

Equivalence ratio contours during and after injection are shown in Fig. 4.8. The contours for each valve are presented from 72 degree before top dead center to TDC in increments of 18 crank angle degrees. In the absence of scavenging flows, mixing appeared to be dominated by jet impingement on the piston and fuel flow redirection along the surface of piston top and cylinder wall. In an overall sense fuel-air mixing occurred in a similar way in the virtual and the real valve cases. In spite of the differences of the injection geometries and the supplied pressure, the size and the strength of the induced vortex in each valve system as well as the spatial distribution of fuel showed good agreement.

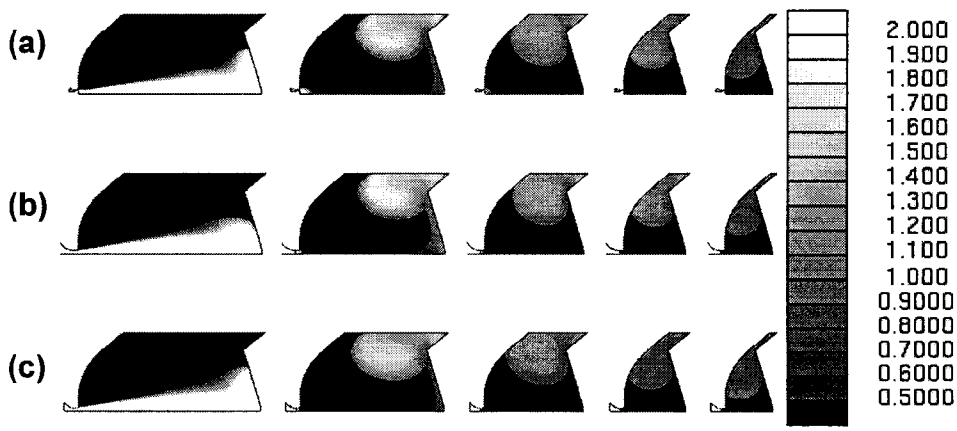

Fig. 4.8 Equivalence ratio contour sequences from 108 degrees of crank angle before top dead center to TDC in every 27 degrees of crank angle for actual valve injection (Fig. 4.8(a)), for virtual-1 (Fig. 4.8(b)) and for virtual-2 (Fig. 4.8(c)).

Fig. 4.9 shows how the flammable mixture fraction changes with time. The relative amount of flammable mixture can be interpreted as indicative of the extent of mixing. The total amount of fuel injected into the cylinder was the same and the overall equivalence ratio was fixed as 0.68 in each simulation. As can be seen in the figure, the two virtual valves already discussed produced flammable mixture fraction curves that bracketed the results for the real valve. In response to this prediction, one more virtual valve with design variables in between the other two was developed.

This valve, virtual-3, had a throat radius of 6.91 mm and a supplied injection pressure of 5.13 bar. These values result from applying the virtual nozzle design procedure described earlier when the exit Mach number was specified as 1.74, midway between the values for virtual-1 and virtual-2. The corresponding flammable mixture fraction prediction for virtual-3 can be seen to be very close to that of the real valve at all crank angles.

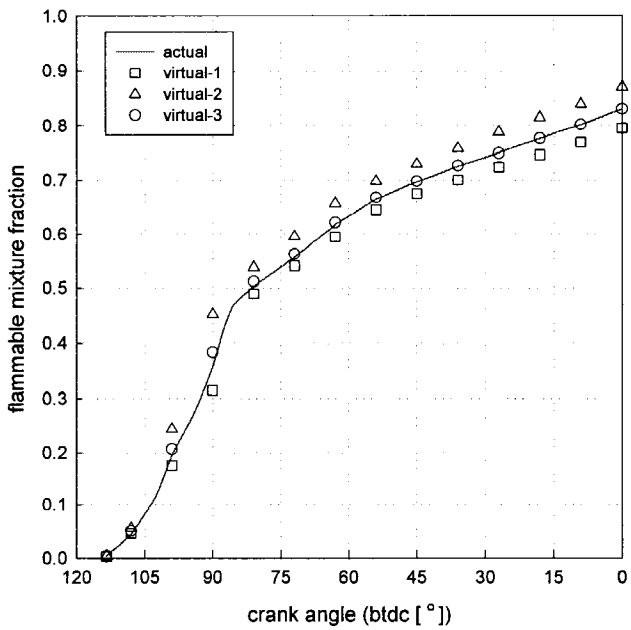

Fig. 4.9 Flammable mixture fraction changes with crank angle [degrees in btdc].

Mass averaged turbulent kinetic energy at the time of ignition, corresponding to 9 degrees before top dead center, was calculated using Eq. (4.7). Results for the four valves considered are compared in Fig. 4.10. The turbulent kinetic energy is of interest since minimization of the combustion duration in an engine requires a high turbulent intensity. Consistent with the flammable mass fraction predictions, the predictions of turbulent kinetic energy for virtual-3 simulate the actual valve very closely and lie between the predictions for virtual-1 and virtual-2.

$$\bar{k} = \frac{\int k\rho dV}{\int \rho dV} \qquad (4.7)$$

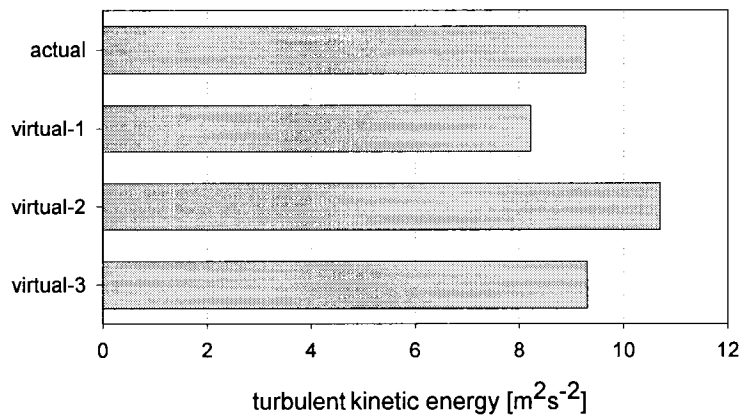

Fig. 4.10 Comparison of mass averaged turbulent kinetic energy at 9 crank angle degrees before top dead center for each tested valve.

Distributions of mixture and fuel mass with equivalence ratio were also computed. Results at 9 degrees before TDC for mixture mass and fuel mass are presented in Fig. 4.11(a) and Fig. 4.11(b), respectively. The distributions predicted for the real valve and virtual-3 are quite similar throughout the range of observed

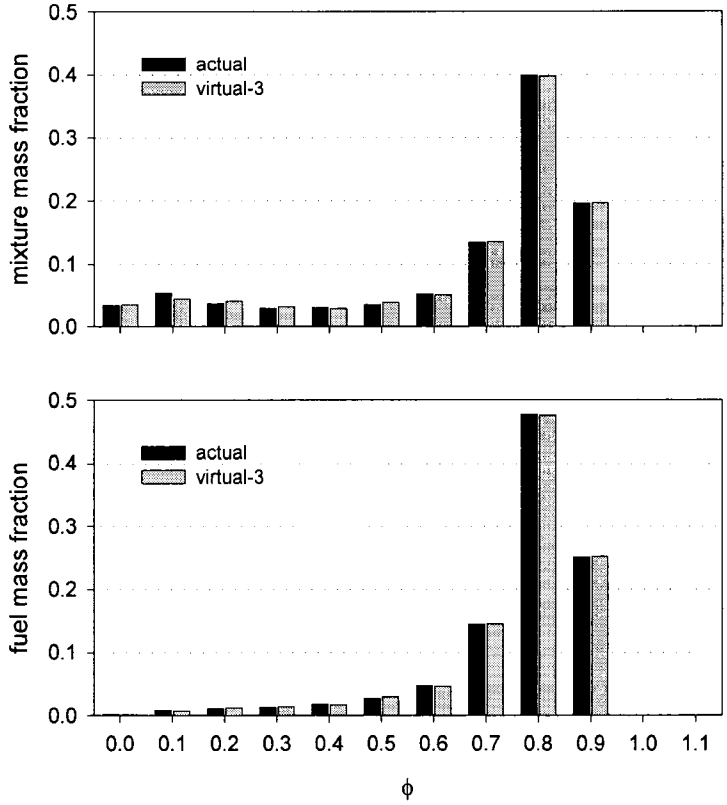

Fig. 4.11 Mass distribution with equivalence ratio for the mixture gas (Fig. 4.11(a)) and for the fuel gas (Fig. 4.11(b)).

equivalence ratios. The similarity of these distributions is important, for instance, in case of NOx production, where the local flame temperature is critical.

The comparisons of spatial distributions of interesting quantities at 9 degrees before top dead center are presented. Fig. 4.12 shows the equivalence ratio contours for the actual valve and the virtual-3 valve. Turbulence kinetic energy contours for these valves are shown at Fig. 4.13. The magnitudes and patterns of these distributions are matched to a good extent. The virtual-3 valve injected practically an identical downstream jet while requiring only 15% of the injection pressure. This is direct evidence of the very poor efficiency of standard poppet valve designs

compared with ideal expansion nozzles. The results seem to indicate that a virtual valve can be successful in simulating not only the average mixing characteristics of a real valve but also the details.

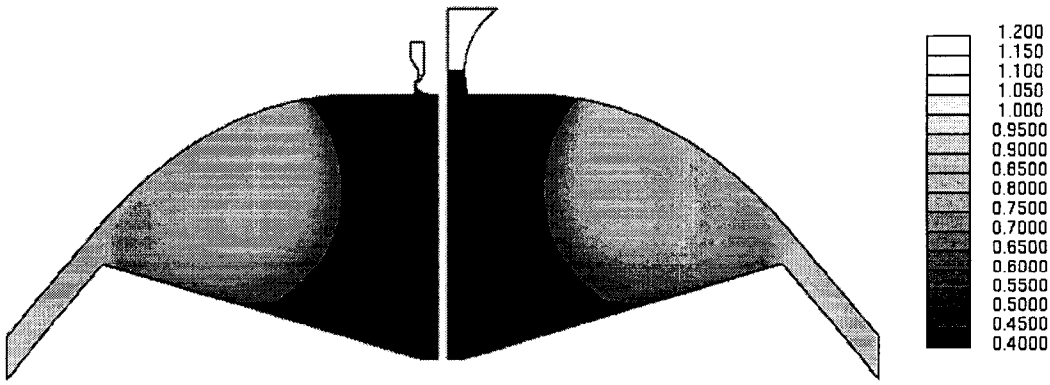

Fig. 4.12 Comparison of spatial distribution of fuel at 9 crank angle degrees before top dead center by showing the equivalence ratio contours for actual and for virtual-3 valve.

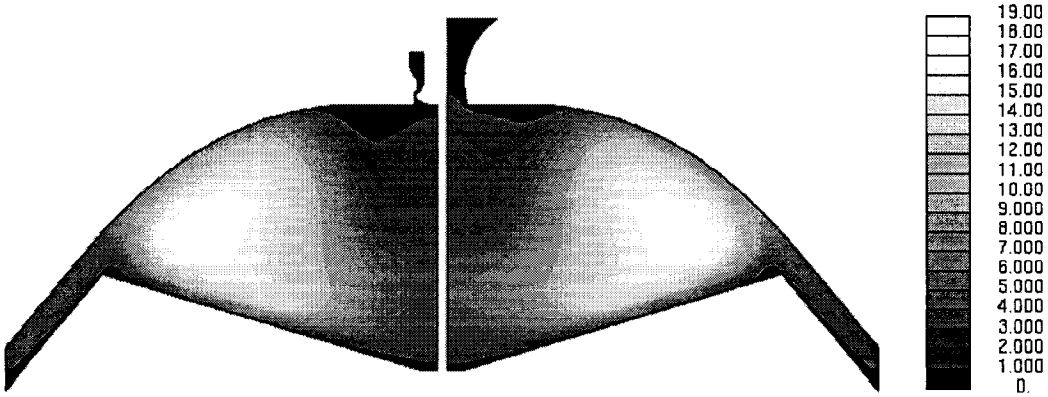

Fig. 4.13 Comparison of spatial distribution of turbulent kinetic energy (TKE) [m^2s^{-2}] at 9 crank angle degrees before top dead center by showing TKE contours for actual and for virtual-3 valve.

CHAPTER 5: Three Dimensional Overall Engine Simulations

Chapter Abstract

A moving grids three dimensional computational model of a Cooper GMV engine that includes ports scavenging, gas compression, fuel injection, fuel-air mixing, combustion, and pollutant generation was developed and validated through comparison with experimental results. The Cooper-GMV is one of the typical large bore natural gas engines which have been used in stationary applications such as gas compression and electric power generation. The first objective of the research is to develop an understanding of the fluid dynamics and combustion in conventional and retrofitted operation of the engine. The second objective, based on the first, is to make suggestions for new design and operating conditions for engine performance improvement.

These numerical computations of conventional operation of this engine indicate that the interaction between the scavenging flow and the injected fuel jet causes the jet to deflect enough to impact the piston top off center, producing non-symmetric mixing in the combustion chamber. The jet does not fill the cylinder volume in a symmetric fashion, but sweeps toward the intake ports, around the top of the cylinder volume toward the opposite side of the cylinder, and along the outer edges of the piston top. As a result, the combustion mixture is not fully mixed at the time of ignition. Most of the cylinder volume is filled with a flammable mixture with equivalence ratios ranging from 0.5 to 1.5 before the ignition occurs. There is a lean region in the core, richer regions around the edge of the cylinder, and a richest region

in the crevice around the edge of the cylinder. The combustion duration is about 30 degrees of crank angle. The flame propagation during combustion is non-uniform, with a greater flame speed in regions with a near stoichiometric equivalence ratio and the flow field favoring the direction of flame propagation.

Retrofitted operation of the engine with high pressure fuel injection, pre-combustion chamber ignition and laser spark ignition are all investigated computationally. The simulation results indicate that high pressure fuel injection enhances the cylinder mixing. The alternative ignition methods examined change the flame propagation pattern so that the duration of heat release is shortened.

5.1 Introduction

The topic of this chapter is the simulation of the two-stroke cycle performance of a large bore two-stroke natural gas fueled engine. As air emission regulations have been enacted, reducing exhaust emission levels from these pipeline engines has been increasingly important. Therefore developing a successful retrofit technology to improve engine performance and reduce pollutant generation became an issue. In order to contrive the effective retrofit technologies, understanding the fluid dynamics and combustion inside the cylinder in conventional operation should precede any design changes. Retrofitted operation of the engine with high pressure fuel injection, pre-combustion chamber ignition and laser spark ignition were investigated using CFD models.

The objectives of this chapter are to develop a computational model of the two-stroke GMV engine that includes port scavenging flow, compression, fuel injection, ignition, and the combustion stroke and to make suggestions for new

designs and operating conditions to improve engine performance. This engine has not been widely studied, and detailed information about the scavenging, fuel injection, and combustion processes are limited. This work is a continuation of the CFD study of the gas injection process in large bore engines by Kim et al. [5.1]. Some relevant previous work should be cited. Pioneering flow visualization studies of the scavenging flow in the Cooper engine were published by Boyer et al. in 1959 [5.2]. Numerical simulations of combustion using a combined time combustion model in a two stroke compression ignition engine with directly injected natural gas and pilot diesel fuel were performed by Ouellette, Mtui, and Hill [5.3]. Finally, CFD combustion and emissions modeling of a Cooper engine was reported by Gundappa et al. [5.4].

An instrumented four cylinder Cooper GMV engine at the CSU Engines and Energy Conversion Laboratory was used to provide cylinder pressure and heat release test data. The cylinder modeled in this chapter is a representative Cooper GMV engine cylinder with a 35.5 cm cylinder bore and stroke, compression ratio of 11, and rated speed of 300 rpm. For the single cylinder computation in this report, the intake ports are assumed to open at 121^{o} after TDC, and close at 120^{o} before TDC. The exhaust ports are assumed to open at 114^{o} after TDC, and close at close at 113^{o} before TDC. The spark ignition is initiated nominally at 10^{o} before TDC.

The scavenging gas is air, and the inlet manifold pressure is boosted above atmospheric pressure by a turbocharger or supercharger. The scavenging in this engine is classified as Schnurle or loop scavenging, in which the intake ports are angled upward to reduce short circuiting. The natural gas fuel is directly injected into

the cylinder, beginning at 120° before TDC, for a 20 degree duration. The electronically controlled valve has a top hat profile, in which the opening and closing times are much less than the fully open duration. The methane injection pressure is nominally 4 bar. The actual static pressure at the injector nozzle was not measured. The computations assumed 15 percent stagnation pressure loss between the gas supply and the nozzle. The amount of injected fuel mass per cycle in each cylinder is approximately 1g. Thus, the engine is fueled lean, with an overall equivalence ratio of about 0.61. Further information about the engine and associated test data is given in Olsen et al. [5.5].

5.2 Computational Modeling

The computational domain of the Cooper engine cylinder and ports assembly was discretized by using a variable size grid. Grid adaptation was used to refine the mesh and locate the rapidly varying expansion and compression structures in the region near the poppet valve injector. Two CFD solvers were used, Fluent, and Star CD. The turbulence model used was the standard k-ε model. About 120,000 grid points were used for the overall cylinder grid. The computations were carried out on a SUN Ultra Sparc workstation, and usually required about six days for a full two stroke simulation.

The computational grids at three different piston positions are presented in Fig. 5.1 for the bottom dead center piston position, at 90° before TDC, and at TDC. The Cooper cylinder is connected to eight intake and five exhaust ports, and the grid models one half of the cylinder with four intake and two and one half exhaust ports

and assumes a plane of symmetry. The four intake ports are shown as inclined slots connected to an intake manifold, and the exhaust ports are shown with the runners.

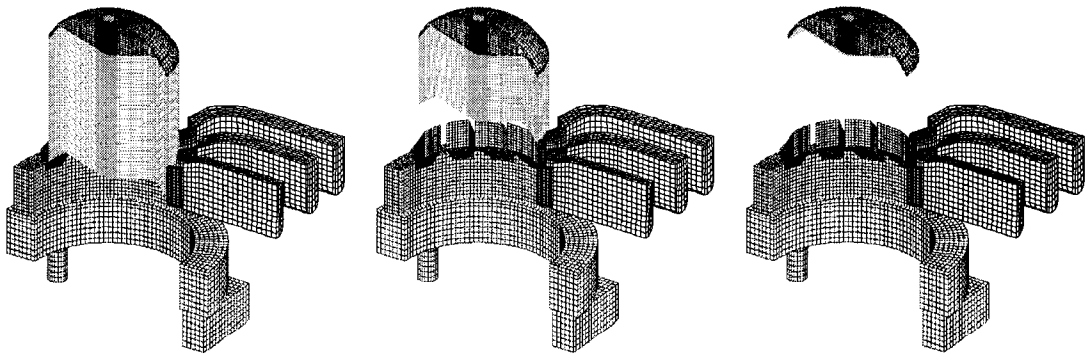

Fig. 5.1 Moving grid mesh used for three dimensional Cooper-GMV engine simulations

The computational time step profile was adjusted to maintain computational stability. The initial time step dt was chosen using the Courant number (Co) condition $Co < 0.5$, where $Co = u\ dt/dx$, u is the fluid velocity, and dx is the cell size. The smallest time step was generally 10^{-6} s. Smaller time steps were sometimes used during fuel injection, initiation of combustion, and at exhaust port opening to account for the increased changes in species concentration, velocity, pressure, and temperature. At each time step, values of species concentrations, velocity, pressure, temperature and turbulence quantities were computed at each computational cell.

The computations for the compression stroke were started at 108° after TDC (before exhaust port opening), with the piston moving downward toward bottom dead center. The intake manifold pressure was set at 107 kPa, and the exhaust manifold pressure was set at 100 kPa. The inlet gas temperature was 316 K. The conventional gas injection poppet valve is 23.9 mm in diameter, with a 6.35 mm maximum lift.

The top hat profile of the poppet valve was approximated in the numerical model by keeping the valve open at its maximum lift. The valve is shown in Fig. 5.2.

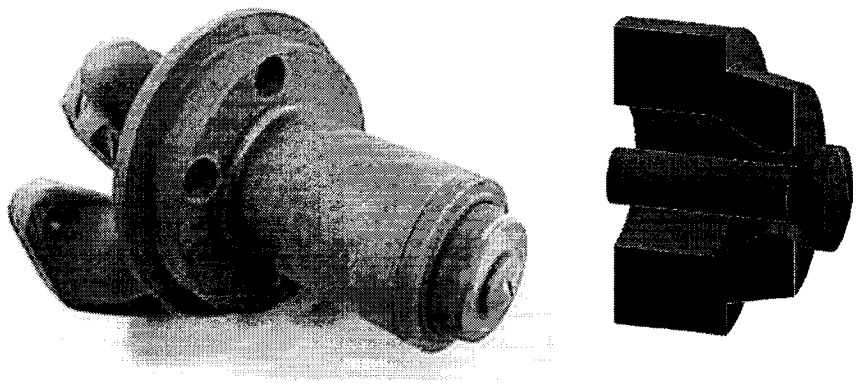

Fig. 5.2 Conventional low pressure injection poppet valve

5.3 CFD Validation with PLIF Experiments

Results from optical engine experiments using PLIF (Planar Laser Induced Fluorescence) were used to visualize the fuel injection and mixing inside the cylinder. The details of the PLIF imaging experiment are described further in Olsen et al. [5.5]. The CFD computations are compared with the PLIF experimental results in Fig. 5.3 and Fig. 5.4. For the PLIF images the bright areas indicate regions of high intensity fluorescence from the acetone seeded fuel and, thus, also represent high concentrations of injected gas. For the CFD images the bright areas represent high concentration of the injected gas.

Fig. 5.3 presents a comparison of CFD prediction and experiment for conventional transient poppet valve injection into a quiescent cylinder. In this simulation, the air in cylinder was initially at rest and piston motion was not incorporated. The left side of each frame is the PLIF image, and the computations

appear on the right side. The supply/cylinder pressure ratio is 4. The flow features contained in the CFD and the PLIF images are very similar. As the gas is injected into the cylinder, it flows over the poppet valve initially forming an S-shaped conical profile with a leading vortex, as shown in the second image. The conical profile collapses to the axis downstream of the poppet valve, and the body of the jet behind the leading vortex has a relatively constant diameter. The vortex increases in size as it penetrates into the cylinder, and mixes with the cylinder gas. This comparison implies that the CFD computation can predict the general qualitative features of the conventional poppet injection.

Fig. 5.3 Comparisons of conventional low pressure fuel injection for the validation of CFD computation with PLIF experiments

In contrast, the CFD simulation and the experimental results compared in Fig. 5.4 include the interaction between the injected fuel jet, piston motion and scavenging flow inside cylinder. In this case, in-cylinder flow fields had already been formed by the scavenging gas flow and the piston motion, by the time the fuel jet started to issue into the cylinder. The images presented in Fig. 5.4 are the section contours at the symmetry plane of the engine. In this symmetry plane, the intake ports are located at the left side of each image and the exhaust ports are at the right. The PLIF images are

on the right hand side, and the CFD results are on the left hand side of the pairs of images. The scavenging flow bends the fuel jet slightly toward the exhaust ports, so that the fuel jet hits the piston top slightly off center, producing non- symmetric mixing in the combustion chamber. The bulk of the fuel jet then moves toward the intake ports, as the piston moves upward. These images indicate that the CFD computations can model the general in-cylinder flow induced by scavenging and the actual injection and mixing processes.

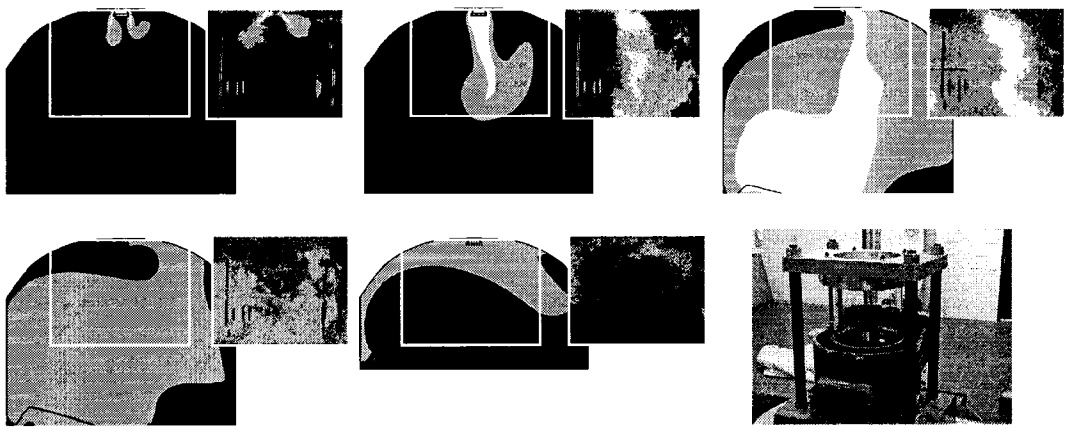

Fig. 5.4 Comparisons of fuel injection and mixing with scavenging flow and moving piston for the validation of CFD computation with PLIF experiments

5.4 Compression Stroke

The compression stroke model includes port scavenging, gas exchange, mixture compression, fuel injection and fuel-air mixing.

5.4.1 Scavenging Process

The scavenging results are shown in Fig. 5.5, plotted as a function of crank angle, starting just before exhaust port opening in the late stages of the expansion

stroke at 250.2 degrees before TDC. The shaded area represents the fresh intake air, and the non-shaded area is the residual gas or the burnt exhaust gas. As the exhaust ports open at 246 degrees before TDC, blowdown flow into the exhaust ports begins. Then, the intake ports open at 239 degrees before TDC, and, since the cylinder pressure is still greater than the intake manifold pressure, there is reverse flow from the cylinder into the intake ports. By about 210 degrees before TDC, positive flow

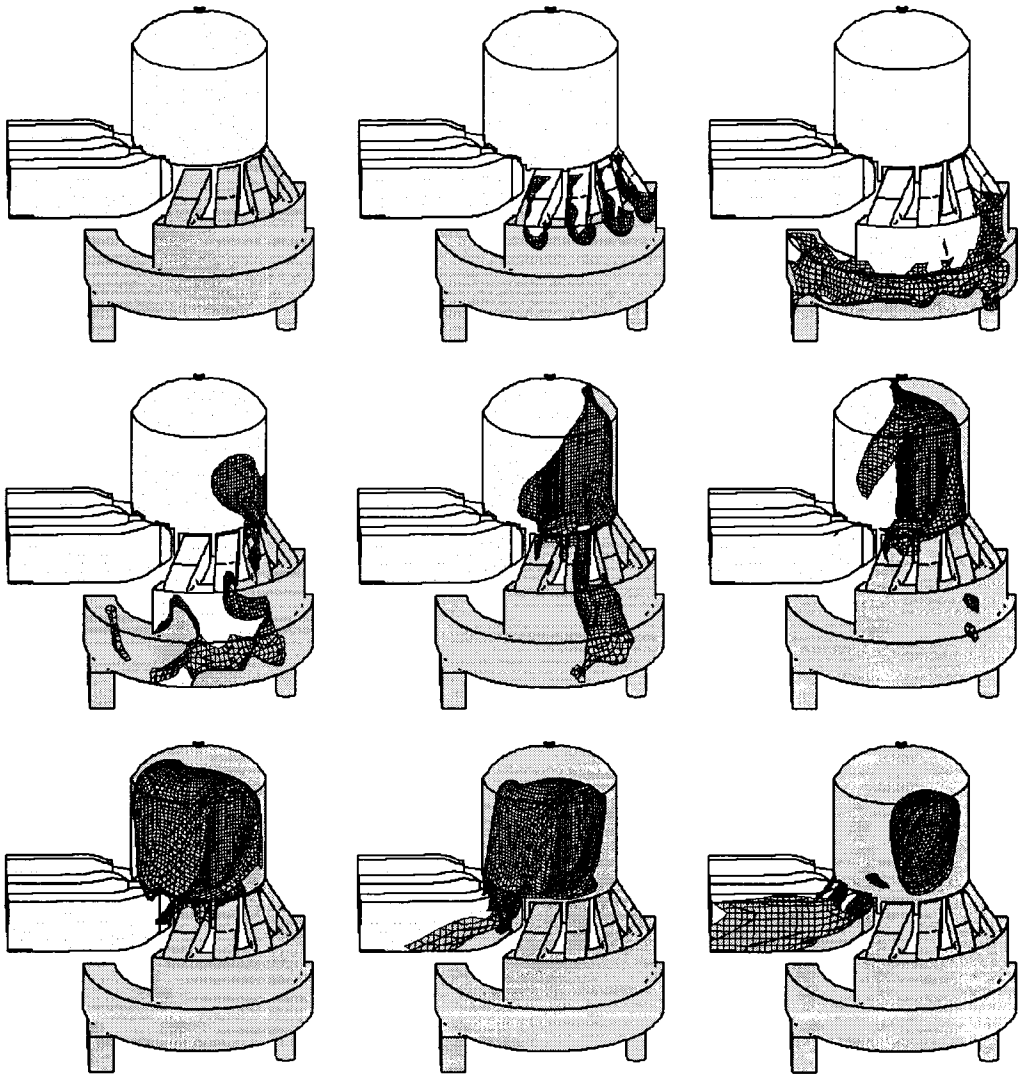

Fig. 5.5 Simulation results of scavenging process for conventional GMV engine. Dark colored region stands for intake fresh air. Numbers represent crank angle in degrees before TDC.

into the cylinder has been established. This positive intake flow is formed earlier in the intake ports farther from the exhaust ports. The schnurl ports direct the flow toward the area of the cylinder opposite the exhaust ports and toward the top of the cylinder, so that most residual gases are displaced toward the exhaust ports, rather than mixed. A cylinder-size vortex, for which the axis is perpendicular to the symmetric plane of the engine, is formed as a result of this scavenging flow. It is observed that some residual gases are trapped in this vortex and are mixed with the intake gas.

Some section plots at 135 degrees before TDC are presented in Fig. 5.6 to show the flow fields and the flow structures formed at the late stage of the scavenging process. Fig. 5.6(a) shows velocity vector plots at four different equally spaced horizontal planes. Velocity magnitude contours at the same section planes are presented at Fig. 5.6(b). Since both the intake and the exhaust ports are still open at this instant, the intake gas flow from the schnurl intake ports and the out-flow to the exhaust ports are clearly seen from the plots at the bottom plane. In-flow from the intake ports is directed toward the opposite side of the exhaust ports and toward the top, forming a narrow up-drift near the plane of symmetry. On the other hand, a downward drift has been formed along the exhaust side cylinder walls toward the ports holes. The distribution of these up and down drifts is easily seen in the velocity magnitude contours of Fig. 5.6(b). This sweeping flow makes a loop around the cylinder. More velocity vector section plots are shown for two different vertical planes; one for the plane perpendicular to the plane of symmetry (Fig. 5.6(c)) and the

other for a plane parallel to the plane of symmetry (Fig. 5.6(d)). Induced vortex motions are shown clearly in the Figures.

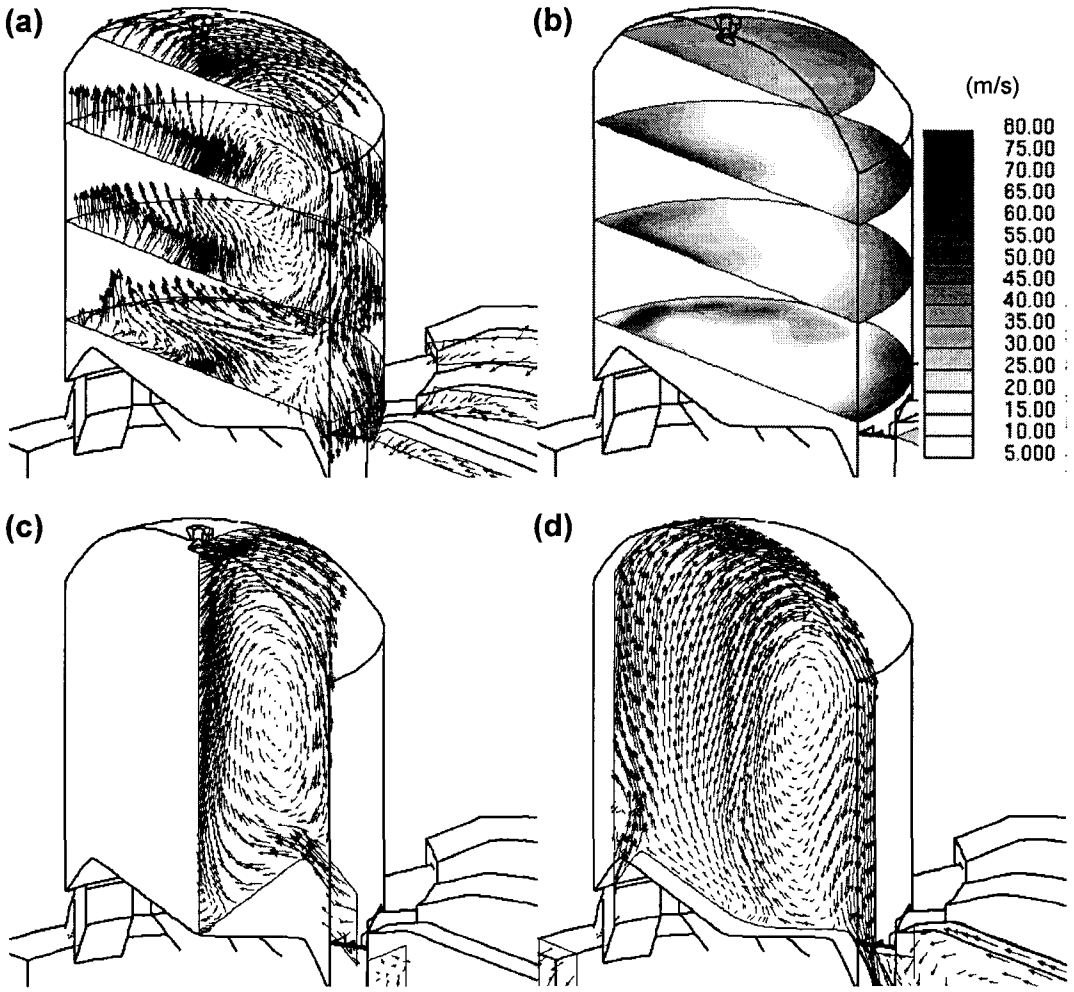

Fig. 5.6 Section vector plots (Fig. 5.6(a), (c), (d)) and velocity magnitude contour plots (Fig. 5.6(b)) at 135 degrees before TDC showing cylinder flow fields induced by scavenging

Iso-surface contours of static pressure at the same instant are presented in Fig. 5.7 in order to define more clearly the vortex structure induced by the scavenging flow. A cylinder scale vortex tube has formed inside the cylinder, and its general shape can be inferred from the figure. Most of the old charge gases are displaced by the sweeping intake gases, but some of burnt gas would be trapped in this vortex and remain as residual gas in the cylinder with a consequent lowering of the scavenging efficiency of the engine.

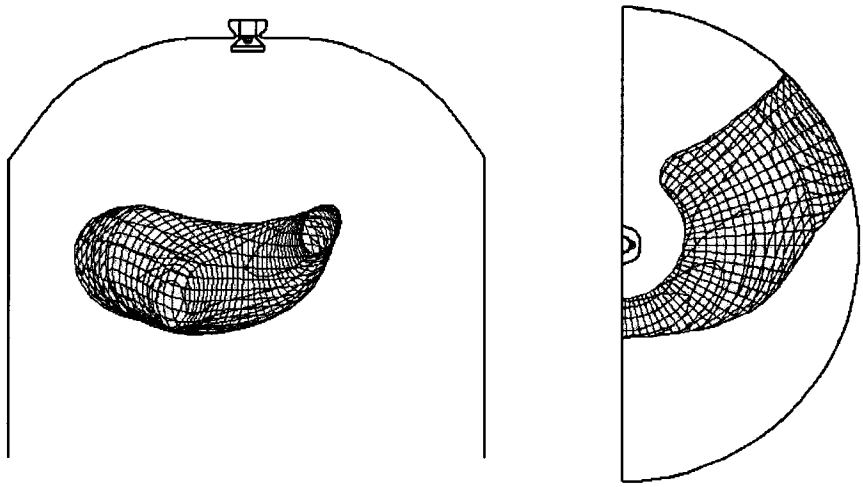

Fig. 5.7 Iso-surface contours of static pressure

The amounts of intake air and old charge gas inside the cylinder are plotted as a function of crank angle in Fig. 5.8. The mass of old charge gas in the cylinder starts to decrease rapidly as the exhaust ports open at 246 degrees before TDC. Even though the intake ports open at 239 degrees before TDC, hardly any intake air comes into the cylinder until about 220 degrees before TDC. During this period, the old charge gas rushes not only into the exhaust ports but also into the intake ports, because the cylinder pressure is still higher than the intake air manifold pressure.

Subsequently the old charge pushed into the intake manifold is pushed back again into the cylinder as the piston moves downward to the bottom dead center position. Therefore, the mass of the old charge gas in the cylinder increases between 220 and 210 degrees before TDC due to the positive net in-flow of the old charge. After this the old charge decreases monotonically until the ports close at 113 degrees before TDC. The amount of the fresh intake air in the cylinder has a maximum at about 140 degrees before TDC. After that, net out-flow becomes larger than the in-flow to make the air mass decrease as well as the mass of residual gas. After the ports close, the scavenging efficiency is predicted to be 0.85.

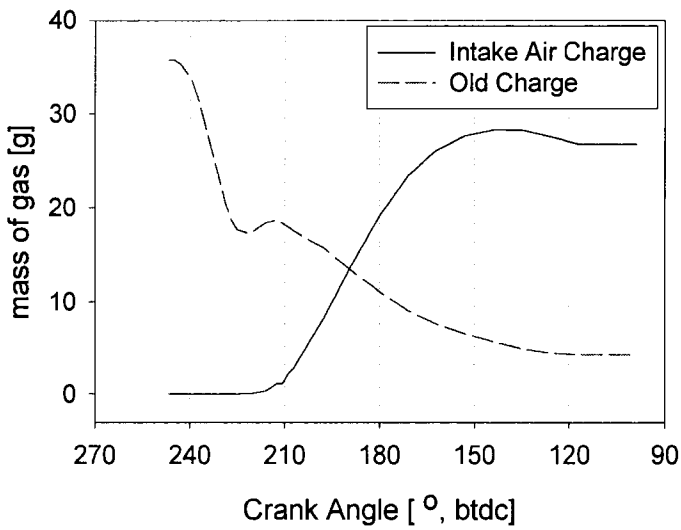

Fig. 5.8 Gas mass variations in cylinder as a function of crank angle

5.4.2 Fuel Injection and Mixing

The fuel injection and mixing during the compression stroke are shown in Fig. 5.9 from 117° before TDC to 18° before TDC. The shaded area in the Figures represents a mixture richer than the lean limit of flammability, ϕ = 0.5. As commented in the previous section, a cylinder scale vortex has already been

established in the chamber when the fuel starts to issue from the valve. In the in-cylinder flow fields induced by the vortex, the bulk flow direction near the valve is from the intake side to the exhaust side and the bulk flow near the piston top surface moves toward the intake side. It is observed that the flow pattern inside the cylinder during fuel injection is still dominated by the scavenging flow. The injection jet is initially tilted a little bit to the exhaust side, but it is bent back toward the intake ports side as the jet tip approaches the piston top. Finally the fuel jet impinges on the piston

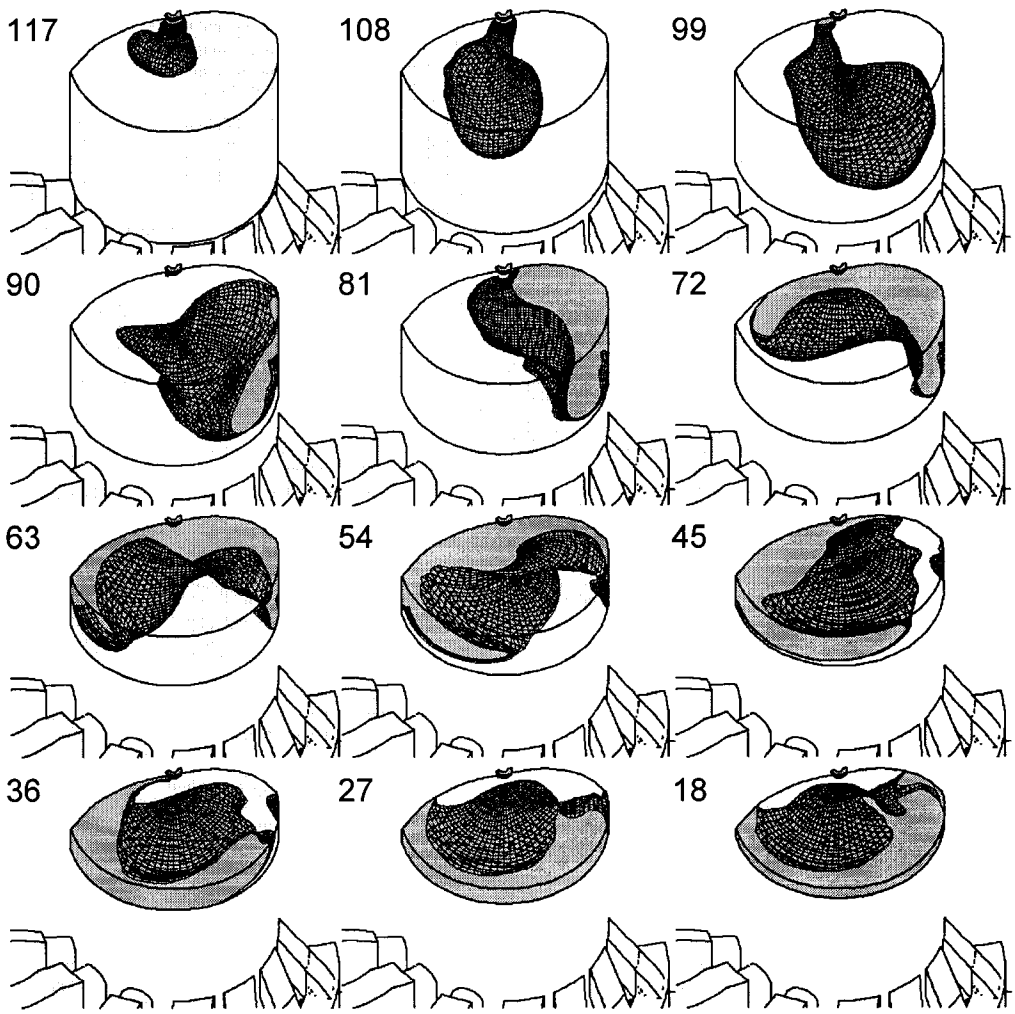

Fig. 5.9 Illustrations for fuel injection and mixing in conventional operation of GMV engine. Dark colored region stands for the mixture richer than the lean limit of flammability. Numbers represent the crank angle in degrees before TDC.

top off center to the intake side. Note that the fuel jet is not much mixed prior to impacting the piston. The jet does not fill the cylinder volume in a symmetric fashion, but sweeps toward the intake ports, around the top of the cylinder volume toward the opposite side of the cylinder, and along the outer edges of the piston top.

The flammable mixture fraction, Eq. (5.1), is defined as the ratio of the flammable mass to the total mass in the cylinder at any instant.

$$f_m = \frac{flammable\,mass}{total\,mass} \qquad (5.1)$$

The mixture fractions are computed by integrating over all of the computational cells in the cylinder and plotted as a function of crank angle in Fig. 5.10. Calculating the flammable mixture fractions during the compression process facilitates evaluation of the effectiveness of the fuel-air mixing for the injection system of the engine investigated. A lean mixture in a cell was defined as one with an equivalence ratio less than 0.5, a flammable mixture has an equivalence ratio between 0.5 and 2.0, and a rich mixture has an equivalence ratio greater than 2.0. Our definitions of lean, rich and flammable mixtures are based on laminar flame propagation limits at atmospheric pressure and nominal atmospheric temperature. At top dead center, both pressure and temperature are substantially higher. It is generally observed that the lean limit is not strongly affected by increasing pressure and temperature. Since our basic mixing problems exist on the lean limit our conclusions should still be valid in the main.

Kim et al. [5.1] reported that the jet impingement on the piston top enhanced the fuel-air mixing in this engine and they also showed that the mixing rate decreased after the impingement period without scavenging flow. However, Fig. 5.10 indicates

that there still exist mechanisms to keep the mixing rate high after the jet impingement when scavenging flow effects are considered. The cylinder flow fields driven by the scavenging flow reinforces the mixing to increase the flammable mixture fraction linearly as shown in Fig. 5.10.

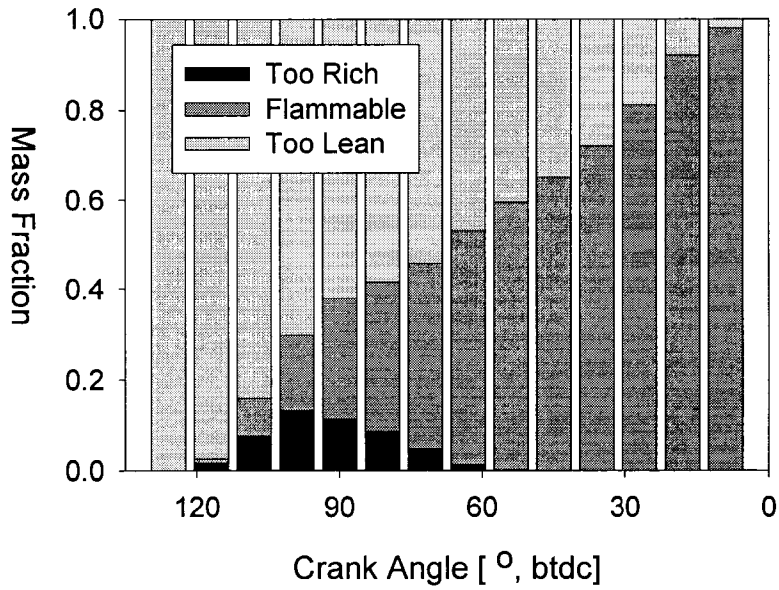

Fig. 5.10 Flammable mixture fraction as a function of crank angle in degrees before TDC

5.5 Power Stroke

The power stroke model includes combustion and pollutant generation, as well as the details of flame propagation and fluid flow structures in the cylinder.

5.5.1 Combustion Modeling

A single step global reaction model for methane combustion was used in this chapter to model the natural gas combustion.

$$CH_4 + 2O_2 \rightarrow CO_2 + 2H_2O \qquad (5.2)$$

The concentration of each species in the above reaction as combustion proceeds depends on both chemical reaction and the species transport. As discussed in the previous section, the fuel and the air mixture are not completely mixed at ignition. Since the mixture inside the cylinder is non-homogeneous, the CFD code solves a pair of differential conservation equations for the leading reactant, methane, and its mixture fraction. Algebraic equations based on stoichiometry are used for the remaining species.

Methane is known as a relatively slow burning hydrocarbon. Thus, both chemical kinetics and the turbulent micromixing were considered to determine the fuel consumption rate by using a combined time scale (Abraham et al. [5.6]) for the purpose of evaluating the reaction time scale. The relative influence of the chemical kinetics and the fluid mixing can be determined from their characteristic time scales, where the controlling factor is the one with the longer time scale (i.e. The slower process). During the early phases of combustion, when the fuel and oxidizer temperatures are low, the chemical kinetics time scale will be relatively long. As combustion proceeds, and the cylinder temperature increases, the chemical kinetics time scale will become shorter. The combined time scale model assumes that the volumetric fuel consumption rate, R_F (kg/m^3·s), is inversely proportional to the reaction time scale, t_R, as shown in Eq. (5.3) and that the overall reaction time scale is the sum of the turbulent mixing and the chemical kinetics time scales.

$$R_F = -\frac{\rho}{t_R} A_e \min\left[m_{methane}, \frac{M_{methane}}{2M_{oxygen}} m_{oxygen}, B_e \frac{M_{products}}{3M_{products}} m_{products} \right] \qquad (5.3)$$

where A_e, B_e are empirical coefficients determined from matching computed heat release rates with experiment, and typically A_e ~20, B_e ~2.5 (Kuo and Reitz [5.7]). The arguments in the square brackets of Eq. (5.3) determine the local rate limiting minimum concentration of either the fuel, oxygen or products. The reaction time scale t_R is given by Eq. (5.4).

$$t_R = t_T + t_C \tag{5.4}$$

The mixing time scale t_T is the time for the dissipation of a turbulent eddy. The mixing time scales are relatively small in locations of high shear, such at the edges of a jet, and at the cylinder walls. A typical mixing time scale in an engine cylinder is of the order of 1 to 10 ms. The turbulent mixing time is computed from the ratio of the turbulence kinetic energy k to its dissipation rate ε.

$$t_T = \frac{k}{\varepsilon} \tag{5.5}$$

The chemical time scale t_C is determined by the chemical kinetics reaction rate ω.

$$t_C \propto \frac{1}{\omega} \tag{5.6}$$

For the above global reaction shown in Eq. (5.2), a chemical kinetics reaction rate can be calculated through Eq. (5.7), assuming an Arrhenius type reaction.

$$\omega = -\frac{d[CH_4]}{dt} = Ae^{-E_a/RT}[CH_4]^n[O_2]^r \tag{5.7}$$

where $[CH_4]$ and $[O_2]$ are molecular concentrations of the fuel and oxygen respectively, A is the Arrhenius pre-exponential factor, E_a is the activation energy, R is the gas constant, and T is temperature. The Arrhenius pre-exponential factor A, and

the activation energy E_a are initially estimated from laboratory data (Westbrook and Dryer [5.8]) for homogeneous constant volume reactions. The combustion in the large bore engine is modeled as an imperfectly mixed, non-constant volume reaction, and A was adjusted to fit the experimental combustion pressure profiles. Values of A = 5.3 x 10^9 , E_a = 2.02 x 10^8 J/kmol, m = -0.3, n = 1.3 were used in the computations. Fig. 5.11 shows the comparison of the measured and the simulated cylinder pressure profiles.

In case $t_T >> t_C$, Eq (5.3) will be identical to the eddy break up model which has been used extensively in turbulence controlled engine combustion computations. Since $t_R \geq t_T$ by the definition, the reaction rate predicted by combined time scale model is generally less than that for the eddy break up model.

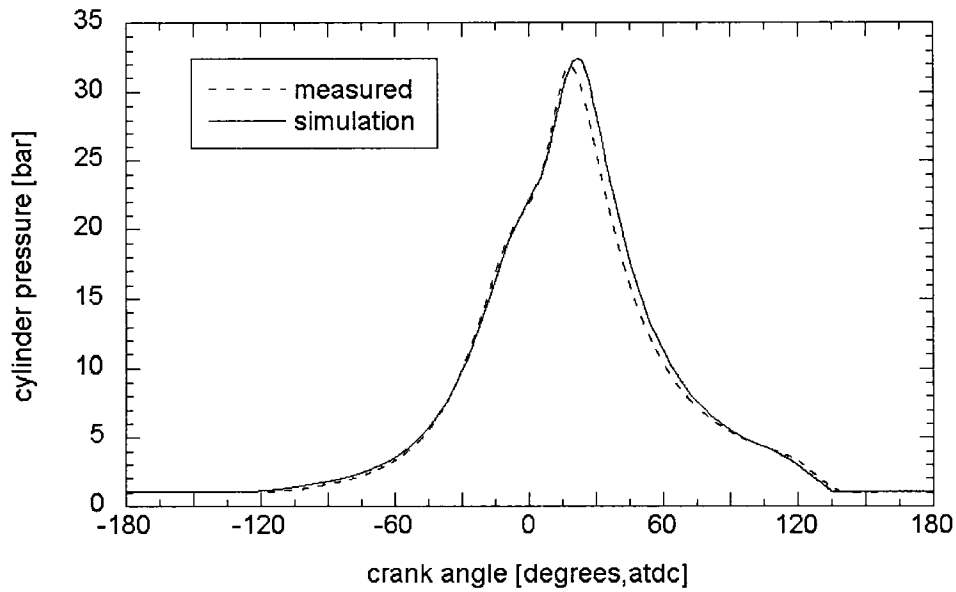

Fig. 5.11 Pressure Trace comparison between experimental measurement and simulation

5.5.2 NO_X Formation Modeling

Nitrogen oxides (NO_x) are formed throughout the cylinder during the combustion process due to the reaction of atomic oxygen and nitrogen. In spark ignition engines, the dominant component of NO_x is the nitric oxide (NO) formed in the high temperature gases left behind by the flame front. The chemical model for this reaction mechanism used in the calculation is the extended Zeldovich mechanism:

$$O + N_2 \leftrightarrow NO + N$$

$$N + O_2 \leftrightarrow NO + O \qquad (5.8)$$

$$N + OH \leftrightarrow NO + H$$

The first reaction is a nitrogen dissociation reaction triggered by an oxygen atom. This reaction is endothermic with an activation energy of + 75.0 kcal, since a nitrogen triple bond needs to be broken, while the other two are exothermic, so the first reaction is the controlling reaction. Since the production of atomic nitrogen (N) is much slower than its consumption, it is reasonable to assume that the amount of N in the reactor at any instant is small enough that the steady-state assumption for this highly reactive intermediate species can be applied. In addition to that, equilibrium assumptions were made for O_2, O, H_2, H, H_2O and OH to evaluate the local NO reaction rate at a given time as a function of the concentrations of O_2, N_2, NO and pressure and temperature.

Since the concentration of NO is low for most of calculation domain, its influence on the flow field can be ignored. In addition, the time scale for NO formation reaction is known to be longer than the time scales for turbulence mixing or combustion of hydrocarbons. Therefore, the NO computation can be decoupled from

the main reaction flow fields prediction. The conservation equation for NO was solved with the local production rate by the extended Zeldovich mechanism at each time step with the given velocity, species concentrations, temperature and pressure fields. To include the effect of turbulence-chemistry interaction in NO formation, a probability density function model was used for temperature fluctuation.

5.5.3 Initial Fields for Combustion

The initial fields for combustion should be investigated carefully to understand the following flame propagation and pollutants generation. Because of the non-homogeneity of the mixture system in the cylinder of this engine, spatial fuel distribution, mean flow fields and turbulence quantity fields at ignition timing could be critical factors determining the characteristics of heat release during the expansion stroke. A plot for the fuel distribution is shown in Fig. 5.12 just before the start of ignition at 10 degrees before TDC. Dark colored region represents flammable mixture

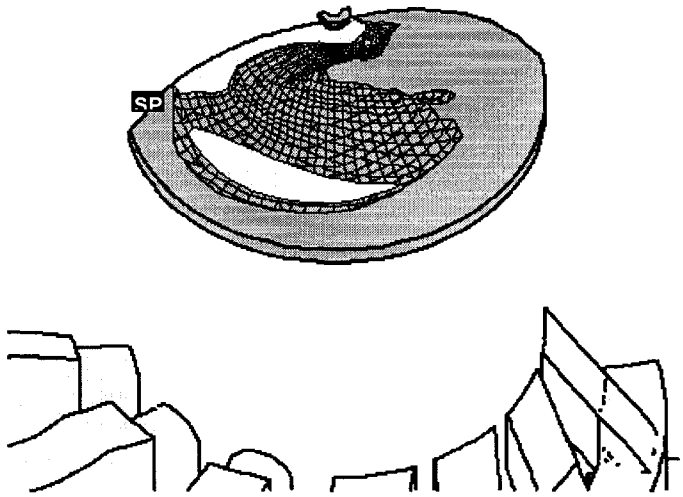

Fig. 5.12 Flammable mixture distribution in cylinder at ignition timing, 10 degrees before TDC

filling 98 percents of the cylinder volume. Flammable mixture is ranging with equivalence ratios from 0.5 to 1.5. The location of spark plug is marked as SP in the figure. As seen in the figure, a lean pocket still remains when the ignition occurs in this engine.

Selected section plots including more detailed information of the combustion initial fields are shown in Fig. 5.13 and in Fig. 5.14. Fig. 5.13(a) and Fig. 5.13(b) present the contours of equivalence ratio at the horizontal and vertical section planes which are equally spaced. Three consecutive contours shown on the right side of Fig. 5.13 are the top views of the horizontal section contours. There is a lean region in the core to the spark plug located side, and richer regions in the crevice around the edge of the cylinder. For the same section planes, velocity magnitude contours and vector plots are presented in Fig. 5.14. The scavenging induced cylinder size vortex dominates the cylinder flow pattern at ignition timing. An energetic bulk flow exists on the plane of symmetry forming a narrow drift from the intake ports side to the

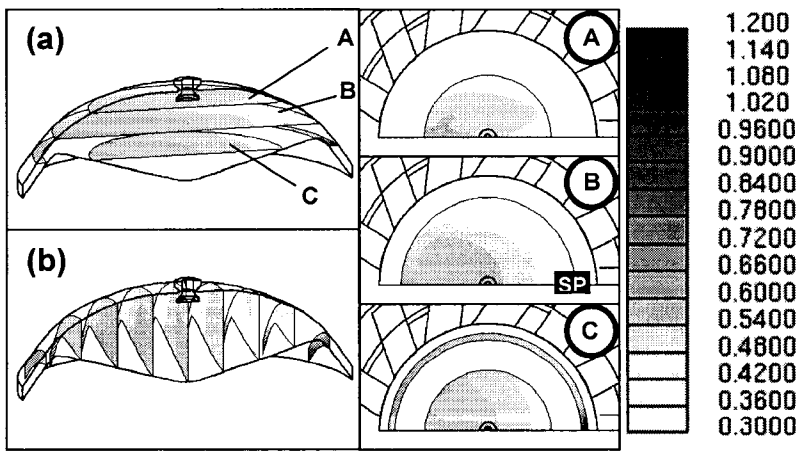

Fig. 5.13 Section contours of equivalence ratio for fuel distribution at ignition

exhaust ports side. This flow direction is opposite to the expected flame propagation which would start from the spark plug. On the other hand, the flow direction in the crevice is from the exhaust side to the intake side.

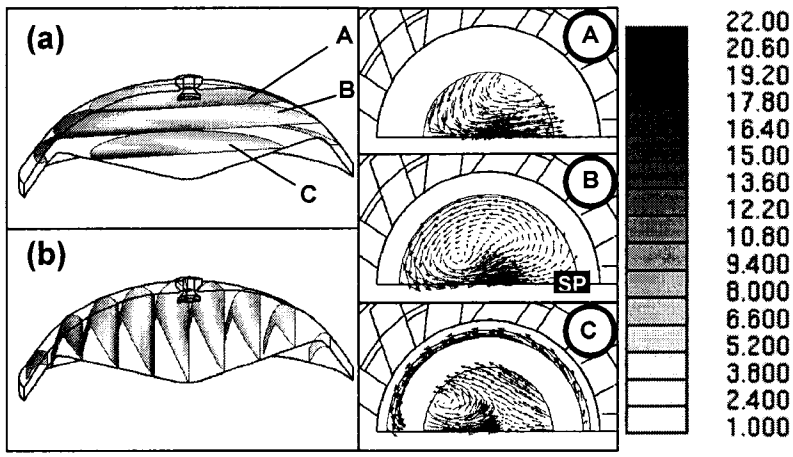

Fig. 5.14 Section contours and vector plots for cylinder flow fields at ignition

5.5.4 Flame Propagation

The combustion flame propagation is shown in Fig. 5.15 at 3.6 degree

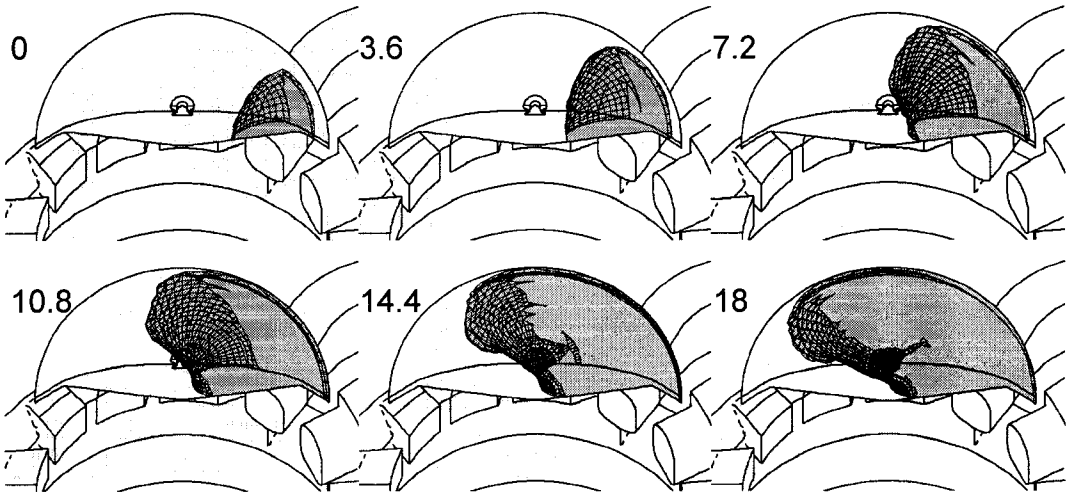

Fig. 5.15 Illustration of flame propagation in conventional operation of GMV engine. Numbers represent crank angle in degrees after TDC.

intervals after top dead center, from 0 to 18 degrees after TDC. The flame is centered at the spark plug, and then propagates through the cylinder volume. This flame travel was visualized by tracking with combustion products. Since the fuel is richer and the flow direction is favorable to the flame propagation in the crevice, the flame mainly propagates along the rim, not across the center. Therefore, the flame travels faster in the azimuthal direction in conventional operation of this engine. The duration of heat release is about 30 crank angle degrees.

5.5.5 NO_X Generation

The NO concentration iso-surface contours are presented in Fig. 5.16 from 18 to 63 degrees after TDC with 9 degrees interval to locate the NO generation spots in the cylinder. Locating the NO formation region is important when the NO reduction technologies such as water injection for combustion gas cooling are considered. The corresponding temperature field contours are also shown in Fig. 5.17. This comparison of the NO formation contours and the temperature contours implies the

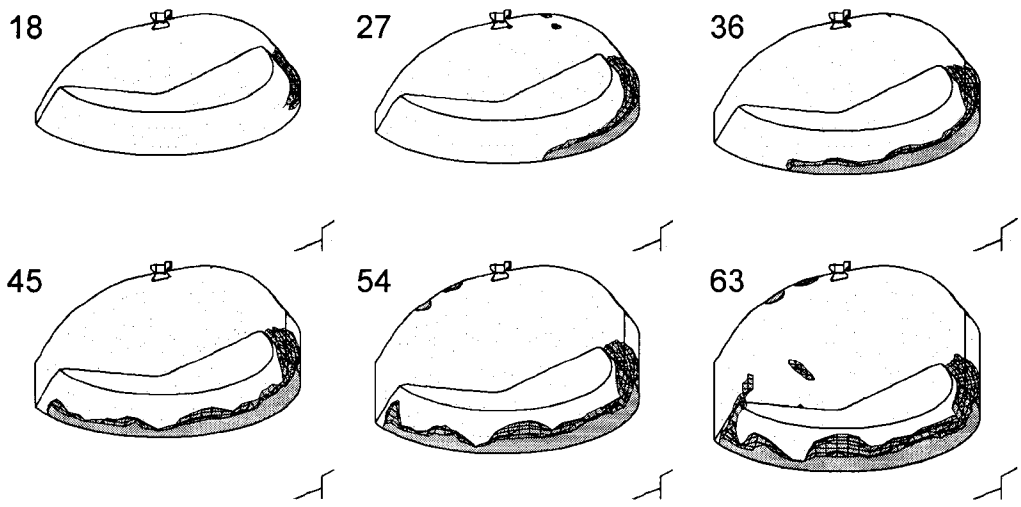

Fig. 5.16 Iso-surface contours of NO concentration for locating NOx formation. Numbers represents crank angle in degrees after TDC.

strong temperature dependence of the NO formation mechanism. The NO is formed in the high temperature post combustion zones. As shown in Fig. 5.16, the NO is mainly formed in the crevice region where the nearly stoichiometric mixture is burnt and compressed earlier so that the region can be heated up more. The end-gas burning is another source of NO. Because the end-gas is continuously compressed and heated before the flame reaches, the flame temperature of end gas is high enough for NO production as shown in the last two frames in Fig. 5.16 and Fig. 5.17.

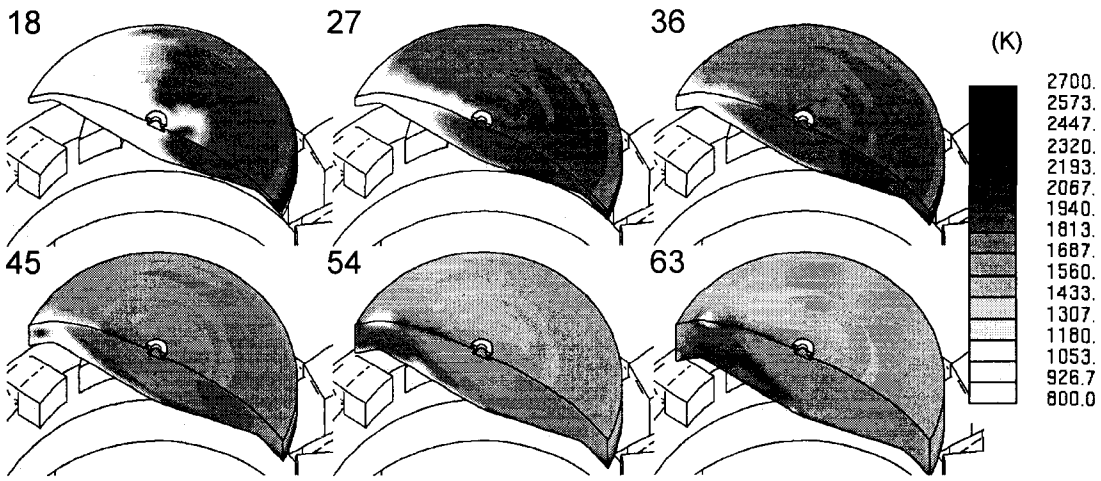

Fig. 5.17 Temperature Contours as a function of crank angle. Numbers represent crank angle in degrees after TDC.

5.6 Retrofit Technologies

Poor in-cylinder mixing due to ineffective fuel delivery system is believed to be problematic in this natural gas engine. Insufficient mixing causes unexpected flame extinguishment that leads to CO and CH_2O. In addition, cyclic combustion instability is one of key-contributor to NO_x and CO. Therefore, enhancement of fuel-air mixing using 35 bar high pressure pipeline gas for fuel injection and use of alternative stable ignition systems such as pre-combustion chamber ignition and laser

ignition are being considered as promising engine retrofit technologies. The retrofit technologies investigated are categorized into two areas: Fuel-Air Mixing Enhancement, and Alternative Ignition Systems.

5.6.1 Fuel-Air Mixing Enhancement

One of the promising mixing enhancement technologies is high pressure fuel injection. In conventional operation, natural gas is typically injected at low pressures, 1~3 bar above manifold pressure. Since natural gas pipelines operate at pressures of the order of 35 bar, it is of interest to explore the use of pipeline gas at high pressure as the source for injected fuel. However, the cost of three dimensional engine

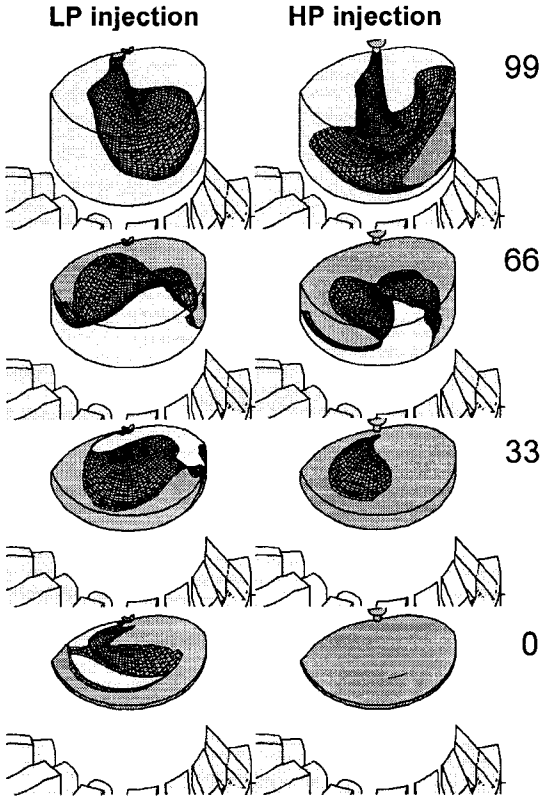

Fig. 5.18 Comparison of fuel injection and mixing between conventional low pressure fuel injection and high pressure pipeline fuel injection. Numbers represent crank angle in degrees before TDC.

simulations becomes considerable if the computational model has to capture the details of the complex supersonic flow structures in and near the intricate geometry of the injection valve. So, a supersonic virtual valve was designed for a three dimensional engine CFD model (Kim et al. [5.9]) to reproduce the actual downstream jet characteristics which were of crucial importance in the macroscopic engine performance. In Fig.5.18, the high pressure fuel injection and mixing during the compression stroke are compared with conventional low pressure injection. The gridded dark colored regions in the figures represents a mixture richer than the lean limit of flammability, $\phi = 0.5$. In the high pressure injection case the flow patterns are similar, but the fuel moves with higher momentum so that the most of the volume in the cylinder is flammable at top dead center.

5.6.2 Alternative Stable Ignition Systems

Lean burn combustion is a common solution for emissions reduction. However, if the combustion occurs in a very lean regime or mixing is not sufficient, CO and hydrocarbon emissions become unacceptably high due to ignition misfires. PCC (Pre-combustion chamber) ignition and laser spark ignition are potential retrofit technologies for obtaining stable ignition. Since a flame jet provides the ignition in the main chamber, PCC ignition is less affected by lean regions or poor mixing around the spark plug, resulting in greater stability of combustion. With a laser-based system, the spark can be positioned at any location in the cylinder.

Comparison of the flame propagation in conventional spark ignition, PCC ignition, and laser spark ignition is presented in Fig. 5.19. With spark ignition, the flame mainly propagates along the rim in the azimuthal direction, not across the

center. The flame propagation during PCC ignition is quite different. The flame propagates faster across the center than in the azimuthal direction. In this case, the flame jet overcomes the adverse flow field of the main chamber. For the laser ignition computation, the laser spark location chosen was slightly off-center to the intake side. The flame initially propagates toward the chamber center, then the flame front moves radially outward. The duration of heat release is about 25 degrees of crank angle for the PCC and laser spark ignition systems, and about 30 degrees for the conventional spark case.

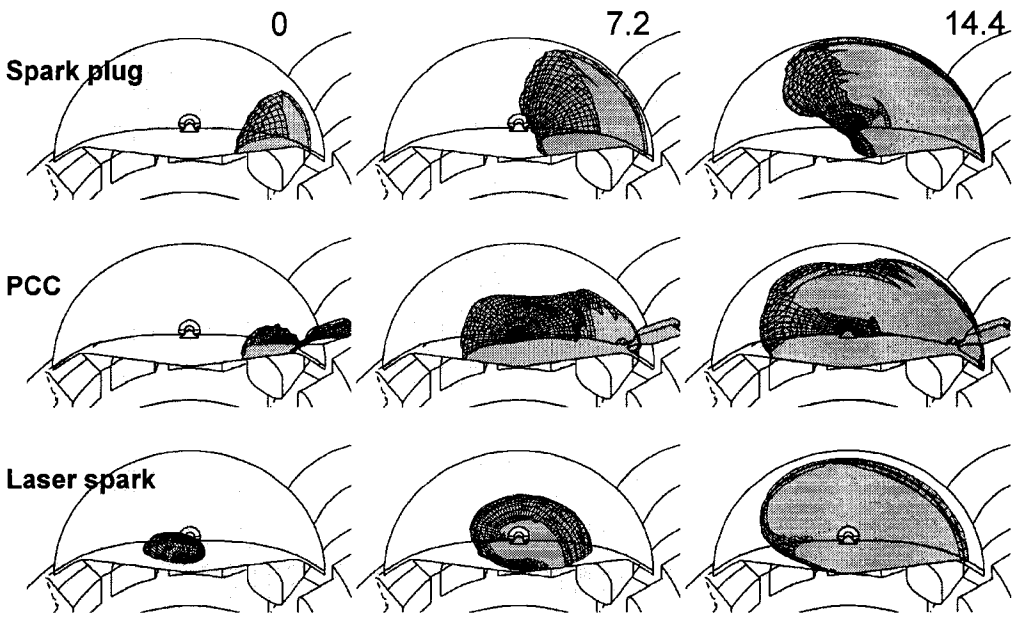

Fig. 5.19 Flame propagation comparison in different ignition systems. Numbers represent crank angle in degrees after TDC.

In Fig. 5.20, the NO formation of the conventional spark ignition case and laser spark ignition case are compared. Knowledge of the NO formation region is important for NO reduction technologies such as water injection. With the conventional spark ignition, NO is mainly formed in the crevice region where the

richer mixture burns at a higher temperature. On the other hand, since the combustion in the laser spark ignition case starts at chamber center, NO is mainly formed near the cylinder center.

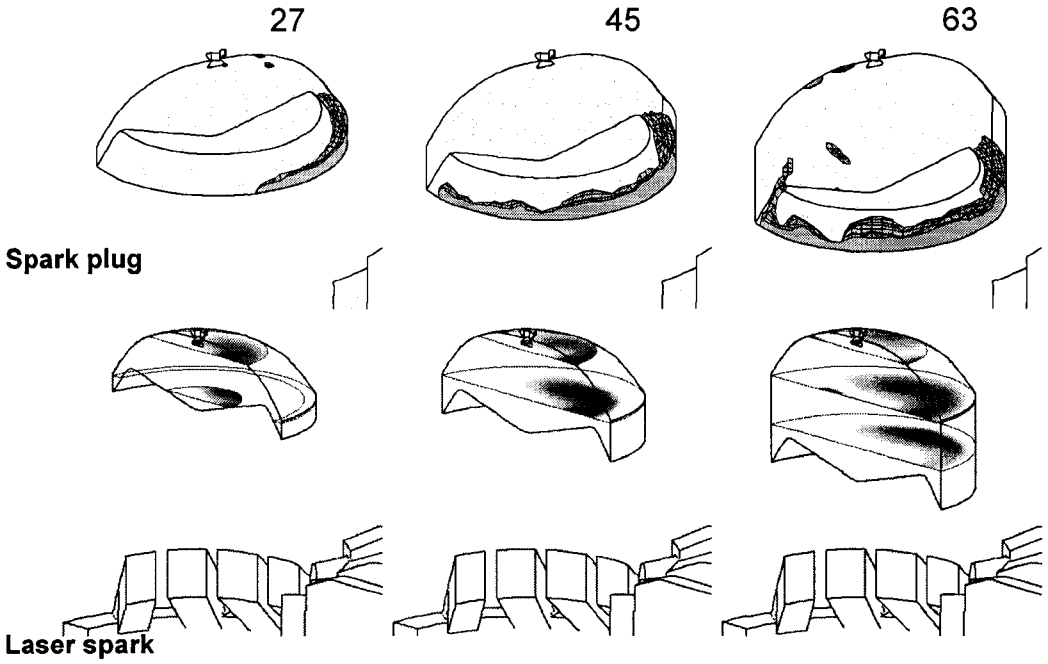

Fig. 5.20 Comparison of location of NOx formation in different ignition systems. Numbers represent crank angle in degrees after TDC.

CHAPTER 6: Conclusions

Fluid dynamics and combustion in the Cooper engine, a typical large bore natural gas engine, were investigated using Computational Fluid Dynamics models. Retrofitted designs and operating conditions of the engine were suggested for engine performance improvement.

In Chapter 2, the effects of injection pressure and valve geometry configuration on the fuel jet were investigated numerically by using two types of poppet valves operated at different pressures. The results indicated that with an unshrouded valve, the low pressure injection supersonic jet became over-expanded while flowing through the poppet valve, was rapidly compressed and slowed to subsonic speed after the valve exit, and eventually collapsed to the axis of symmetry of the valve downstream to form a "bell-shaped" subsonic jet. If the same valve was used with a high pressure supply, the supersonic flow was under-expanded in the valve and further expansion and spreading of the jet occurred after the valve exit. Eventually the jet impinged upon and ran along the cylinder wall in this case. At high pressures, addition of a shroud around the poppet valve was effective in directing the supersonic flow toward the center of the cylinder. With a shroud in place, the jet from a high pressure supply eventually formed a supersonic "bell-shaped" jet on the axis of symmetry some distance downstream of the valve exit. In tested valves of Type A (un-shrouded low pressure valve) and Type B (shrouded high pressure valve), the downstream axial momentum flow rate from the high pressure shrouded valve was about twice that of the valve without a shroud operated at a low pressure, while the

flow of kinetic energy was about six times as large. PLIF experiments for the low pressure valve without a shroud and for the shrouded valve at high pressure showed flow patterns that were quite similar to those of the computational predictions, at least qualitatively. Computations performed for a cylinder model with a moving piston indicated that the shrouded valve operated at high pressure provided better mixing of fuel and air than the unshrouded valve operated at low pressure. The flammable mixture fraction at TDC was predicted to be 5% to 7% higher at TDC for high pressure injection, regardless of the mass of fuel injected. Average turbulent kinetic energy in the cylinder at TDC was also predicted to be about twice as large for high pressure injection as for low pressure injection.

Numerical simulations of the gas flow through various poppet valve geometries were performed in Chapter 3. Both push and pull poppet valve geometries with nozzle were studied. The stagnation pressure losses, momentum delivery downstream and downstream flow characteristics of the jets from conventional poppet valves and the modified valves were compared. Pressure-based valve injection efficiency was defined and used to compare the valve injection performance. Valve and nozzle based stagnation pressure losses were quantified and classified for both low and high pressure conditions. A mixing fraction parameter was also defined to compare valve performance in a moving piston simulation.

The results indicate that a conventional poppet valve is a relatively inefficient mechanism to deliver momentum to a fuel-air mixture. Comparison of the results indicates that it is possible to make significant improvements in injection

performance with respect to momentum delivery by incorporating well-designed converging-diverging nozzles into the poppet valve geometry.

The development of a compatible virtual valve which reproduces downstream jet characteristics of the jet issuing from actual valves is described in Chapter 4. Complex supersonic structures in intricate actual valve geometry cause dramatic increase of calculation cost. Instead of including the complex detail of real valve, a simple converging-diverging type virtual valve is suggested for a three dimensional engine simulation with high pressure injection. Downstream flow characteristics such as velocity profile, momentum flow rate and mass flow rate are compared between the jets emanating from actual and virtual valves. Various mixing parameters are evaluated in moving piston simulations that include the effect of the jet-piston interaction. The results indicated that the suggested converging-diverging nozzle type virtual valve produces practically identical down stream fuel jet with the real valve injection jets.

In Chapter 5, a computational model incorporating a moving grid simulation of the scavenging, compression, combustion, and expansion processes of a Cooper GMV engine was developed and validated through comparison with experimental results. The numerical computations indicate that the schnurl ports direct the intake gas flow toward the opposite side to the exhaust ports and toward the top of the cylinder, so that a cylinder-size vortex is formed as a result of this scavenging flow. The interaction between the scavenging flow and the injected fuel jet causes the jet to deflect enough to impact the piston top off center, producing non- symmetric mixing in the cylinder. The injected fuel jet does not fill the cylinder volume in a symmetric

fashion, but sweeps toward the intake ports, around the top of the cylinder volume toward the opposite side of the cylinder, and along the outer edges of the piston top. The combustion mixture is not fully mixed at the time of ignition. The cylinder volume has a flammable mixture ranging with equivalence ratios from 0.5 to 1.5. There is a lean region in the core, and richer regions in the crevice around the edge of the cylinder. The combustion duration is about 30 degrees. The flame propagation during combustion is non-uniform, with a greater flame speed in azimuthal direction.

The simulation results of retrofit technologies for better mixing and more stable ignition are presented and compared with the results of conventional operation case. The computations indicate that high pressure fuel injection enhances the cylinder mixing. The fuel jet impinges on piston top and moves with higher momentum so that the most of the volume in the cylinder is flammable at top dead center. The alternative ignition methods change flame propagation pattern so that the duration of heat release is shortened. A pre-combustion chamber is used to obtain stable ignition by ensuring the mixture near the spark plug is flammable. The flame jet from the pre-combustion chamber overcomes the adverse cylinder flow, so that the flame propagates across the center of cylinder reducing the duration of heat release. Locating a laser spark near the center of the cylinder reduces flame travel distance inside cylinder to shorten the heat release duration. It is observed that the location of NO_X formation in the cylinder is different for the two alternative ignition systems.

REFERENCES

[2.1] Birch, A. D., Brown, D., Dodson, M., and Swaffield, 1984, "The Structure and Concentration Decay of High Pressure Jets of Natural Gas", Comb. Sci. and Tech., 36, pp. 249-261.

[2.2] Ewan, B.C.R., and Moodie, K., 1986, "Structure and Velocity Measurements in Underexpanded Jets", Combustion Science and Technology, Vol. 45, pp. 275-288

[2.3] Li, Y., Kirkpatrick, A., Mitchell, C., and Willson, B., 2001, "Analytical and Computational Modeling of High Pressure Gas Injection", Proc. ASME Fall 2001 ICE Conference.

[2.4] Ouellette, P., and Hill, P., 2000, "Turbulent Transient Gas Injections", J. Eng. For Gas Turbines and Power, 122, pp. 743-753.

[2.5] Mather, D. K. and Reitz, R., 2000, "Modeling the Effects of Auxiliary Gas Injection on Diesel Engine Combustion and Emissions", SAE Paper 2000-01-0657.

[2.6] Gaillard, P., 1984, "Multidimensional Numerical Study of the Mixing of an Unsteady Gaseous Fuel Jet with Air in Free and in Confined Situations", SAE Paper 840225,.

[2.7] Han, Z., Tsao, K., and Abdalla, M., 1994, "Computation of the In-Cylinder Processes of a Natural Gas Engine", SAE Paper 940213.

[2.8] Gundappa, M., Denlinger, M., Dulaney, K., Campbell, L., and McCarthy, J., 2000, "Computational Fluid Dynamics Modeling of Internal Combustion Engine Performance and Emissions", Proc Gas Machinery Conference, Austin, TX.

[2.9] Boyer, R., Craig, D., and Miller, C., 1954, "A Photographic Study of Events in a 14-In. Two-Cycle Gas Engine Cylinder", Transactions of the ASME, January, pp. 97-108.

[2.10] Conley, R., Hoffman, J., and Thompson, H., 1985, "An Analytical and Experimental Investigation of Annular Propulsive Nozzles", J. Aircraft, April, pp. 270-276.

[2.11] Sawada, K., and Asami, K. 1997, "Numerical Study on the Underexpanded Coanda Jet, J. Aircraft, 34, pp. 641-647.

[2.12]Abraham, J., and Magi, V., 1997, "Computations of Transient Jets: RNG k-e Model Versus Standard k-e Model, SAE Paper 970885.

[2.13] Papageorgakis, G., and Assanis, D., 1998, "Optimizing Gaseous Fuel-Air Mixing in Direct Injection Engines using an RNG Based k-e Model", SAE Paper 980135.

[2.14] Olsen, D. and Willson, B., 2001, "Planar Laser Induced Flourescence Imaging of Gas Injection from Fuel Valves for Large Bore Natural Gas Engines." Proc. ASME Fall 2001 ICE Conference.

[3.1] Kim, G.-H., Kirkpatrick, A., and Mitchell, C., 2004, "Computational modeling of natural gas injection in large bore engines", J. of Engineering For Gas Turbines and Power, 126, pp 256-264.

[3.2] Kim, G.-H., Kirkpatrick, A., and Mitchell, C., 2003, "Supersonic Injection Virtual Valve Design for Three Dimensional Numerical Simulations of a Large-Bore Natural Gas Engine", submitted to J. of Engineering For Gas Turbines and Power.

[4.1] Kim, G.-H., Kirkpatrick, A., and Mitchell, C., 2004, "Computational modeling of natural gas injection in large bore engines", J. of Engineering For Gas Turbines and Power, 126, pp 256-264.

[4.2] Gaillard, P., 1984, "Multidimensional Numerical Study of the Mixing of an Unsteady Gaseous Fuel Jet with Air in Free and in Confined Situations", SAE Paper 840225,.

[4.3] Han, Z., Tsao, K., and Abdalla, M., 1994, "Computation of the In-Cylinder Processes of a Natural Gas Engine", SAE Paper 940213.

[4.4] Gundappa, M., Denlinger, M., Dulaney, K., Campbell, L., and McCarthy, J., 2000, "Computational Fluid Dynamics Modeling of Internal Combustion Engine Performance and Emissions", Proc Gas Machinery Conference, Austin, TX.

[4.5] Ouellette, P., and Hill, P., 2000, "Turbulent Transient Gas Injections", J. Eng. For Gas Turbines and Power, 122, pp. 743-753.

[4.6] Mather, D. K. and Reitz, R., 2000, "Modeling the Effects of Auxiliary Gas Injection on Diesel Engine Combustion and Emissions", SAE Paper 2000-01-0657.

[4.7] Olsen, D. and Willson, B., 2001, "Planar Laser Induced Flourescence Imaging of Gas Injection from Fuel Valves for Large Bore Natural Gas Engines." Proc. ASME Fall 2001 ICE Conference

[4.8] Boyer, R., Craig, D., and Miller, C., 1954, "A Photographic Study of Events in a 14-In. Two-Cycle Gas Engine Cylinder", Transactions of the ASME, January, pp. 97-108.

[4.9] Abraham, J., and Magi, V., 1997, "Computations of Transient Jets: RNG k-e Model Versus Standard k-e Model, SAE Paper 970885.

[4.10] Papageorgakis, G., and Assanis, D., 1998, "Optimizing Gaseous Fuel-Air Mixing in Direct Injection Engines using an RNG Based k-e Model", SAE Paper 980135.

[5.1] Kim, G.-H., Kirkpatrick, A., and Mitchell, C., 2004, "Computational modeling of natural gas injection in large bore engines", J. of Engineering For Gas Turbines and Power, 126, pp 256-264.

[5.2] Boyer, R., Craig, D., and Miller, C., 1954, " A Photographic Study of Events in a 14-in. Two Cycle Gas Engine Cylinder"', Trans. ASME, January, pp. 97-108.

[5.3] Ouellette, T., Mtui, P., and Hill, P., 1998, "Numerical simulations of directly injected natural gas and pilit diesel fuel in a two stroke compression ignition engine", SAE paper 981400.

[5.4] Gundappa, M., Denlinger, M., Dulaney, K., Campbell, L., and McCarthy, J.,2000, "Computational fluid dynamics modeling of internal combustion engine performance and emissions", Proc. 2000 Gas Machinery Conference.

[5.5] Olsen, D. Hutcherson, G., Willson, B., and Mitchell, C., 2002, "Development of the Tracer Gas Method for Large Bore Natural Gas Engines – Part II: Measurement of Scavenging Parameters", Journal of Engineering for Gas Turbines and Power, 124, 3, pp. 686-694.

[5.6] Abraham, J., Bracco, F.V., and Reits, R.D. 1985 "Comparison of computed and measured premixed charge engine combustion", Combust. Flame, 60, pp.309-322.

[5.7] Kuo, T., and Reitz, R., 1989, "Computation of premixed charge combustion in pancake and pent roof engines", SAE paper 890670.

[5.8] Westbrook, C., and Dryer, F., 1981, "Simplified reaction mechanisms for oxidation of hydrocarbon fuel flames ", Combustion Science and Technology, 27, pp. 31-43.

[5.9] Kim, G.-H., Kirkpatrick, A., and Mitchell, C., 2003, "Supersonic Injection Virtual Valve Design for Three Dimensional Numerical Simulations of a Large-Bore Natural Gas Engine", submitted to J. of Engineering For Gas Turbines and Power.